Design of swirl recovery vanes in a slipstream of limited extension

MSc Thesis

J.A.C. van der Vlugt

Flight Performance and Propulsion

TU Delft Delft University of Technology

Challenge the future

DESIGN OF SWIRL RECOVERY VANES IN A SLIPSTREAM OF LIMITED EXTENSION

by

J.A.C. van der Vlugt

in partial fulfillment of the requirements for the degree of

Master of Science

in Aerospace Engineering

at the Delft University of Technology,

to be defended publicly on Thursday February 16, 2023 at 13:00.

Student number:	4449274	
Thesis committee:	Prof. dr. ing. G. Eitelberg	TU Delft, chair and supervisor
	Dr. ir. T. Sinnige	TU Delft, supervisor
	Dr. D. Modesti	TU Delft

An electronic version of this thesis is available at http://repository.tudelft.nl/.

Cover image source:
https://www.3dhubs.com/blog/cnc-machined-parts-for-aerospace/

TU Delft Delft University of Technology

ACKNOWLEDGEMENTS

This thesis report completes my Master of Science degree in Aerospace Engineering with a specialisation in Flight Performance at Delft University of Technology. Reaching this milestone has not been easy, but I am glad to have made the decision after my bachelor's in Mechanical Engineering to pursue a master's in Aerospace Engineering.

A master thesis is never completed alone and my report would not have reached this stage without the people around me. First, I would like to thank my supervisors Georg Eitelberg and Tomas Sinnige for their ideas, help and critical assessment. It was difficult to keep the meetings short, but I always left with new energy to continue the thesis.

Also, many thanks go to my roommates and friends who supported me during my master's. Above all, I would like to thank my parents, my brothers and my girlfriend who always believed in me to achieve my goals.

J.A.C. van der Vlugt
Delft, February 2023

SUMMARY

The ongoing search for more efficient propulsion systems in the fast-growing aviation sector has led to increased interest in propellers for their high propulsive efficiency. Due to the applied torque to the propeller, the propeller slipstream contains angular momentum or swirl. This angular momentum does not contribute to the thrust of the propeller and can thus be seen as an energy loss. This loss can be reduced by recovering some of the angular momentum. It has been demonstrated that the wing, downstream of the propeller, can recover a part of the swirl, however, more swirl could be recovered using stator vanes behind the propeller, so-called Swirl Recovery Vanes (SRVs). The SRVs can produce lift caused by the swirl angle of the propeller slipstream, the resultant force has a forward component which can be seen as additional thrust. These stationary vanes do not consume any power, but the additional thrust will increase the propulsor efficiency of the propulsion system. Previous research was focused on designing SRVs. A variety of high and low-fidelity models were used to predict the thrust of the SRVs. Both types of models predicted an increase in total thrust, however, the prediction of the SRV thrust between these models showed a discrepancy.

A low-fidelity model, based on the Lifting Line Theory (LLT), over-predicted the SRV thrust compared to wind tunnel experiments or CFD simulations. The flow field assumption in the LLT is an unbounded flow field which extends from $-\infty$ to $+\infty$. For propeller-SRV propulsion systems, this assumption is not valid because the propeller is located in close proximity upstream of the SRVs and defines the flow field at that location. Further, the height of the flow field is bounded by the other vanes, which can affect the lift. Therefore, the aim of this thesis is to use a correction to account for the boundaries imposed by the propeller and SRV.

It was found that the arc length between the SRV blades, of the configuration used in this thesis, was large enough to neglect the height boundary imposed by the other airfoil blades. For the SRV geometry, a blade number of 5 or higher would require a correction for the bounded height of the flow field. However, the axial distance, between the propeller outflow plane and the SRVs, was too small and therefore the aerodynamic simulation of the vane performance needs to be corrected. To validate the influence of the axial distance, a comparable case to the propeller-SRV configuration was used. Just like a propeller, an open-jet wind tunnel prescribes the flow field upstream of a 2D airfoil. If the axial distance between the exit nozzle of the open-jet wind tunnel and the leading edge of the 2D airfoil is small, the effect of the axial distance on the lift coefficient of the airfoil can be demonstrated. Previous research has established that the 2D-RANS (unbounded) and 3D-RANS (bounded) models predicted different lift values for the same airfoil. The 2D-RANS model assumes a potential flow flied, which means that the airfoil is in free-flight condition and the flow is not disturbed. The 3D-RANS model simulates the complete wind tunnel set-up and thus effect due to the close proximity of the airfoil to the wind tunnel exit nozzle is included. When the angle of attack of the 3D-RANS simulation is increased the solution would match with the 2D-RANS result. The amount of rotation can be approximated using the Biot-Savart law by taking into account the distance between the quarter chord point of the airfoil and the location of the prescribed flow field, the chord length, the far field angle of attack and the zero lift angle of attack. Assuming the thin airfoil approximation where the slope of the lift polar is equal to 2π, a new corrected lift polar can be computed.

Including the correction in the SRV design routine resulted in a prediction of thrust similar to the wind tunnel experiments and CFD simulations. Additionally, the original thrust prediction could also be matched with a corrected pitch angle of the SRVs. Along the blade, the maximum correction was located at the point of maximum circulation. Consequently, this location also had the biggest impact on the thrust prediction. Since most of the lift is produced at this location, the thrust will also increase the most if the angle of attack of this airfoil section is corrected. Since the correction was computed for each separate airfoil section along the blade, the correction angle was not constant which would make it complicated to implement when the SRVs are operated at off-design conditions. Operating the SRV at a high advance ratio requires a smaller correction angle compared to a low advance ratio. Rotating the whole vane by one constant correction angle across the blade and by having a variable pitch allows the correction method to be also useful at off-design conditions. Using an average and a weighted average of all correction angles of the airfoils, a similar thrust was obtained with the separate correction angles.

Finally, the airfoil design routine from Li was adjusted to account for the limitations of XFOIL. The airfoil performance solver could not converge for all angles of attack, especially around the stall angle of attack. Therefore, the stall angle was defined to be at the end of the linear regime of the lift polar. The newly designed airfoils were different compared to the airfoils designed by Li, however, no thrust was lost. Therefore more variations were investigated and it was found that the airfoil profiles and also the chord distribution have more design freedom without decreasing the thrust of the SRV due to the small effect of the profile drag.

To conclude, the over-prediction in thrust from the low-fidelity compared to the high-fidelity models can be captured using a correction method to account for the bounded flow field which submerges the SRV. The correction method can match the thrust of the high-fidelity model. When the angle of attack is increased, the original LLT thrust prediction can be obtained. This helps to have a more reliable thrust prediction using the much faster low-fidelity model.

CONTENTS

List of Figures

LIST OF TABLES

List of Symbols and Abbreviations

The list below describes several symbols and abbreviations that will be later used in this report.

Roman symbols

c	chord (m)
C_D	Drag coefficient (-)
C_d	Sectional drag coefficient (-)
C_L	Lift coefficient (-)
C_l	Sectional lift coefficient (-)
C_m	pitching moment coefficient (-)
c_{SRV}	SRV chord (m)
$C_{T,P}$	Thrust coefficient Propeller (-)
$C_{T,V}$	Thrust coefficient SRV (-)
CF	compressible scaling factor (-)
d	perpendicular distance from arbitrary point to vortex filament (m)
D_p	Diameter propeller (m)
d_{SRV}	Distance between propeller outflow plane and quarter chord point of SRV airfoil (m)
H	height of wind tunnel (-)
h	Maximum camber of airfoil (-)
h_p	Location of maximum camber of airfoil (m)
J	Advance Ratio (-)
k_1	Cascade interference coefficient
L'	Sectional lift (-)
n	Propeller rotational speed (rps)
P	Power propeller (w)
p	pressure (Pa)
Q_p	Propeller torque (Nm)
R	Radius propeller (m)
r	Radial location along propeller radius (m)
R_{hub}	Radius of hub (m)
R_{SRV}	Radius SRV (m)
s	Arc length (m)
T	Thrust (N)
t	Maximum thickness of airfoil (-)
T_P	Propeller thrust (N)

t_p	Location of maximum thickness of airfoil (m)
T_V	SRV thrust (N)
V^*	Inflow velocity (m/s)
V_∞	Freestream velocity (m/s)
v_a	Induced axial velocity (m/s)
V_a	Axial velocity (m/s)
v_t	Induced tangential velocity (m/s)
V_t	Tangential velocity (m/s)
w	distance from arbitrary point to line segment of vortex filament (m)
WF	weight factor (-)
Z	number of SRV blades (-)

Greek symbols

$\alpha_{C_l=0}$	Zero lift angle of attack (-)
α_{corr}	Correction angle of attack (-)
α_{des}	Design angle of attack (-)
α_{FA}	Free stream angle of attack (-)
α_{stall}	Stall angle of attack (-)
α_{WT}	Wind tunnel angle of attack (-)
β	Inflow angle (-)
β_i	Induced inflow angle (-)
Δ	Difference in vane thrust normalized with the propeller thrust (-)
Γ	Circulation (m^2/s)
γ	Stagger angle of Cascade airfoils (-)
ω	Propeller angular velocity (rad/s)
ϕ	Angle between blades of Propeller or SRV (-)
ρ_∞	Freestream density (kg/m^3)
θ	Pitch angle (-)

Abbreviations

$2D$	Two-Dimensional
$3D$	Three-Dimensional
BEM	Blade Element Momentum
CFD	Computational Fluid Dynamics
$CROR$	Contra Rotating Open Rotor
FF	Far field
LLT	Lifting Line Theory
SRV	Swirl Recovery Vane
WT	Wind Tunnel

1

INTRODUCTION

Aircraft propulsion systems are extremely refined and highly efficient devices. Currently, propulsion devices are operating close to their physical performance limit. To further improve the propulsive efficiency, the cowling can be removed from the turbofan engine resulting in a propfan or propeller, as can be seen in figure 1.1. Besides a higher propulsive efficiency, propellers also allow for more design flexibility such as electric propulsion or distributed propulsion compared to turbofans.

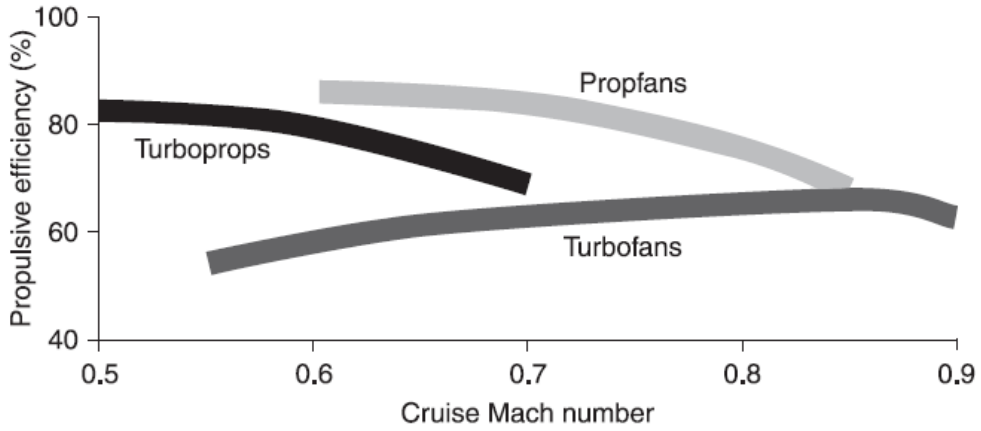

Figure 1.1: Propulsive efficiency of turbofans, turboprops and propfans at different cruise Mach number [1]

The already high efficiency of a propfan can be even further increased when the swirl of the propeller is recovered. It is known that the wing can recover a significant part of the propeller swirl [4]. Some important factors which influence the amount of recovery are the power setting, the wing loading and the propeller position relative to the wing.

The wing behind the propeller experiences different vertical velocities due to the swirl of the propeller. On the down-going side, the wing experiences a downwash and on the up-going side an upwash. In figure 1.2, a change of the effective angle of attack of the wing is shown and is adjusted from the work of Stokkermans [2]. The angle of attack of the wing is equal to the zero lift angle of the airfoil. In the finite case of a symmetric airfoil, this angle of attack would also be equal to zero, but for a cambered airfoil, this angle is non-zero. At the down-going blade side, the effective angle of attack becomes negative resulting in a negative resulting force R, hence a negative lift and forward-tilted drag force. At the up-going side of the blade, the resultant force is positive and tilted forward, consequently, the lift force is also positive and the drag is again in the same direction as the thrust. Both at the down-going blade side and the up-going blade side of the wing, the drag of the airfoil is decreased due to a change in the effective angle of attack. A reduction in wing drag effectively increases the thrust of the propeller-wing combination.

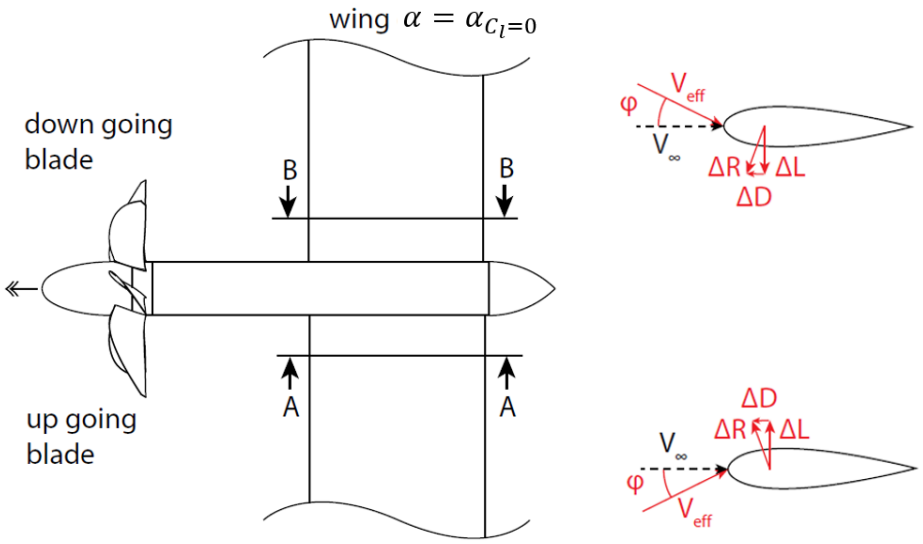

Figure 1.2: Recovery of swirl by a wing, at the zero lift angle of attack, submerged by the slipstream of a propeller at the up-going blade side (section A-A) and at the down-going blade side (section B-B)[2]

Even though some thrust is produced by partly recovering the swirl with the wing, the remaining swirl is still a loss. To further improve the swirl recovery, a second rotor can be placed behind the first rotor with a rotational direction opposite to the front rotor [11, 12], as is also shown in figure 1.3a. The first experiments by NASA were done using counter-rotating propellers (CROR) [13]. The results were promising since the propulsor efficiency increased up to 8% compared to a single rotor [13]. However, the efficiency increase came at the cost of increased complexity and weight due to the gearbox [14] and added noise [15].

(a) Contra rotating open rotor [13]

(b) Open fan demonstrator [16]

Figure 1.3: Swirl recovery concepts, contra rotating open rotor in (a) and a recent open fan demonstrator from CFM including an SRV in (b)

To simplify the CROR, the aft rotor can be replaced by stationary vanes to recover the propeller swirl, a so-called Swirl Recovery Vane (SRV). A recent concept by CFM presented in 2021 of an open fan-SRV configuration is depicted in figure 1.3b. Contrary to the recovery of swirl by the wing where a part of the surface was submerged by an upwash and a downwash due to the swirl, SRVs are fully submerged in an upwash which changes the direction of the inflow velocity. As is shown in figure 1.4, the inflow velocity for each vane becomes V^* instead of V_∞. The change in the angle of the inflow velocity results in a lift vector with a larger axial component, thus an increase in thrust force. Individually SRVs can produce more thrust compared to a wing optimized for the twist, as shown by Liu [17]. Respectively 1.4% thrust increase for the wing and a propeller-SRV can increase the thrust by 3.4% according to Li [3].

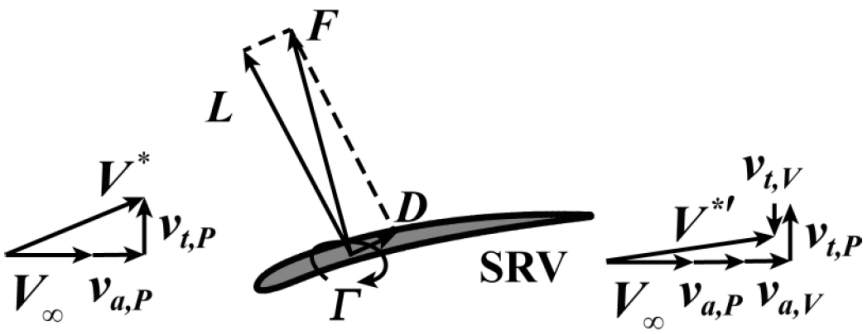

Figure 1.4: Velocity and force diagram of an SRV airfoil section. The inflow velocities (axial and tangential) are altered by the SRV, reducing the tangential velocity and increasing the axial velocity [3]

Interest in propellers due to their high efficiency has resulted in recent research on SRVs to further improve propulsor efficiency. Kuijk [18], Stokkermans [2] and Li [3] designed SRVs and studied their effects on the propeller and aircraft performance. High and low-fidelity models were used to predict the thrust increase due to the SRVs. Kuijk used a design method which was originally intended for rotor design, but by using a (very) low rotational speed, the SRV situation was approached. Unfortunately, the method did not reach the efficiency increase as predicted by several earlier studies. In the case of Stokkermans and Li the design routine for SRVs was based on the lifting line theory (LLT). In both SRV design methods, the thrust at a low advance ratio was over-predicted by 25% compared to validation using either CFD simulations or wind tunnel experiments. This large over-prediction by the SRVs design methods using an LLT model is undesired and it raises the question what assumptions are made in the LLT model, which are not present in the CFD simulations or the wind tunnel experiments.

The LLT assumes a flow field which extends from - ∞ to + ∞ in all directions. Since SRVs operate in the slipstream of the propeller, the flow field is bounded in the vertical and axial directions. Nederlof already showed, that the vertical boundary, i.e. height of the propeller slipstream, has a significant influence on the prediction of the wing lift by the lifting line theory at the location of the slipstream [19].

Only a part of the wing is submerged in the slipstream of the propeller, but for an SRV the full blade is inside the slipstream. Therefore, the height of the airfoil section of the SRV is not defined by the propeller diameter, but by the circumferential distance between the blades of the SRV. The second boundary to the flow field is the axial distance between the propeller and the SRV. The rotation of the propeller defines the flow field in the slipstream therefore, the flow can not be assumed to be at an infinite distance in front of the SRV. So far, the limitations of the upstream flow field boundaries were not taken into account in the SRV design, which provides a research opportunity.

1.1. RESEARCH OBJECTIVE

Having identified a gap of knowledge in predicting the thrust of SRVs by low-fidelity potential flow models the following research objective is formulated:

Reduce the thrust over-prediction of an LLT SRV design model by using a potential flow correction that better approximates the boundaries imposed by the propeller slipstream.

This objective results in the following research question and sub-questions.: ***What is the effect of a potential flow correction accounting for the upstream boundary of the flow field on the thrust prediction of a swirl recovery vane?***

- What are the boundaries of the slipstream?
- How and where will the boundaries be defined in the potential flow model?
- What is the impact of the adjustment to the potential flow model on the design result?

The questions will be answered by identifying the boundaries of the flow field assumed in lifting line theory. By applying a correction to the SRV design model, the boundaries should be captured appropriately. This

adjusted design model will then be used to compute the thrust of the SRV and the results will be compared with available data.

1.2. RESEARCH OUTLINE

This thesis report contains six chapters. After the introduction, the basics of propeller and SRV modelling will be explained in Chapter 2. Further, several SRV design models will be discussed, including the limitations of the models and where it needs to be improved. Chapter 3 will present the required correction for the LLT model including the validation of the model. It is followed by explaining how the corrected model is implemented in the design of the SRV in Chapter 4. Additionally, an adjustment is proposed for the airfoil profile optimization. Chapter 5 presents the results of the corrected design methodology and the thesis will be concluded in Chapter 6 with conclusions and recommendations for future work.

2

SRV DESIGN

In the introduction, some performance benefits of SRVs were briefly presented, in this chapter, the performance will be discussed more elaborately (section 2.1). Further, a description of the slipstream is provided (section 2.2) and basic propeller models are discussed (section 2.3). Followed by the definition of the SRV geometry and required terminology (section 2.4). Finally, different SRV design models (section 2.5) and their limitations will be discussed (section 2.6).

2.1. SWIRL RECOVERY

The rotation of the fluid, or swirl, is caused by a part of the propeller's shaft power that results in the angular momentum of the slipstream and does not contribute to the thrust of the propeller. As mentioned in the introduction, by recovering a part of the swirl the efficiency of a propeller can be increased. Swirl recovery can be done by positioning aerodynamic elements behind the propeller in the slipstream under a specific angle. These elements can be rotating resulting in contra-rotating open rotor (CROR) configuration or they can be static so-called Swirl Recovery Vanes (SRVs).

Previous studies showed an increase in propulsor efficiency for CRORs. A research project from NASA found that the propulsor efficiency could increase up to 8% compared to a single propeller if all swirl in the slipstream would be recovered at Mach 0.75 [13]. CRORs are beneficial because the loading can be split over two rotors, enabling a reduction in the rotor diameter compared to a single propeller, making the CROR more suited for high-speed flight. Mikkelson stated that CRORs would be able to increase the propulsor efficiency by 5 to 10% for high-speed flight [11] and for lower-speed flight even higher efficiency gains were expected. Additionally, also installation improvements were found for CROR, in reducing the torque and gyroscopic loads. However, the increased efficiency is paid for by a weight [20] and a noise penalty [21].

Starting with the noise penalty, having a static set of vanes does not provide additional noise to the propulsor in cruise conditions according to Dittmar and Hall [22]. However, other investigations contradicted this statement. Sinnige et al. [23] stated that the broadband noise was not affected, but a significant increase in tonal noise was perceived due to the SRVs at low thrust settings. Later, also van den Ende [24] showed that an increase in noise was found, however, this was only up- and down-stream of the propeller, meaning that the maximum noise in the cabin and on the ground remained unaltered.

Besides the noise, stator vanes are also simpler in terms of weight and complexity but are still able to recover swirl and produce thrust to increase the propulsor efficiency. Several studies captured the efficiency benefit of the SRV. Gazzaniga and Rose performed wind tunnel tests of a propeller-SRV configuration which increased the propulsor efficiency by 2% at the design Mach number of 0.8 [25]. Using a 3D Euler code, Yamamoto [26] showed that the numerical approach would predict a thrust increase by the SRV of 5% at the same conditions as in Gazzaniga [25]. The over-prediction is attributed to the lack of capturing the viscous phenomena of the flow in the Euler code.

In more recent research a CFD simulation of an isolated propeller with an SRV was performed by Wang [27]. The CFD experiments predicted an increase of almost 6% in the total thrust of the propeller-SRV configuration, but the propulsor efficiency was lower due to an increase in shaft power. Over the whole range of advance ratios, an increase in power was seen, however, the additional thrust of the vane reduced for increasing advance ratios and the vane thrust becomes negative from an advance ratio of J = 1.1. Therefore at higher advance ratios, the propulsor efficiency of the propeller-SRV combination is much lower compared to the isolated propeller.

Using CFD simulations in optimizing SRVs is not efficient, since the computational time is high. To reduce computational time, low-fidelity models are used in the SRV design procedure. Van Kuijk used XROTOR minimum induced loss routine [18]. Later, in section 2.5.1, a deeper explanation will be given of this design routine, but it predicted a propulsor efficiency gain of 2.5%. Stokkermans [2] developed a design procedure based on the non-linear lifting line theory and by maximizing the thrust of the SRV an optimal planform was designed. The model, based on the LLT, predicted a propulsor efficiency of 3.5% but the CFD simulations presented an increase of 2.6%. A similar trend was found in the design procedure of Li [3]. The numerical (LLT) design approach predicted an increase of 3.4% in total thrust, but in the wind tunnel experiments, only a 2.6% increase in thrust was measured. This difference will be discussed more elaborately further in this chapter.

2.2. FLOW FIELD OF THE SLIPSTREAM

The basis of swirl recovery is the conversion of the angular moment from the propeller slipstream into axial momentum using aerodynamic components behind the propeller. This highlights the importance of the slipstream on the effectiveness of the SRV. If the slipstream does not contain any angular momentum, the SRVs will not be able to produce any thrust.

The slipstream is the result of the added momentum from the propeller to the flow. This momentum can be decomposed into axial and tangential momentum and influences the characteristics of the surfaces submerged in the slipstream. Veldhuis showed that a wing lift distribution is heavily influenced by the propeller slipstream [4]. The slipstream is, in reality, an unsteady flow, however, to capture the unsteadiness the problem would become too complex and in general a steady flow, or time-averaged flow, forms a good approximation of the performance prediction of the lifting surfaces and thus will also be used in this study. The velocity components of the slipstream can be decomposed in the axial, tangential and radial velocity and will be discussed in the next sections.

2.2.1. AXIAL VELOCITY

The axial velocity is in the streamwise direction of the flow of the propeller. This is the main component responsible for the thrust produced by the propeller. A typical axial velocity distribution can be seen in figure 2.1. The non-uniformity of the distribution, in the radial direction, is caused by the loading of the propeller blade which is also not uniform. At the tip, there is a large drop in axial velocity due to the pressure equalization and the presence of a vortex. In the streamwise direction, the axial velocity is accelerated due to a pressure jump at the location of the propeller plane. Based on the law of Conservation of Mass, the increased axial velocity will cause a contraction of the slipstream to preserve the mass flow, as is shown in figure 2.3.

2.2.2. SWIRL VELOCITY

The second velocity component is caused by the rotational motion of the propeller and is the tangential or swirl velocity. Variations in propeller loading will change the tangential velocity distribution, while the axial velocity distribution stays constant [4]. Based on the vortex theory, the propeller blades are represented by a bound vortex. This bound vortex induces only a tangential velocity in the slipstream, not an axial velocity. As can be seen in figure 2.2, the induced tangential velocity is negative in front of the propeller. This is physically not possible, because upstream of the propeller there is no tangential velocity. This can be compensated using an assumption that the wake vorticity induces an opposite tangential velocity in front of the propeller plane. Downstream of the propeller, the tangential velocity is constant and has twice the magnitude of the swirl induced by the bound vortex at the propeller plane.

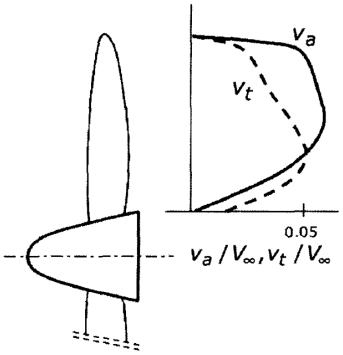

Figure 2.1: Typical axial and tangential velocity profile in the slipstream of a propeller [4]

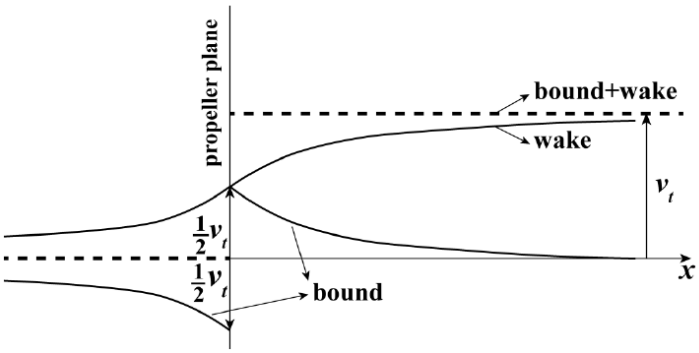

Figure 2.2: The tangential induced velocity (dashed line) in the propeller slipstream due to contributions of the bound and wake vorticity (solid lines) [3]

2.2.3. RADIAL VELOCITY

In the far field behind the propeller, the static pressure in the slipstream must be equal to the free stream pressure. Since there is a pressure jump across the propeller plane, the static pressure needs to decrease after the propeller which is possible if the axial velocity increases. This results in a variation along the streamwise location of the axial velocity distribution. The consequence of increased axial velocity is a contraction in the slipstream to conserve the mass flow in the slipstream. The slipstream contraction results in a velocity component in the radial direction. The contraction is large in front of the propeller disk and often small behind the propeller as can be seen in figure 2.3. Since the SRV is located behind the propeller, the radial velocity component will not be considered in this thesis.

2.3. PROPELLER MODELS

Understanding the velocities that play a role in the propeller slipstream, discussed in the previous sections, helps to start modelling the slipstream using different approaches. When only the axial velocity is taken into account, the slipstream can be modelled as a 1D Actuator disk model described in section 2.3.1. Modelling the slipstream in 2D by using the axial and swirl velocity is done using the Blade Element Momentum theory, in section 2.3.2. Finally, to model the 3D effects of the propeller blade the lifting line theory is used in section 2.3.3.

2.3.1. ACTUATOR DISK THEORY

A simplistic propeller model is the actuator disk (or momentum) theory. This theory, developed by Rankine [28], represents the propeller as a disk of an infinite number of thin blades at the same diameter. Another assumption is that the flow does not have a rotational component, it is incompressible and also viscosity is neglected. The disk has a uniform inflow field with free stream conditions defined by V_1 and p_∞, see figure 2.4. The momentum can only be varied in the axial direction in this 1D model. At the location of the disk, the static pressure of the flow increases instantly from p_1 to p_2, while the velocity is accelerated from V_1 to V_2, see figure 2.4. This increase in static pressure generates the thrust of the propeller disk. Using Bernoulli's law,

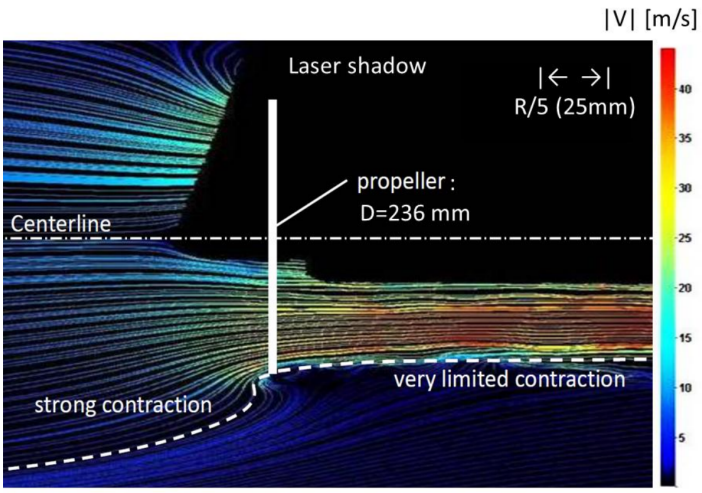

Figure 2.3: Contraction of the propeller slipstream indicated by streamlines and velocity magnitude[5]

the thrust can be written according to equation (2.1), with R as the radius of the disk. Downstream of the propeller disk, the static pressure decays again to the free stream pressure p_∞. The accelerated flow eventually converges at a new velocity V3, see figure 2.4.

The limitation of this 1D model is that only the axial velocity is accounted for, any other velocities in the slipstream are not included. While, the swirl velocity causes a loss in efficiency, excluding this velocity, will result in an over-prediction of the propeller performance. The next model presented includes the swirl velocity and would thus be better suitable for the performance calculations.

$$T = \pi R^2 \delta p = \pi R^2 (p_2 - p_1) \tag{2.1}$$

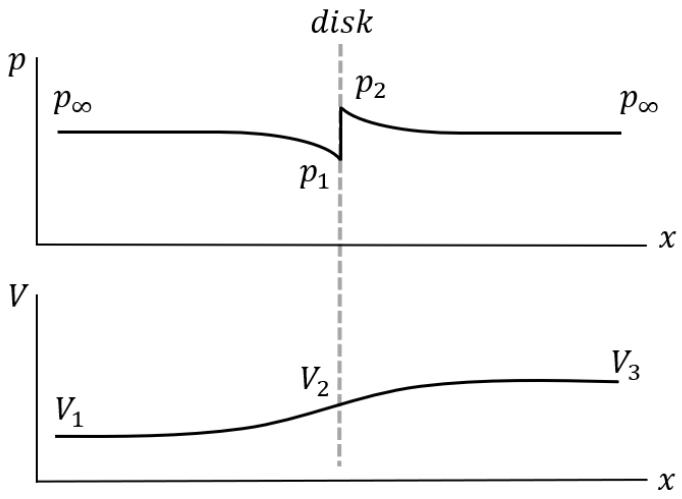

Figure 2.4: Pressure and velocity distribution for the actuator disk theory. p_∞ is the free stream pressure, p_1 and p_2 indicates the pressure jump at the disk, V_1 is the free stream velocity, V_2 is the velocity at the disk and V_3 is the accelerated flow converged at a new velocity.

2.3.2. BLADE ELEMENT MOMENTUM THEORY

A more sophisticated theory compared to the Actuator disk theory is the BEM (or Blade Element Momentum) theory. This theory is based on the coupling of the blade element theory and the momentum theory. The blade element theory divides the propeller blade along the radius into a number of elements and the aerodynamic performance of the 2D sections is separately analysed. The thrust must be equal to the difference in upstream and downstream momentum of a stream tube passing at the corresponding blade element.

Figure 2.5 shows the diagram of the velocities and forces of a blade element. The axial and tangential velocities are defined as V_a and ωr. Adding the induced velocities results in the effective velocity (V^*) of the blade. The magnitude can be computed by equation (2.2). The pitch angle of the blade element is defined by the summation of the inflow angle and the angle of attack $\theta = \beta_i + \alpha$. For a propeller blade section, the most important forces are thrust and torque. Both can be computed using the lift equation (2.3) and drag force equation (2.4), resulting in equation (2.5) for the thrust and equation (2.6) for the torque. These forces are also computed using the axial and circumferential momentum for each blade section. This results in a set of equations that can be solved by iteration. To obtain the forces of the full propeller, the blade elements need to be summed over the radius and multiplied by the number of blades as can be seen in equation (2.7) and equation (2.8). With Z as the number of blades and R_{hub} as the radius of the hub.

The BEM theory includes the axial and swirl velocity which would provide a good first-order approximation of the propeller performance. To improve the results even more a 3D model could be used to capture the development of the slipstream.

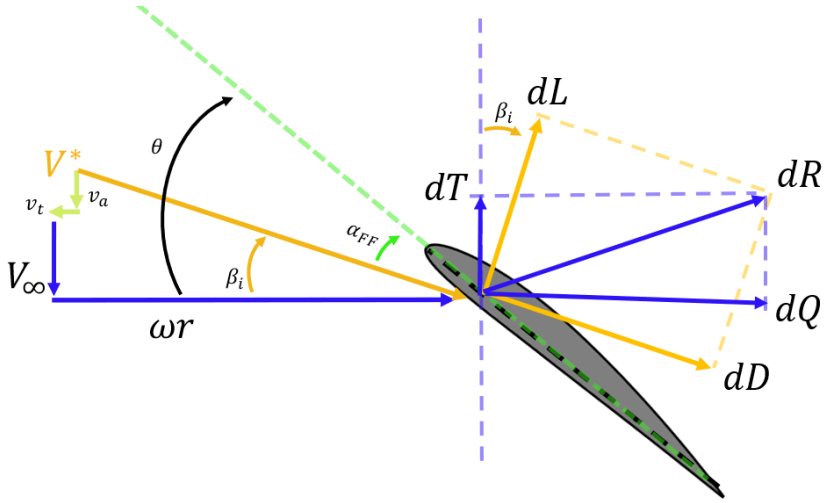

Figure 2.5: 2D blade airfoil section with velocity and force vectors used in the BEM theory. ωr indicates the rotational velocity, V_∞, V^*, v_a, v_t are respectively the free stream, inflow, induced axial and induced tangential velocities. β_i is the inflow angle, α_{FF} is the free stream angle of attack and θ is the pitch angle of the blade. The sectional forces are indicated by dR as the resultant force, dL and dD are the lift and drag forces, dT is the thrust force and dQ is the force producing the torque. The circulation of the blade is indicated by Γ

$$V^* = \sqrt{(V_\infty + v_a)^2 + (\omega r - v_t)^2} \tag{2.2}$$

$$dL = \frac{1}{2}\rho V^{*^2} C_l c dr \tag{2.3}$$

$$dD = \frac{1}{2}\rho V^{*^2} C_d c dr \tag{2.4}$$

$$dT_p = dL cos(\beta_i) - dD sin(\beta_i) \tag{2.5}$$

$$dQ_p = (dLsin(\beta_i) + dDcos(\beta_i))r \tag{2.6}$$

$$T_p = Z\int_{R_{hub}}^{R} \left[dLcos(\beta_i) - dDsin(\beta_i)\right] dr \tag{2.7}$$

$$Q_p = Z\int_{R_{hub}}^{R} \left[(dLsin(\beta_i) + dDcos(\beta_i))r\right] dr \tag{2.8}$$

2.3.3. LIFTING LINE THEORY

The lifting line theory was originally developed for fixed wings by Prandtl [29]. Betz [30] adjusted the theory to make it applicable for propellers. The blade of the propeller can be modelled using a bound vortex line at the quarter chord line of the blade. Helmholtz's theorem [31] states that a vortex can not end in a fluid. Combining this theorem with a variation of vorticity over the radius of the blade results in a shed vortex sheet behind the propeller. Due to the rotation of the propeller, the vortex sheet has a helical shape as it continues downstream, which is shown in figure 2.6. The magnitude of the vorticity can be described by the circulation. The circulation is defined as the line integral of the velocity vector along a closed contour. Typically, the maximum circulation can be found at 70% to 75% of the blade radius.

Representing the wake, two models can be used, a prescribed or free wake model. The prescribed wake model is much simpler and runs more quickly. The shape of the trailing vortices is usually a helix with constant pitch and radius based on the rotor geometry and operational parameters. The free wake model discretizes the wake of the slipstream into vortex panels which are aligned with the local velocities of the flow field otherwise there will be a pressure difference across the vortex sheet, hence a resultant force. The main benefit of a free wake is that the effect of the induced velocities on the trailing vortex filament is captured. The induced velocities account for the axial flow in the wake, the slipstream contraction and the vortex roll-up of the trailing vortices, which then influences again the induced velocities, thus making it an iterative procedure, until the full wake is prescribed [32].

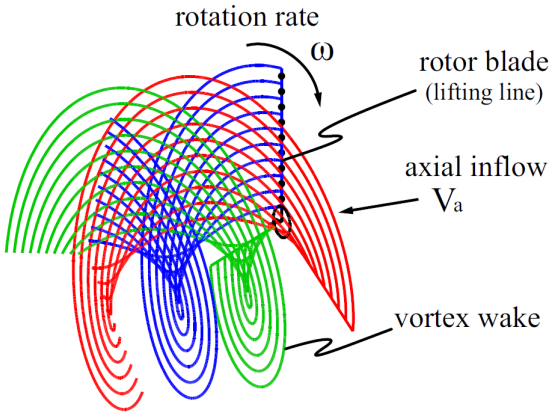

Figure 2.6: Helical vortex wake described by the Lifting line theory of a three-bladed propeller [6],

2.4. SRV GEOMETRY AND TERMINOLOGY

In this section, the most important design parameters of the SRV will be discussed and the non-dimensional coefficients are given. Figure 2.7 shows the layout of a propeller with SRVs. V_∞ is the free stream velocity in front of the propeller. The radius of the propeller blade and the SRV are respectively, R_p and R_{SRV}. The hub radius of the propeller is R_{hub}. For this study in particular the distance between the propeller trailing edge and the SRV's quarter chord is of importance, because the quarter chord is the location of the vortex that represents the airfoil, and is defined as d_{SRV}.

The performance of the propeller and the SRV are determined by the total thrust and total power. To be able to compare different sizes and operating conditions, the parameters are normalized with the density (ρ),

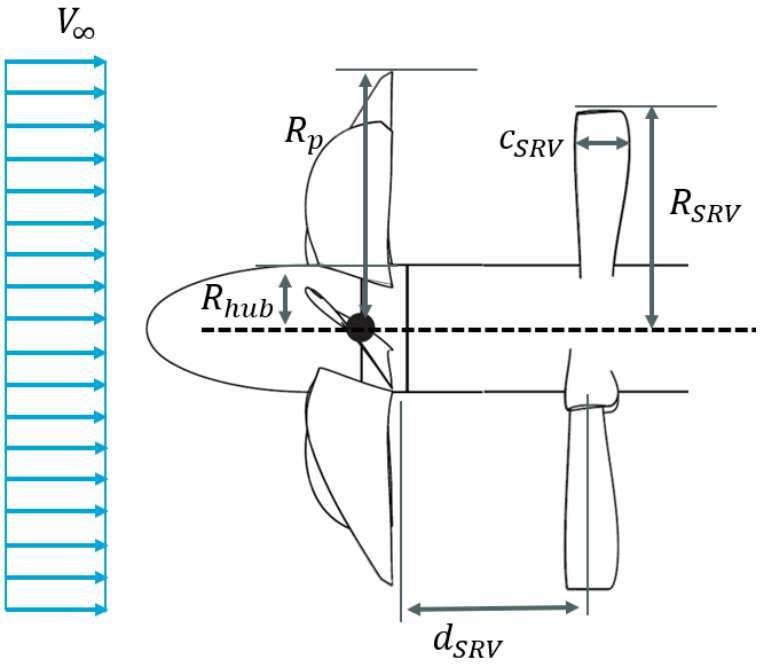

Figure 2.7: Layout of a propeller-SRV configuration. V_∞ is the free stream velocity, R_p, R_{SRV} and R_{hub} indicate respectively the propeller, SRV and hub radius. the chord of the SRV is c_{SRV} and d_{SRV} is the distance between the propeller outflow plane and the quarter chord point of the SRVs.

rotational speed (n) and diameter of the propeller (D_p), see equation (2.9) and equation (2.10) for respectively the thrust and power coefficient. Further, the advance ratio is used to normalize the propeller's velocity with the free stream velocity, see equation (2.11).

$$C_{T,P} = \frac{T_P}{\rho_\infty n^2 D_p^2} \tag{2.9}$$

$$C_p = \frac{P}{\rho_\infty n^3 D_p^5} \tag{2.10}$$

$$J = \frac{V_\infty}{nD_p} \tag{2.11}$$

The thrust coefficient of the SRV is computed by equation (2.12).

$$C_{T,V} = \frac{T_V}{\rho_\infty n^2 D_p^2} \tag{2.12}$$

The velocities and forces working on an airfoil section of the SRV are similar as presented for the BEM theory, see figure 2.8. The inflow angle is determined by the velocity profiles of the propeller, which are V_a and V_t for respectively the axial and tangential velocity. To obtain the effective inflow angle the induced velocities v_a and v_t need to be taken into account, which results in the effective inflow angle β_i defined by equation (2.13). The magnitude of the corresponding effective velocity is defined as equation (2.14). The pitch angle of the airfoil section is the summation of the effective inflow angle and the angle of attack, see equation (2.15).

$$\beta_i = atan\left(\frac{V_a + v_a}{V_t - v_t}\right) \tag{2.13}$$

$$V^* = \sqrt{(V_a + v_a)^2 + (V_t - v_t} \tag{2.14}$$

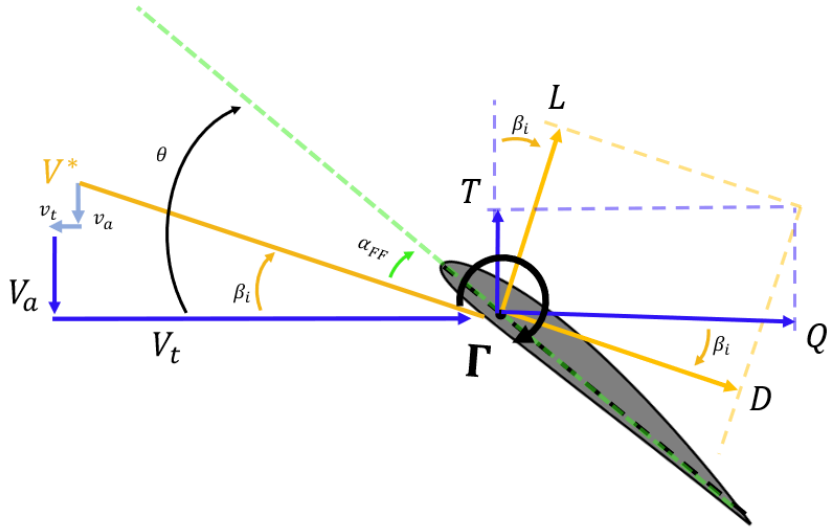

Figure 2.8: Velocity and force diagram of an airfoil blade section of an SRV. V_a, V_t, V^*, v_a, v_t are respectively the axial, tangential, inflow, induced axial and induced tangential velocities. β_i is the effective inflow angle, α_{FF} is the free stream angle of attack and θ is the pitch angle of the blade. The sectional forces are indicated by L and D as the lift and drag forces, T is the thrust force and Q is the force producing the torque. The circulation of the airfoil is indicated by Γ.

$$\theta = \beta_i + \alpha \tag{2.15}$$

In section 2.3.2 the equations to compute the lift, drag, thrust and torque were defined in equation (2.3) to equation (2.6). These equations also hold for the SRV airfoil. Figure 2.8 makes clear that the axial component of the lift and drag is responsible for the thrust generated by the SRV. Therefore, an airfoil profile is required to generate the required lift at minimal drag.

To determine the lift of each vane section the Kutta-Joukowski theorem is applied, see equation (2.16). Using this theory, two assumptions are made. The first one is already mentioned in section 2.2.3 and explains that the flow around the profile is 2D, so no radial velocities are considered. Secondly, each airfoil section has a uniformly distributed inflow of V^*.

$$L' = \rho V^* \Gamma \tag{2.16}$$

The equation for the thrust of an airfoil section, equation (2.5), can be rewriting into equation (2.17) using the drag, equation (2.4), and lift, equation (2.16).

$$dT_V = \left(\rho V^* \Gamma dr\right) cos(\beta_i) - \left(\frac{1}{2}\rho {V^*}^2 C_d c dr\right) sin(\beta_i) \tag{2.17}$$

To obtain the thrust of the full SRV blade all the sections of the blade needs to be integrated and the equation becomes:

$$T_V = \rho Z \int_{R_{hub}}^{R} \left[\left(V^* \Gamma\right) cos(\beta_i) - \left(\frac{1}{2} {V^*}^2 C_d c sin(\beta_i)\right)\right] dr \tag{2.18}$$

Finally, when basic trigonometry is used, the axial and tangential velocities and induced velocities can be included in the equation, see equation (2.19).

$$T_V = \rho Z \int_{R_{hub}}^{R} \left[\left((V_t + v_t)\Gamma\right) - \left(\frac{1}{2} V^* C_d c (V_a + v_a)\right)\right] dr \tag{2.19}$$

2.5. SRV DESIGN MODELS

Research on Swirl Recovery Vanes is not new, recent studies have contributed to SRV design models. This section will provide an overview of different models and their limitations. Starting with the model presented by van Kuijk, in section 2.5.1, where he uses a BEM method in combination with a minimum induced loss routing. The second design model, in section 2.5.2, is presented by Stokkermans and is based on a non-linear lifting line theory. The final design model is from Li and uses a combination of the BEM method and the lifting line theory, see section 2.5.3.

2.5.1. SRV MODEL BY VAN KUIJK

Van Kuijk [18], presented in his thesis a method to design SRVs and assessed their performance using a BEM method. In the method, a routine is used which is called the minimum induced loss (MIL) routine. This routine includes the finite span effects on the circulation distribution and includes the viscous drag in the performance analysis since in basic BEM methods this is not taken into account. The code used is called XROTOR from Drela and Youngren [33] and is an open-source code which typically needs a small number of iterations until it converges.

The MIL condition for a propeller blade can be compared to an elliptically loaded wing and has a constant efficiency (ratio of induced drag over lift) along the radial sections of the blade. The design point is defined by the overall lift coefficient of the blade and is iterated until the matching circulation is found. The output of the model is a chord distribution of the blade.

The limitation of the model is that the use of XROTOR's minimum induced loss design routine is perfectly applicable to design rotors, but it struggles with stator designs. The cause is due to the simple fact that XROTOR cannot handle non-rotating devices, such as stators. Recalling the 2D blade section in figure 2.5 the tangential velocity of the airfoil section is defined by the angular rotation of the blade. When this is set to zero for a stator blade, the overall efficiency becomes zero as well. This complies with the understanding of a stator blade since it does not impose a tangential slipstream on the flow. However, the iterations in XROTOR cannot start with an efficiency equal to zero. Van Kuijk already stated that this approach, using XROTOR, was not accurate enough and in the best case, it produces a sub-optimal design for the stator blades. Therefore, the next section will discuss an improved SRV design model.

2.5.2. SRV MODEL BY STOKKERMANS

The second SRV design approach which will be discussed here was presented by Stokkermans in his thesis [2]. His approach is used for an isolated propeller with a nacelle and aims to design the SRVs for maximum thrust compared to maximum swirl recovery since the propeller efficiency increases more when the SRV produces maximum thrust.

The design tool is based on the concept of a lifting line code, which is adjusted to allow for non-uniform inflow conditions. The lifting line method is used to find the induced velocities of the SRV and is based on Phillips and Snyder [34] and a three-dimensional vortex lifting law. The added third dimension, compared to the 2D Kutta-Joukowski theorem, is used to account for the sweep of the blade. The input for the lifting line code is a velocity field obtained from the CFD model of the propeller. To account for the sweep, at each section the bound vorticity is included when computing the induced velocity at the section. The method can also assess the off-design conditions because a large angle of attack behaviour is taken into account. Further, a modification is applied to include the effect of the nacelle. Approaching the nacelle, the axial velocity decreases due to the development of the boundary layer at the wall of the nacelle. The nacelle effect is accounted for using the image of the real part with equal vortex strengths, resulting in an imaginary part in the equation. To construct this image, an equation is used to calculate the radial position of the horseshoe vortex image inside a cylinder [35]. To account for the influence of the SRVs on each other, each vane requires a lifting line.

To define the airfoil properties of the SRV, a program called XFOIL by Drela is used [36]. In the tool, a NACA 4 series airfoil is defined using the airfoil thickness, maximum camber and position of maximum camber. XFOIL will then determine the lift and profile drag polars of the airfoil. When the airfoil performance is known, the SRV planform geometry is defined and the loading on the SRV blade is computed.

To obtain the maximum thrust for the SRV, an optimisation routine is built which consists of 14 variables: chord at root, taper ratio, Chord shape function, Class function variable determining tip chord slope, root

pitch angle, twist angle, Pitch shape function, airfoil thickness over chord ratio, airfoil maximum camber over chord ratio, airfoil chordwise location of maximum camber. The chord and pitch shape function consists of both out of 3 variables. During the optimisation, these 14 variables will be changed and using a gradient-based function in Matlab, the maximum thrust is found for a given swirl angle, free stream velocity and SRV geometry.

In figure 2.9 the output of the SRV thrust from the SRV analysis tool is compared with CFD experiments. The SRV blades were designed for a high thrust condition (J = 0.95). The figure shows a clear over-prediction of the thrust by the SRV analysis tool in comparison to the CFD simulation. The over-prediction is 25% for low advance ratios, but increasing the advance ratio will reduce the over-prediction to almost zero. Meaning that at high thrust conditions, the analysis tool has more difficulty in making a correct prediction of the thrust produced by the SRV.

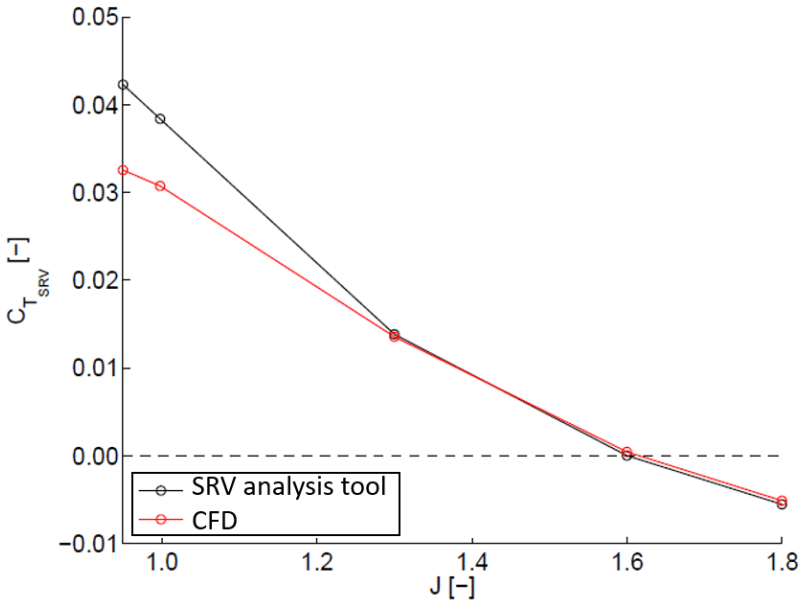

Figure 2.9: Thrust coefficient vs advance ratio for an SRV blade designed for high thrust. In black the SRV analysis tool is indicated, which is the LLT-predicted thrust and red the CFD thrust prediction is displayed [2].

Stokkermans attributes the over-prediction in thrust to a combination of effects. First, the airfoil properties are computed using XFOIL [36]. For these computations, the undisturbed air speed and mean chord are used. However, in reality, both the airspeed and chord vary along the span. Especially at lower advance ratios, the airspeed varies considerably. The second effect is the chord effect described by Jones [37], This effect is based on the influence of a limited aspect ratio for the blades. At low aspect ratios (3 according to Prandtl [29] and 4 according to Phillips and Snyder [34]) the loading can not be represented by a lifting line and therefore also the chordwise distribution of the lift should be taken into account. Using the correction of Jones [37], a reduction of wing lift of about 4% and 8% are found for respectively the design of cruise and high-thrust for the vanes. The third effect contributes Stokkermans to an unknown effect of radial flow.

This design method could not guarantee a global optimum for the SRV design only after a series of optimizations were performed. Therefore, a design routine was developed by Li with a fast turnaround time and will be discussed in the next section.

2.5.3. SRV MODEL BY LI

The final SRV design method which will be discussed is from Li [3] and will be explained in more detail compared to the previous two models since this method forms the basis of this thesis. Li's design method includes the chord variation along the span and the actual inflow velocity as mentioned by Stokkermans. The design method could be characterized by its fast computational time. An auxiliary function is used where a Lagrange multiplier is multiplied with both the objective function and the constraints. The partial derivative of the auxiliary function is set to zero which minimized the objective function while maintaining the constraints. The

resulting set of equations will be solved which is computationally much faster than performing an optimization routine.

The SRV design method can be divided into three main parts, see figure 2.10. Starting with the velocity input, where the velocity field behind the isolated propeller is obtained using a RANS simulation. The velocity field is taken at the mid-chord location of the SRV. The second part determines the optimal loading distribution on the SRV. Finally, the method includes a design routine for the airfoil sections of the SRV. The design method is able to predict the thrust of the design condition, e.g. the velocity input, but is not capable of analysing off-design conditions, since a new input for the velocity profile will provide a different design output.

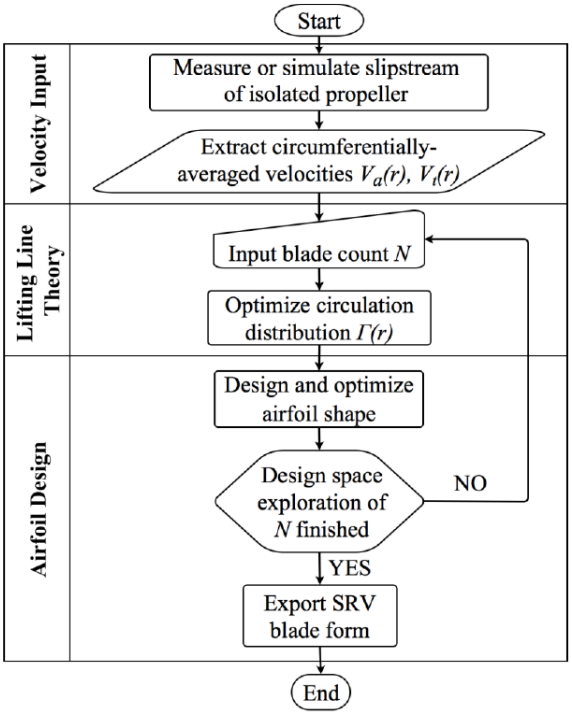

Figure 2.10: SRV design methodology by Li. The three parts contains the velocity input from the propeller slipstream, the Lifting Line Theory to optimize the circulation distribution and finally the airfoil shape optimization [3].

The importance of the velocity profiles can be explained by equation (2.19), here it shows that the axial and tangential input velocities have a direct influence on the thrust production of the SRV. Li uses a generic six-blade propeller, which is typically used in modern turboprops and the layout can be seen in figure 2.11. The propeller has a diameter of 0.406m and the hub has a diameter of 0.084m. The chord and twist distributions are shown in figure 2.12.

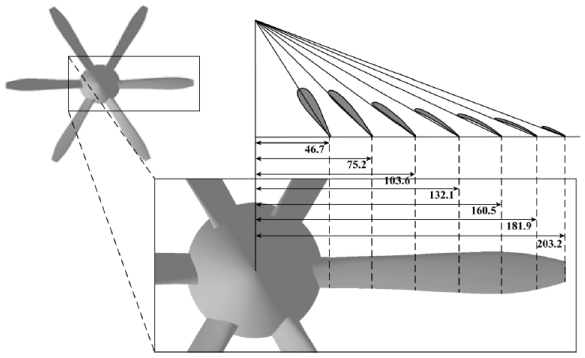

Figure 2.11: Generic six-bladed propeller [3].

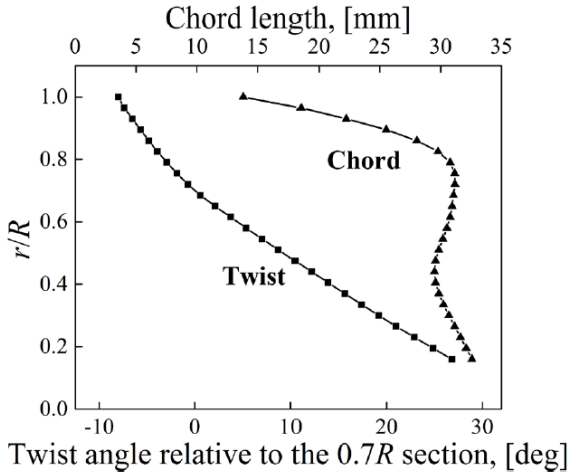

Figure 2.12: Chord and twist distribution along the blade radius of the six-bladed propeller [3].

To model this propeller in a RANS simulation, a domain of 10 times the propeller radius was chosen in the upstream, downstream and radial direction to make sure the boundaries of the domain would not influence the flow field. The free stream velocity was 29 m/s since this was also the maximum attainable speed of the wind tunnel validation experiment. The Reynolds number was based on the free stream velocity and the blade chord length at 0.7R. The wind tunnel has a turbulence intensity of 0.5%. To make sure the RANS simulation would obtain the same level at the propeller plane, an turbulence intensity of 5% was chosen with an eddy viscosity ratio of 10. At the outlet, the static pressure was prescribed to be equal to the undisturbed static pressure. The resulting velocity profiles serve as the input for the second part of the design method and are shown in figure 2.13a and figure 2.13b. They are located at the mid-chord position of the SRVs at an advance ratio of J = 0.6 and a thrust coefficient of $C_{T,P} = 0.322$.

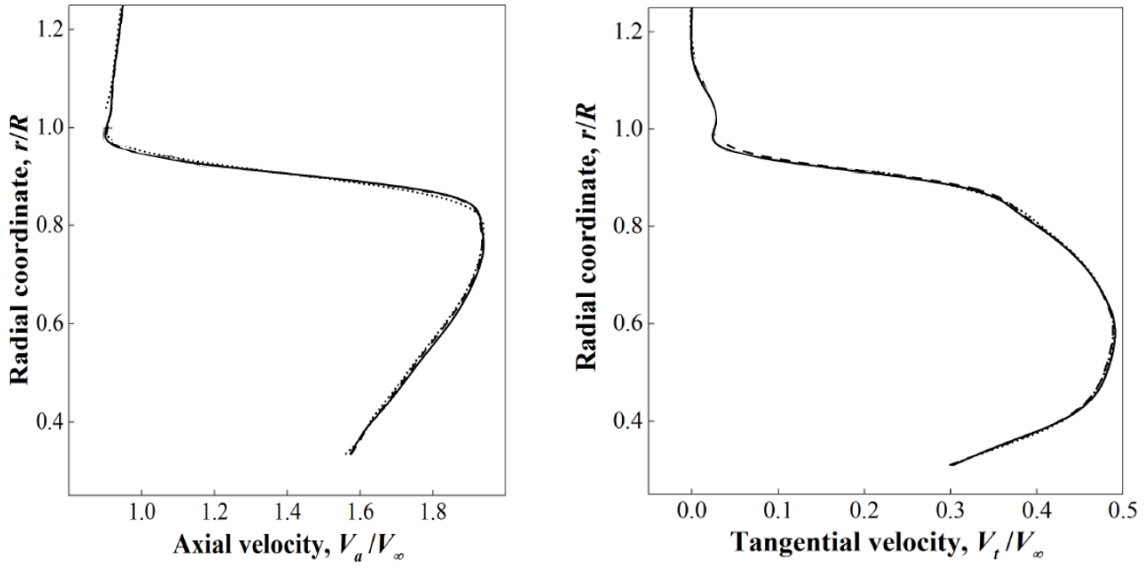

(a) Axial velocity distribution

(b) Tangential velocity distribution

Figure 2.13: Velocity profiles at the location of the mid-chord of the SRV obtained by Li [3].

To determine the optimal circulation distribution of the SRVs, a model is used based on the lifting line theory. As explained earlier, the thrust of the SRV is computed using equation (2.19). Here, the Kutta-Joukowsi theorem is used to compute the lift of the airfoil. The maximum generated thrust of the SRV is calculated by taking the partial derivative of the SRV thrust with respect to the circulation distribution and setting this derivative equal to zero, see equation (2.20). The partial derivative of the thrust is given by equation (2.21).

$$\frac{\partial T_V}{\partial \Gamma} = 0 \tag{2.20}$$

$$\begin{aligned}\frac{\partial T_V}{\partial \Gamma} = (V_t + v_t)\,dr + \sum_i \frac{\partial v_{t_i}}{\partial \Gamma_m}\Gamma_i\,dr_i \\ -\sum_i \frac{1}{2}\frac{\partial V_i^*}{\partial \Gamma_m} C_{d_i} c_i\,(V_a + v_a)\,dr_i \\ -\sum_i \frac{1}{2} V_i^* \frac{\partial (C_{d_i} c_i)}{\partial \Gamma_m}\,(V_a + v_a)\,dr_i \\ -\sum_i \frac{1}{2} V_i^* C_{d_i} c_i \frac{\partial v_a}{\partial \Gamma_m}\,dr_i\end{aligned} \tag{2.21}$$

In equation (2.21), the partial derivatives of the induced axial and tangential velocities to the circulation are called induction factors and are determined using the equations from Wrench [38]. To determine the optimal circulation distribution four unknowns are defined, the circulation, induced tangential and axial velocity and the inflow angle of the blade section. Using the Newton Solver as described in Epps [6], the optimal circulation can be computed, hence the design lift coefficient.

The final part of the SRV design method is optimizing the airfoil shapes of the SRV blade. The airfoil sections are parameterized using five variables based on a NACA 4-series airfoil: the maximum camber h, the chordwise position of maximum camber h_p, maximum thickness t, the chordwise position of maximum thickness t_p and the chord length c. The objective of the airfoil optimization is to minimize the drag of the airfoil while keeping the optimal circulation distribution and is formulated as equation (2.22). With equation (2.23) the lift coefficient can be computed to match the circulation. Using XFOIL [36], the airfoil profile performance can be determined. The corresponding Reynolds number is based on the local inflow velocity and chord length. XFOIL gives an output of the matching angle of attack α and drag coefficient C_d for the design lift coefficient. Besides the drag coefficient at the design point, also the drag coefficient at the stall location is included in the objective function. This is done since the SRV encounters sudden angle of attack increases due to the propeller blade wake [27] [39] and it is desired to have a high stall angle of attack. The weight factors WF_1 and WF_2 are set to 0.5 but could be adjusted if necessary.

$$F(h, h_p, t, t_p, c) = \frac{[(C_d c)_{des}]_{opt}}{[(C_d c)_{des}]_{init}} + WF_1 \frac{[(C_d c)_{stall}]_{opt}}{[(C_d c)_{stall}]_{init}} - WF_2 \frac{[\alpha_{stall} - \alpha_{des}]_{opt}}{[\alpha_{stall} - \alpha_{des}]_{init}} \tag{2.22}$$

$$C_{l_m} = \frac{2\Gamma_m}{V_m^* c_m} \tag{2.23}$$

To obtain the planform of the SRV blade, the airfoil optimization is performed at four sections, the root (r/R = 0.32), the point of maximum circulation (r/R = 0.56), the intermediate section between the point of maximum circulation and the tip (r/R = 0.76) and the tip (r/R = 1.00). The intermediate sections are determined by interpolation with a piecewise cubic Hermite polynomial, resulting in the shapes of the following airfoil profiles when four SRV blades are chosen, see figure 2.14.

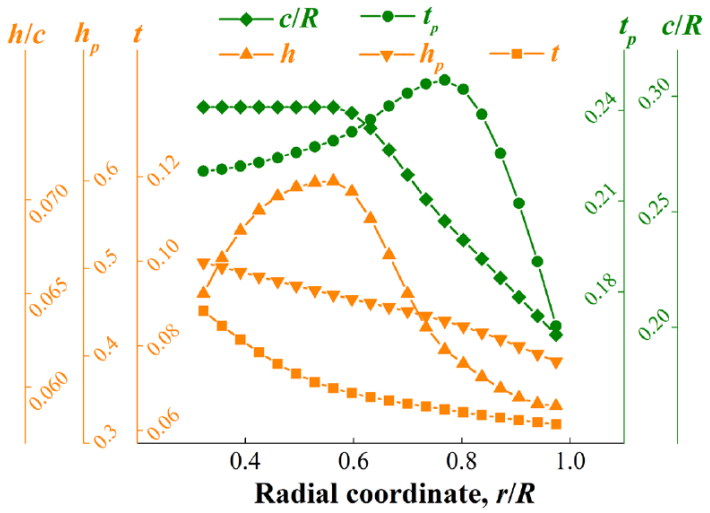

Figure 2.14: Blade shape of the SRV with a blade count of 4 defined by 5 parameters as a function of the radial location r. The maximum camber is h, position of maximum camber is h_p, maximum thickness is t, position of maximum thickness is t_p and chord length is c [3]

The validation of the SRV design model was done using a wind tunnel experiment, which is extensively explained in Li [3]. The output of the wind tunnel experiments is provided in figure 2.15. A very noticeable difference was shown when Li compared his prediction of the lifting line theory and the experiments. At the design condition of J = 0.6, the experiments showed an increase in thrust of 2.6%. However, the predicted thrust by the lifting line theory was 3.4%. With almost a difference of 25%, the lifting line model should be improved.

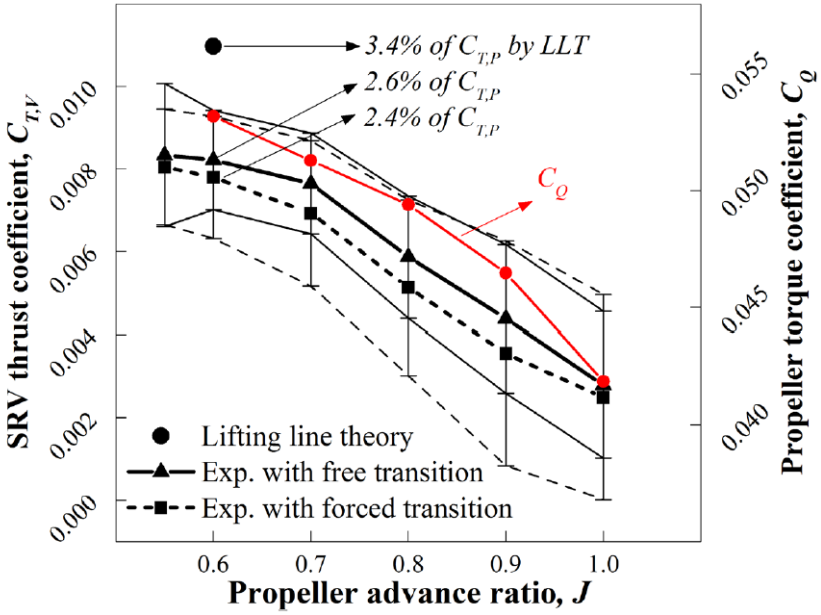

Figure 2.15: Results of thrust prediction of a 4 blade SRV designed for J = 0.6. The black dot represents the design pont and the corresponding thrust prediction based on LLT. The two black curves show the result of two wind tunnel test of the SRV at various advance ratios using a free and forced transition over the blades. Additionally the uncertainty of both experiments are included. The torque coefficient is represented in red [3]

2.6. LIMITATIONS

Despite the regular use of the lifting line theory for simple low-fidelity predictions, when it comes to the propeller-SRV interaction, no accurate thrust prediction is provided, both Stokkermans and Li showed that the lifting line theory over-predicted the thrust compared to CFD or wind tunnel experiments. Veldhuis [4] proposed a swirl correction factor to let the potential flow prediction match with the experimental data. This correction factor was estimated to be 0.5. However, it is empirically based and has no physical meaning. Further, it was difficult to determine the correction factor for arbitrary airfoils. Therefore a more thoughtful correction is required to have a more realistic lift prediction of different airfoils while maintaining the fast computation time of a low-fidelity model.

Li presented a possible solution for the over-prediction and suggested taking the de-camber effect into account because it can affect the lift of a lifting surface. Along the chord line, the local velocity field is changed due to the downwash from the free vortices. However, for the computation of the relative velocity, the lifting line method uses a fixed velocity component at the quarter chord point. The induced velocity by the vortex system of the wake will be higher at the trailing edge compared to the leading edge due to the larger distance of the leading edge to the vortex system. Consequently, the induction of the vortices can be felt as a negative camber for the leading edge of the airfoil and can be referred to as 'decambering' [40]. Sorensen [41] showed that the effect is present, but in terms of performance, the correction for the decambering effect has little influence and thus can be neglected.

One of the main assumptions made, when using the lifting line theory, is that the flow is assumed to continue infinitely far upstream and downstream of the lifting surface. Nederlof [19] showed in his thesis that computing the lift of a wing submerged in the slipstream using the lifting line theory requires a correction due to the limited height of the slipstream and will be further explained in section 2.6.1. Additionally, the propeller-SRV system is located in close proximity to each other. Therefore, also in the axial direction, the slipstream is limited and will be discussed in section 2.6.2.

2.6.1. LIMITED SLIPSTREAM HEIGHT

Nederlof discussed in his thesis the effect of the finite slipstream height of the propeller on the wing [19]. He showed that in the current use of the lifting line theory, a large over-prediction of the lift coefficient in the region of the propeller slipstream can be noticed compared to experimental data. This approach added the axial velocity induced by the propeller to the free stream velocity and a vertical velocity to add the swirl component resulting in a change in the local angle of attack. Using this approach, assumes the flow boundaries to be infinitely far away. But in the case of a propeller slipstream, this assumption is not valid. The propeller has a finite diameter, hence the slipstream also has a finite height.

The correction method to reduce the over-prediction for a 2D airfoil is based on wind tunnel corrections [7], see figure 2.16. Using the system of image reflections the presence of a slipstream boundary can be simulated. These images create a reduction in the circulation of the actual airfoil and thus reduce the lift. However, in the case of the SRVs, the blades are fully submerged in the slipstream. Therefore, the height boundary is defined by the periodicity of the consecutive airfoil blades which can be displayed as a 2D airfoil cascade as shown in figure 2.17. The airfoil blades are no image reflections, thus the method of Nederlof [19] can not be used. Instead, a 2D model for cascade flow is used presented by Weinig [8]. Weinig uses the Kutta-Joukowski theorem for a single airfoil profile and extends it to be used for a profile in a cascade by rewriting the circulation in terms of a velocity difference upstream and downstream of the airfoil cascade. A more elaborate explanation is given in his paper [8].

Before applying Weinig's model to design SRV blades, first, the spacing between the SRV airfoils needs to be determined. The distance between the airfoils can be computed with the equation for an arc length s, see equation (2.24), with a radial distance r along the SRV blade and an angle ϕ (in degrees) between the blades, see also figure 2.17 for the schematic overview of the SRV blades from Li. Using the arc length and the chord distribution for each radial section, the arc length over chord ratio can be computed. Li's SRV design with 4 blades has a ratio of $2 < s/c < 8$, see figure 2.18. The ratio is not going to zero, since a hub radius of the SRV is considered, hence the blade radius is larger than zero.

$$s = \phi(\pi/180)r \tag{2.24}$$

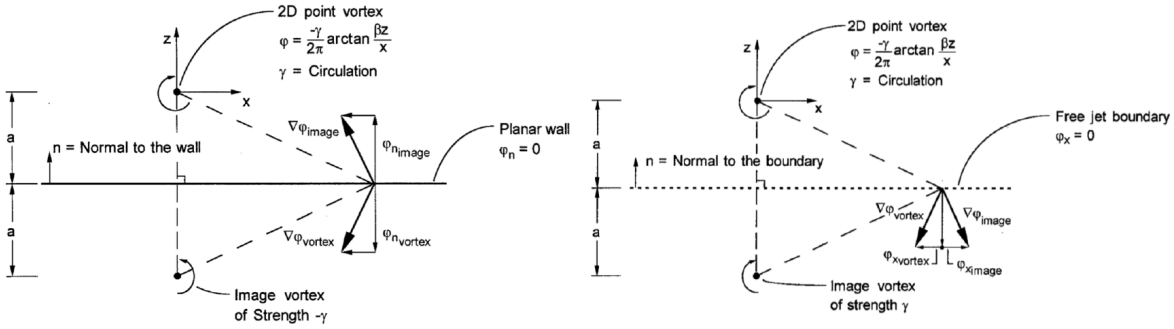

(a) Solid wall boundaries

(b) Free jet boundaries

Figure 2.16: Image vortex system for a solid wall boundary (a) and a free jet boundary (b) to correct the lift prediction due to the presence of the wind tunnel wall [7]

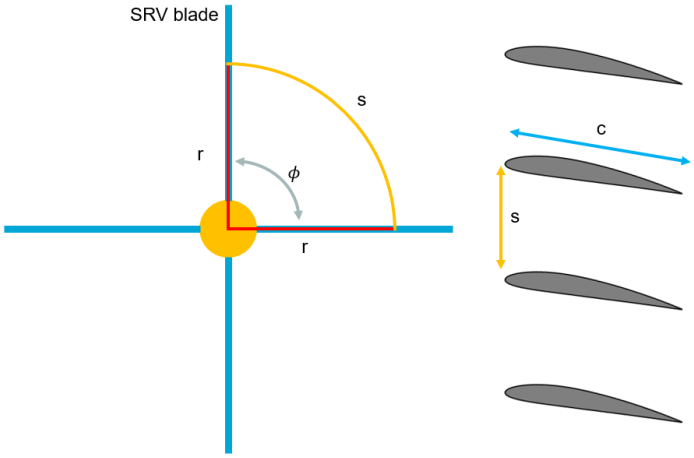

Figure 2.17: Schematic overview of the 4-bladed SRV from Li with a 2D cascade airfoil representation at a radial location r. Where s is the distance between two airfoil and c is the chord length.

In figure 2.19, the interference coefficient (k_1) is plotted against the distance between the cascade airfoils (s/c) and stagger angle (γ). The stagger angle is defined as the angle between the chord line and the axial. Li's SRV blade section has a high pitch angle, towards 90° [3], which results in a small stagger angle. The interference coefficient is defined by the ratio of the cascade airfoil circulation and the single airfoil circulation. In the range of Li's SRV blades, the interference coefficient is equal to 1, meaning the circulation for the airfoil blade in a cascade is equal to the single airfoil circulation.

This coefficient becomes of importance when the chord length of the blade increases or when the arc length reduces due to a higher number of blades. Weinig [8] shows in figure 2.19 that the interference coefficient becomes of importance if the s/c < 2, assuming small stagger angles. Since the majority of the SRV blade sections have a large enough ratio between the cascade distance and chord, it is assumed that the cascade distance does not influence Li's SRV design. However, for larger blade numbers, the cascade interference can probably not be neglected anymore.

2.6.2. AXIAL PROXIMITY OF PROPELLER

The propeller is placed in close proximity to the SRV, thus assuming the flow field of the SRV airfoil extends from minus infinity to plus infinity is not a valid assumption, similar to the limited height of the slipstream. However, the influence of the axial distance between the SRV and the propeller on the propulsive efficiency is not clear.

Starting with a simple propeller-wing configuration. In 1939 Silverstein [42] performed experiments to identify the effect of the distance between the propeller and the wing on the maximum lift coefficient of the wing. The propeller was located at three locations, at a distance of 0.13, 0.25 and 0.4 of the wing's chord length. The

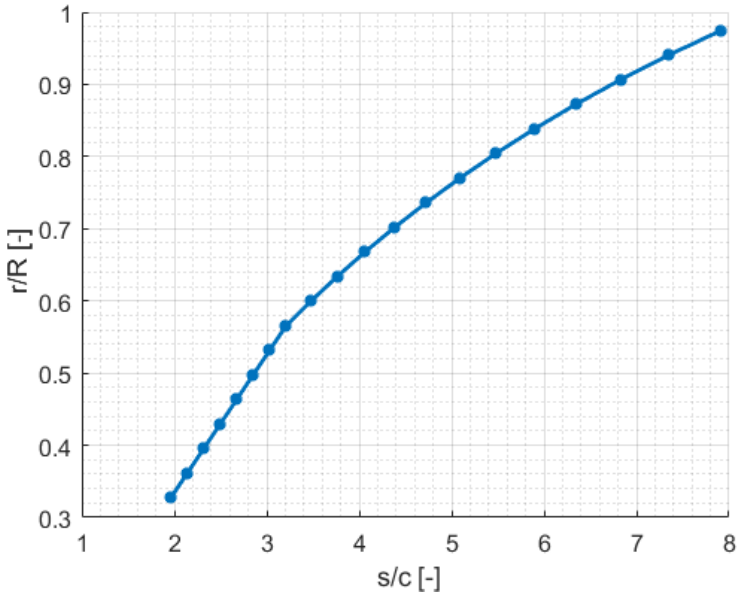

Figure 2.18: Radial distribution of cascade distance (s/c) between two vanes of the 4-bladed SRV design by Li

maximum lift coefficient was the highest for the distance of 0.25 of the wing's chord length. The other two distances reduced the maximum lift coefficient by 2%.

A study from Patterson [43] showed a different behaviour in wing lift when the distance between the propeller and the wing is increased. For axial distances between 0.25 to 1.5 of the wing's chord length, he showed that increasing the propeller-wing distance would also increase the lift of the wing. Patterson attributed the lift increase in slipstream velocity. A wing located at a larger distance from the propeller would result in a large contraction, hence a larger slipstream velocity.

The main message from these two papers is that for a simple propeller-wing configuration the lift changes by varying the axial distance. This indicates that the lift, hence the thrust, also is influenced by the axial distance between a propeller and SRV.

Miller [44] used a 3D Euler code to compute the thrust and efficiency of a propeller with SRV at two locations. The computations were performed for a high-speed cruise at a Mach number of M = 0.8. The two locations of the SRV were not specified but mentioned as 'near' and 'far' from the propeller. Both locations showed an increase in thrust (propeller+SRV). However, the thrust of the smaller distance was almost 2% higher compared to the larger distance. Also, the propulsor efficiency was higher for the forward SRV location.

A slightly adjusted propeller, which required less power compared to Miller's propeller, was tested in a wind tunnel at the same flow conditions (high-speed cruise) by Gazzaniga and Rose [25]. Also, this configuration had two locations for the SRV behind the propeller. The results showed very little difference in thrust coefficient between the two SRV locations. Yamamoto [26] performed numerical calculations for the propeller-SRV configuration used by Gazzaniga and Rose, with the same 3D Euler code as used by Miller [44]. In these calculations, the SRV at the forward location had a lower efficiency compared to the aft location. The over-prediction by the numerical Euler code compared to the wind tunnel experiments was 8.1 % for the forward SRV location and 8.4 % for the aft SRV location, which is a small difference.

In more recent research the effect of the axial distance between the SRV and propeller was discussed by Wang et al. [27]. Although the SRV shapes are simple, still an effect of the varying axial distance was shown. Three axial distances were defined related to the chord: $d_{SRV}/c = 2.0$, 2.5 and 3.0. The total efficiency is the highest for the most aft position and decreases with a shorter distance. It showed that the forward position resulted in a smaller propeller thrust increase due to the SRV. Wang et al. [27], stated that the main reason for the difference would be due to the contractive slipstream zone of the propeller, meaning that the SRV has a smaller effective blockage area with a more forward-positioned SRV. The optimum should lie between the location

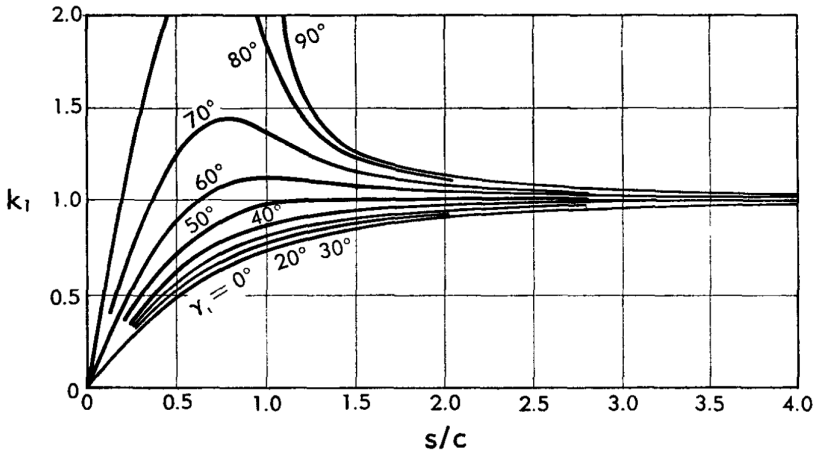

Figure 2.19: Cascade interference coefficient k_1 at different cascade distances (s/c) and stagger angles (γ) [8]

with a weaker block effect (close to the propeller) and the location with low blade interaction (far from the propeller). The same effect of contracting slipstream on the efficiency was discussed by Celik and Güner [45]. When the effect of the slipstream deformation is taken into account, they showed that with increasing axial distance, the propeller efficiency would increase.

The above discussion showed that the axial distance between the propeller and the SRV affects the thrust and propeller efficiency. Yamamoto, Celik and Güner and Wang et al. showed that with increasing propeller-SRV distance, the propeller efficiency would also increase. Gazzaniga and Rose showed no effect due to the axial distance variation and Miller stated that the efficiency would decrease with increasing axial distance. However, a limited amount of axial distances were investigated in the above papers, which could explain the different conclusions. Further, these papers only used 3D methods to compute the thrust or efficiency. In this thesis, the focus lies on capturing the over-prediction between the 2D and 3D models. The next chapter will focus on the difference between a 2D and 3D model due to the limiting axial distance.

3

2D CORRECTION MODEL

The previous chapter shows that using the lifting line theory in the design of SRVs causes an over-prediction in the SRV thrust. The limitation was attributed to the boundaries of the slipstream. The slipstream has a finite height and a finite axial distance, contrary to what is assumed in the lifting line theory, where the flow field extends from minus infinity to plus infinity. Weinig [8] showed that for small distances between the 2D cascade airfoils, this distance needs to be taken into account when the lift of the airfoil is computed by the lifting line theory. However, in the SRV design method of Li [3], the arc length between SRV blades is too large to be relevant in correcting the lift for the influence of the cascade airfoil profiles. The axial distance influences the lift of the SRV blades, but no physical model describes the effect. This chapter will provide a theory which corrects the effect of the axial distance.

3.1. CORRECTION METHODOLOGY

An upstream boundary condition could be imposed by a propeller, as in the case of SRVs, but also by an open jet wind tunnel. At the wind tunnel exit, a flow field is prescribed and if an object is in close proximity, the flow conditions at the nozzle exit will enforce a boundary condition. The lift of a 2D airfoil profile in close proximity to the wind tunnel exit nozzle is already described in 1966 in the AGARDograph 109 [46]. The AGARDograph discusses several corrections to account for the interference due to boundary conditions imposed by the wind tunnel on the lifting surface. The correction that captures the effect of the upstream boundary is presented by Vandrey [47]. Representing the flow field as a combination of a vortex and a source, the interference velocities can be expressed. The distance between the nozzle exit and the vortex point influences the upwash of the vortex and an upwash angle can be defined, see equation (3.1).

$$\Delta\alpha = -\frac{cC_L}{4H}\left[G_0 + \frac{\pi c}{CF \cdot H}\left(\frac{1}{4}\frac{C_m}{C_L}\right)G_1\right] \tag{3.1}$$

It includes the height of the wind tunnel (H), a scaling factor for compressibility (CF), the chord length c, the lift and pitch moment coefficients, C_l and C_m and two functions G_0 and G_1 The functions G_0 and G_1 are dependent on respectively, the axial distance, from the nozzle exit of the open jet wind tunnel and the vortex point of the airfoil, and the distance between the nozzle exit and the collector of the wind tunnel. In AGARDograph 109 [46] the plot of the two functions can be found. Since this approach is rather complex, a more simplified correction was presented by Eitelberg [48].

As mentioned before, the lifting line theory is based on potential flow which assumes that the flow field extends from minus infinity to plus infinity in both horizontal and vertical directions, so-called free flight. In figure 3.1 it is clearly shown what is meant by having boundaries towards infinity up- and down-stream of the airfoil. An airfoil is in a flow field with an angle of attack of 3°. The streamlines are computed using a potential flow simulator from Simon [49]. The streamlines of the flow are shown in blue and at 2 chord lengths upstream and downstream, the flow has approximately the same direction as indicated by the red horizontal lines, since only at minus and plus infinity the up- and down-wash are completely gone. However, if the ve-

locity vector of a streamline is taken at plane P, the velocity has a free stream V_∞ component and an induced component u_i. Using the Biot-Savart law an expression for the induced velocity can be derived.

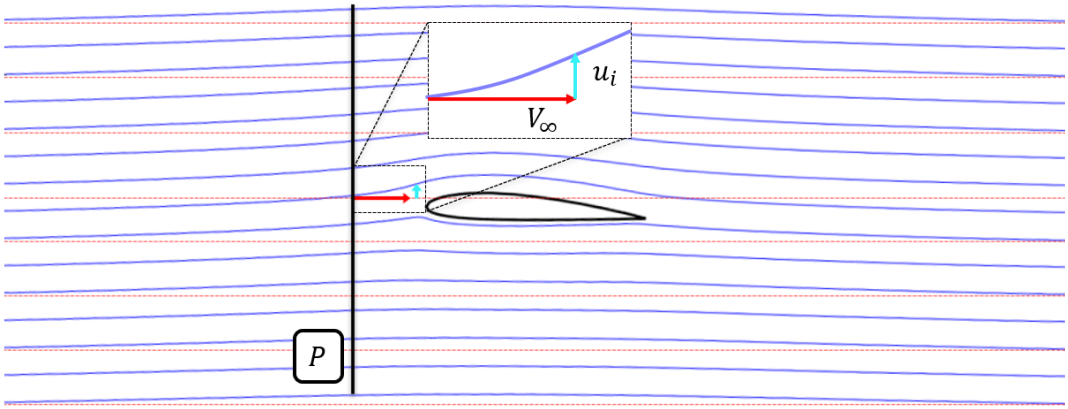

Figure 3.1: Streamlines of the potential flow (in blue) around an airfoil at $\alpha_{FF} = 3°$. In red lines indicate the same distance between the streamlines at the inflow and outflow. At a plane P, the velocity vector is composed into two components.

First, the Kutta-Joukowski theorem (equation (2.16)) is required. Here, the sectional lift can be written in terms of density, far-field velocity and circulation, see equation (3.2). The sectional lift is the amount of lift per unit span. Rewriting this equation and inserting equation (3.2) gives an expression of the circulation in terms of the lift coefficient as is shown in equation (3.3).

$$L' = \frac{1}{2}\rho C_l V_\infty c \tag{3.2}$$

$$\Gamma = \frac{L}{\rho V_\infty} = \frac{C_l \rho V_\infty^2 c}{2\rho V_\infty} = \frac{1}{2} C_l c V_\infty \tag{3.3}$$

To include the upstream distance to the expression, the Biot-Savart law is used. This fundamental relation shows how a vortex filament induces a velocity at an arbitrary point P, located at a distance w from the vortex filament, see figure 3.2. In equation (3.4), the Biot-Savart law is stated, with du_i as the induced velocity at point P, the vortex strength Γ, dk is an infinitely small segment along the vortex filament, w is the distance between the segment dk and point P, d is the distance from point P perpendicular to the vortex filament and k is the distance between point O and the location of segment dk. The full derivation of the Biot-Savart law can be found in for example the book by Karamcheti [50].

$$du_i = \frac{\Gamma}{4\pi} \frac{dk \times w}{|\, w^3 \,|} \tag{3.4}$$

Taking a vortex filament which reaches from minus infinity to plus infinity and computing their influence on the velocity at point P, the Biot Savart Law can be rewritten into equation (3.5). The cross product $dk \times w$ can be written as $w sin(\psi) dk$, where ψ is the angle between dk and w, see figure 3.2. Inserting this into equation (3.5) gives equation (3.6). The distance w and k, as shown in figure 3.2, can also be written in terms of ψ, see equation (3.7) and equation (3.8). Taking the derivative of k, an expression follows for dk, as shown in equation (3.9).

$$u_i = \int_{-\infty}^{\infty} \frac{\Gamma}{4\pi} \frac{dk \times w}{|\, w^3 \,|} \tag{3.5}$$

$$u_i = \frac{\Gamma}{4\pi} \int_{-\infty}^{\infty} \frac{sin(\psi)}{w^2} dk \tag{3.6}$$

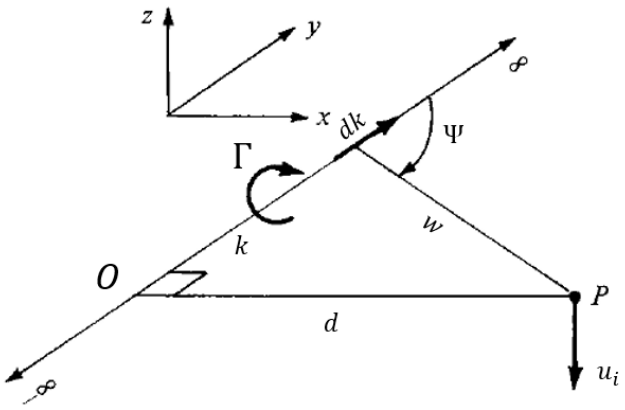

Figure 3.2: Induced velocity (u_i) at point P by an infinite straight vortex filament of strength Γ. The distance between points O and P is indicated by d and the distance between dk and P is w. dk is an infinitely small section along the vortex filament and k is the distance between O and dk. [9]

$$w = \frac{d}{sin(\psi)} \tag{3.7}$$

$$k = \frac{d}{tan(\psi)} \tag{3.8}$$

$$dk = -\frac{d}{sin^2(\psi)} d\psi \tag{3.9}$$

Inserting equation (3.7) and equation (3.9) into the rewritten Biot-Savart law in equation (3.6), results in equation (3.10). Finally, by solving the integral, an expression is found where the induced velocity at a point P is written in terms of the vortex strength Γ and the distance d, between the point P and the vortex filament, see equation (3.11).

$$u_i = \frac{\Gamma}{4\pi} \int_{-\infty}^{\infty} \frac{sin(\psi)}{wr^2} dk = \frac{\Gamma}{4\pi d} \int_{\pi}^{0} sin(\psi) d\psi \tag{3.10}$$

$$u_i = \frac{\Gamma}{2\pi d} \tag{3.11}$$

The thin airfoil approximation can be written as equation (3.12), where α_{FF} is the far field angle of attack and $\alpha_{C_l=0}$ is the offset when the zero lift angle of attack is not equal to zero. Combining equation (3.12) and equation (3.3) with equation (3.11), the induced velocity can be written as stated in equation (3.13). Cleaning up this equation gives equation (3.14). For small angles, it can be assumed that $sin(\alpha_{corr}) = \alpha_{corr}$. Therefore, the induced velocity divided by the free stream velocity is equal to α_{corr}, resulting in an expression for the correction angle of attack, see equation (3.15) [48].

This equation shows the amount of rotation required to correct the 2D potential flow approximation accounting for a flow field predetermined in close proximity to the leading edge of the airfoil. It has to be noted that, for airfoils, the distance needs to be taken from the location of the boundary to the quarter chord point since this is the location of the representative vortex of the airfoil.

$$C_l = 2\pi(\alpha_{FF} - \alpha_{C_l=0}) \tag{3.12}$$

$$u_i = \frac{\Gamma}{2\pi d} = \frac{\frac{1}{2} C_l c V_\infty}{2\pi d} = \frac{\pi(\alpha_{FF} - \alpha_{C_l=0}) c V_\infty}{2\pi d} \tag{3.13}$$

$$u_i = V_\infty \frac{(\alpha_{FF} - \alpha_{C_l=0})}{2} \frac{c}{d} \tag{3.14}$$

$$\alpha_{corr} = \frac{(\alpha_{FF} - \alpha_{C_l=0})}{2} \frac{c}{d} \tag{3.15}$$

3.2. VALIDATION

To verify the expression for the angle of attack correction, the lift polars from the AWB wind tunnel test in figure 3.4 are used [10]. The multi-element airfoil has a high camber configuration, which means that the zero-lift angle of attack is not equal to zero anymore and thus the offset angle needs to be computed.

The result of a CFD simulation is shown in figure 3.3, where an open wind tunnel jet defines the upstream velocity profile in close proximity to the airfoil. Comparing this flow field of the airfoil with the potential flow field in figure 3.1 a clear difference can be seen that upstream of the airfoil in the wind tunnel has a straight outflow with a velocity vector perpendicular to the nozzle exit plane. While for the potential flow, the flow will have an up-wash component in the velocity at this location in front of the airfoil. Downstream of the airfoil of the wind tunnel, a strong additional downwash can be noticed compared to the potential flow. With a straight outflow and an additional downwash, it seems that the airfoil in the potential flow field case should be rotated to match the flow field from the wind tunnel, just as was found in the expression by Vandrey [47] and Eitelberg [48].

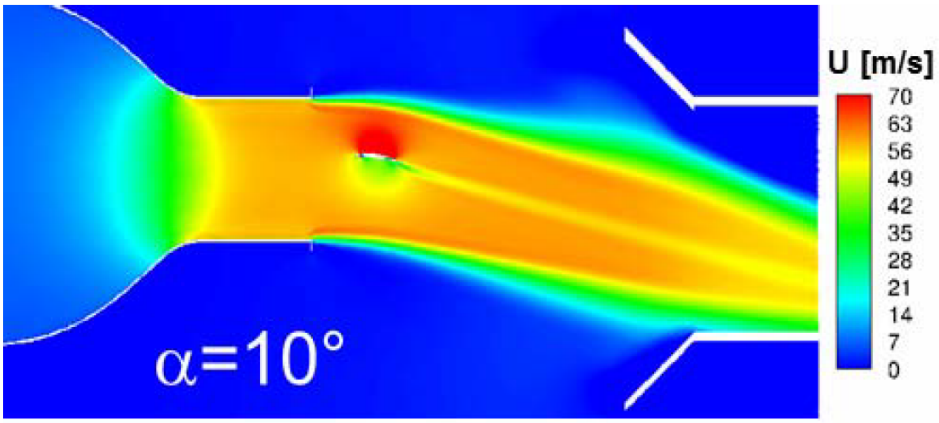

Figure 3.3: Mean velocity of a 2D airfoil in the AWB wind tunnel. [10]

Taking a closer look at the lift polar of the airfoil, the necessity of a rotation is confirmed. The lift polar for the wind tunnel experiment is shown in figure 3.4 [10]. The graph shows three different lift polars, the experimental measurements, 3D RANS (including the wind tunnel) and 2D RANS (free-flight). The free-flight condition can also be labelled as the potential flow solution with an unbounded flow field. The 3D simulation matches closely with the experimental data, however, when the effect of the wind tunnel is neglected, which is the case for the 2D RANS data, the lift is much higher for the same angle of attack. As can be seen in figure 3.4, the slope of the three polars are roughly the same. This means that if the angle of attack of the bounded domain (3D RANS) is increased, the same lift coefficient can be obtained as in the unbounded domain (2D RANS).

To compute the angle of attack for the airfoil in the wind tunnel, while maintaining the same lift as in the 2D RANS simulation, the correction angle of attack is added to the free stream angle of attack, see equation (3.16).

$$\alpha_{WT} = \alpha_{FF} + \alpha_{corr} \tag{3.16}$$

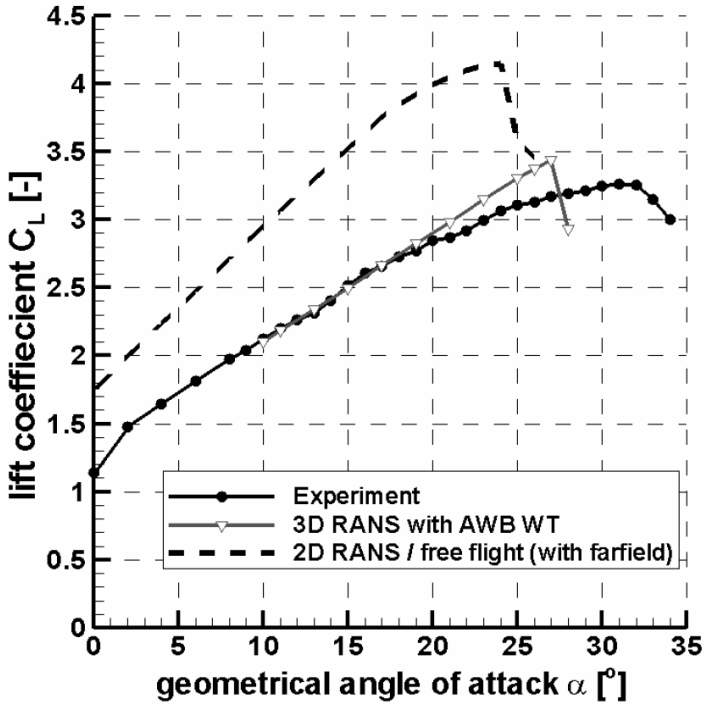

Figure 3.4: Lift curves of the experiment (black dotted line), 3D RANS (gray dotted line) and 2D RANS (dashed line) simulations for an airfoil section in the AWB wind tunnel [10]

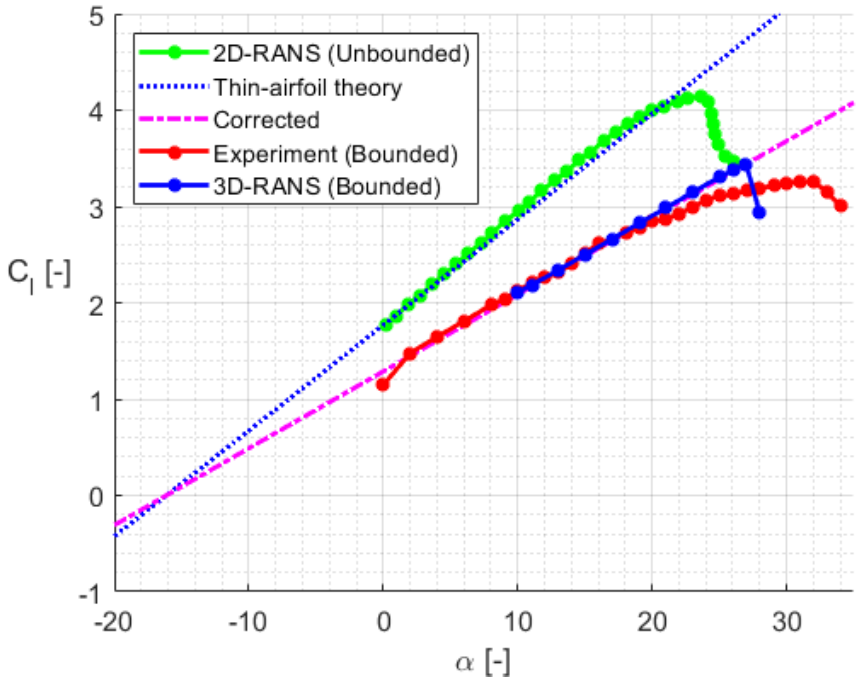

Figure 3.5: Lift curves of an airfoil in the AWB wind tunnel, red, blue and green dotted lines for respectively the results of the experiments,3D-RANS and 2D-RANS. Including the thin airfoil theory lift curve in dashed blue and the corrected lift curve in pink

To prevent an extrapolation over more than 15 degrees, the 2π lift slope, as assumed in the thin airfoil theory, was shifted to match the lift coefficient at zero angle of attack. As can be seen in figure 3.5, the lift slope of the multi-element airfoil can be well approximated with the thin airfoil theory and holds until an angle of attack of 20°. The zero-lift angle for this multi-element airfoil is $\alpha_{C_l=0} = -16.1°$. To compute the correction, the chord length and axial distance between the nozzle and the quarter chord point are required. For this experiment, they are 0.3m and 0.44m, respectively the chord length and the axial distance. The result of the corrected lift slope is also plotted in figure 3.5. The corrected lift slope shows very good agreement with the experimental and 3D RANS data. This proves that the correction method can capture the effect of the upstream boundary condition in the linear regime of the lift curve slope.

3.3. LIMITING CASES OF CORRECTION

The correction shows a good approximation, however, it is an approximation thus it is not for every condition applicable. Firstly, due to the usage of the Biot-Savart law, the angle of attack correction only holds for the stagnation streamline of the airfoil. Secondly, the consequence of using a lift slope of 2π is that the correction only holds for the linear part of the lift curve. Thirdly, the assumption of the thin airfoil theory, means that the approximation is only valid for airfoils with a small thickness. As demonstrated in figure 3.6, the thickness of a symmetric airfoil is increased and the lift coefficient deviates more from the 2π lift curve. When designing the airfoil profiles of the SRV, this should be taken into account to check the validity of the correction.

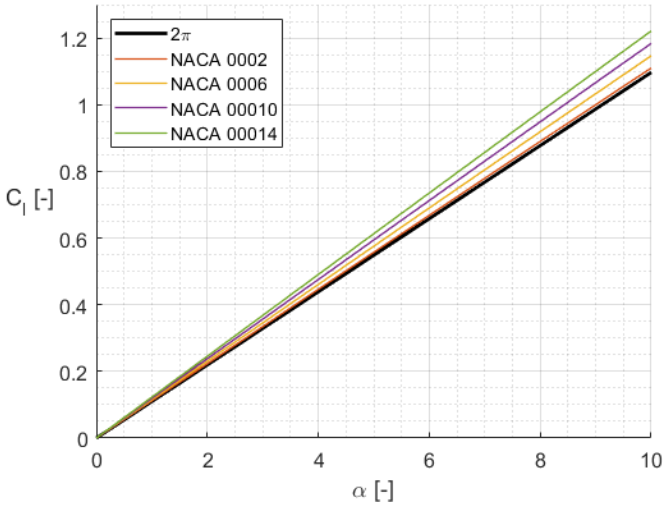

Figure 3.6: 2π lift slope compared to symmetric NACA airfoils at varying thickness

The influence of the axial distance, between the location of the boundary condition and the airfoil, on the correction, is presented in figure 3.7. The sectional lift coefficient is normalised with the far field lift coefficient of the airfoil, which makes the graph independent of any airfoil shape. The angle of attack was chosen to be $\alpha_{FF} = 2°$. The red line represents the far field condition where no correction is applied. The graph shows that the far-field lift coefficient will be approached when the axial distance increases. The gradient of dC_l/dr becomes stronger when the axial distance is reduced. When the axial distance becomes d/c = 0.5, the correction angle will be equal to the free stream angle of attack, according to equation (3.15). This results in a wind tunnel angle of attack (α_{WT}) which is twice the free stream angle of attack. The nozzle boundary condition defines the angle of the stagnation streamline, meaning the induced upwind is fully suppressed.

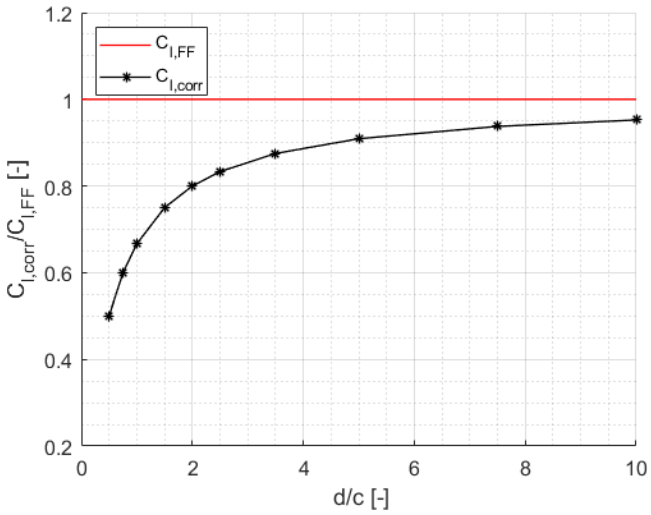

Figure 3.7: The influence of varying axial distance on the lift coefficient normalized with the far field lift coefficient of a 2D airfoil profile

4

SRV DESIGN INCLUDING 2D CORRECTION

The different methods, discussed in chapter 2, used to design SRVs with the lifting line theory had an over-prediction in the thrust of the lifting line results compared to either the CFD or the wind tunnel experiments. With the SRV being in close proximity to the propeller the upstream boundary condition could be an explanation for the large over-prediction of the thrust. Rotating the blade of an airfoil section from the 2D solution showed good agreement with the 3D experiments, see section 3.2. However, the SRV is a blade in 3D, hence, the 2D correction expression determined in chapter 3 will be implemented in the SRV design routine in this chapter.

4.1. IMPLEMENTATION IN SRV DESIGN ROUTINE

The design routine for SRV will be based on the method of Li [3] as discussed more elaborately in section 2.5.3. The upstream distance between the propeller outflow plane and the quarter chord point is shown in figure 4.1. Due to the taper ratio of the SRV blade of 2/3, both the upstream distance and the chord of the SRV blade vary, resulting in a d_{SRV}/c ratio between 0.38 and 0.56 for this propeller-SRV configuration. The correction method predicts for these ratios a large drop in the lift, as shown in figure 3.7, therefore the correction method is necessary for this propeller-SRV configuration.

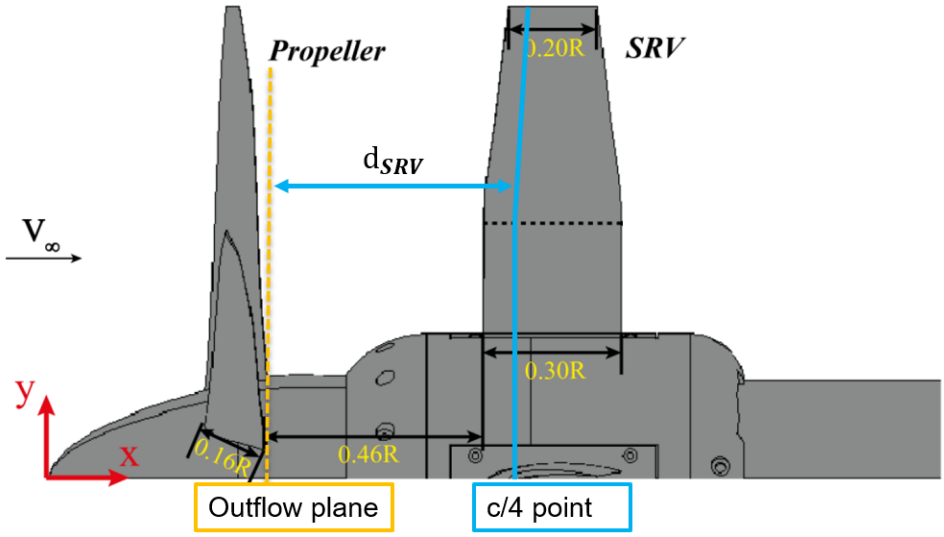

Figure 4.1: Sketch of propeller-SRV layout adjusted from Li with the propeller outflow plane in yellow and at a distance d_{SRV}, the quarter chord line of the SRV in blue [3]

Li provided velocity profiles as input for the Newton Solver. These profiles are located at the mid-chord position of the SRV. To apply the correction, strictly speaking, a negative distance needs to be used since the

location of the vortex of the airfoil is in front of the boundary condition. However, this is not realistic, so it is assumed that the velocity distribution of figure 2.8 is the same at the location of the propeller outflow plane as defined in figure 4.1.

The available data of the work of Li showed that for a lower thrust setting ($T_{C,P}$ = 0.0294), compared to the propeller thrust of the design point ($T_{C,P}$ = 0.322), the tangential and axial velocities do not vary much at different axial distances behind the outflow plane, see figure 4.2. This would prove that the assumption of shifting the velocity profile from the mid-chord to the propeller outflow plane is valid. However, the development of the slipstream is depended on the magnitude of the thrust force. This was already shown in section 2.3.1, where the pressure increase results in the thrust force. The graph shows also that the pressure converges towards the free stream pressure after the actuator disk. This convergence will be reached at an earlier location behind the propeller plane for a lower thrust compared to a higher thrust, because of the smaller pressure jump at low thrust. Therefore, the development of the slipstream at the design thrust setting could result in different velocity profiles. This is however beyond the scope of this thesis and would be useful for further work.

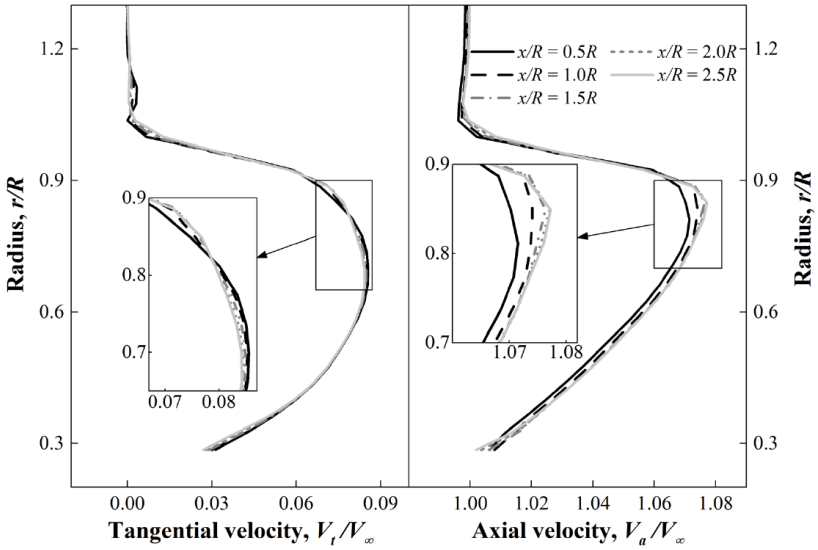

Figure 4.2: Radial velocity distributions of the circumferential-averaged tangential and axial velocity at various distances in the propeller slipstream at J = 2.4, $T_{C,P}$ = 0.0294 and $\beta_{0.7R}$ = 50° [3]

To compute the correction angle of attack, several inputs are required. The axial distance, the chord length and the zero lift angle of attack. The zero lift angle of attack is dependent on the airfoil profile and thus the correction angle of attack is computed after the aerodynamic performance of the airfoil profile is known.

To recall the steps taken in the design routine, the circulation distribution was one of the outputs of the Newton solver. Using the circulation in combination with the inflow velocity, profile shape and chord length, the lift coefficient is calculated. This is the design lift coefficient and at this design point, the drag is minimised. Besides the drag also the angle of attack is computed at the design point with XFOIL [36]. This angle of attack is the free stream angle of attack. With the known lift polar also the zero lift angle of attack of the airfoil profile can be determined. With all the variables known, the correction angle of attack can be computed.

The design diagram presented by Li in figure 2.10 can be adjusted with the implementation of the correction, as is shown in figure 4.3. Instead of computing the angle of attack corresponding to the design lift coefficient and then adding this angle of attack to the inflow angle to obtain the pitch angle, first, the correction angle needs to be computed. Using the free stream angle of attack, the chord distribution and the pre-determined axial distance, the correction angle is computed following equation (3.15), where $d = d_{SRV}$. Consequently, a new pitch angle is computed by adding the correction angle to the inflow angle (θ) and angle of attack (α_{FF}).

The previous chapter showed that for a constant angle of attack, the lift would decrease when the axial distance becomes smaller. With the correction angle of attack known, also the lift for each section of the blade can be computed for the uncorrected case, to check if this would be similar to the thrust prediction of Li's wind tunnel experiments.

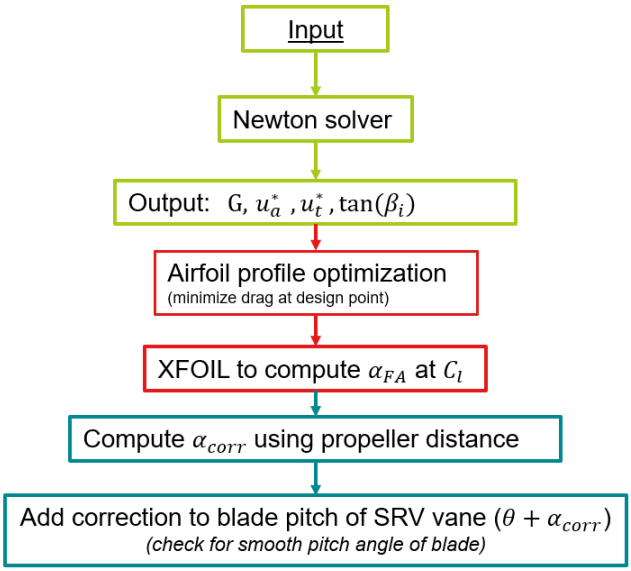

Figure 4.3: Chain diagram of adjusted design procedure. The green boxes indicated the optimization of the circulation distribution, in red the airfoil optimization and in blue the addition due to the correction angle

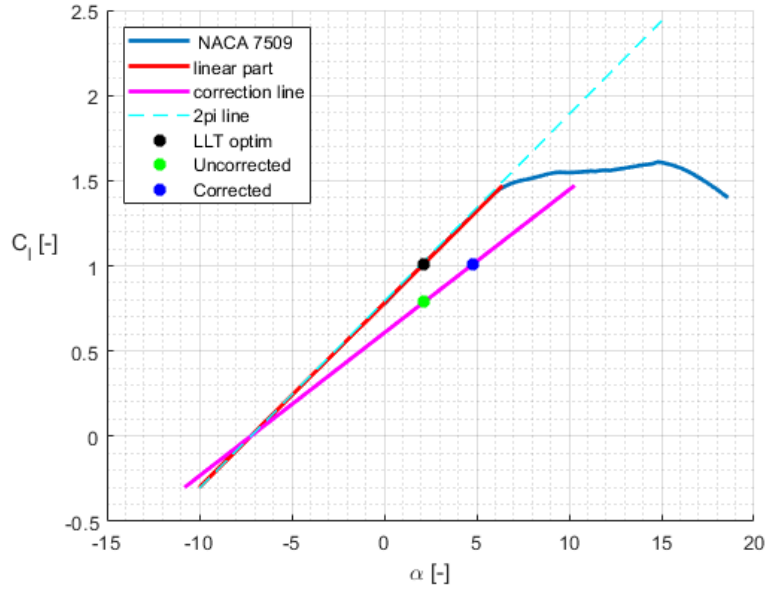

Figure 4.4: Lift polar of the root airfoil (NACA7509) of the SRV by Li in blue. The red line indicates the linear part of the lift polar and in light blue is the thin airfoil lift curve plotted. The corrected lift curve is in pink and the three dots, black, green and blue are respectively the optimal prediction by the LLT, the uncorrected lift and the corrected lift.

To illustrate the application of the correction, for an airfoil section of the SRV blade, figure 4.4 can be used. In dark blue, the lift polar of the NACA 7509 is plotted, according to the blade shape of the root airfoil profile, see figure 2.14. The Reynolds number is based on the chord length of the section and the local inflow velocity V^*. The red line represents the slope of the linear part of the lift polar since the correction assumes to be in the linear regime. To determine the linear part, a function is used to find abrupt changes in the data of the lift polar. By adjusting the threshold a good prediction can be given of the linear slope. In light blue, the lift curve with a slope of 2π is plotted and shifted to match the zero lift angle of attack. Finally, in purple, the

corrected lift curve is plotted based on the 2π lift slope for the given chord length and upstream distance. The lift coefficient of the design point is represented by the black point. If no angle of attack correction would be applied, the circulation, hence the lift coefficient, would be lower than the desired circulation for the optimal performance (minimum induced losses) as is indicated by the green point, the so-called uncorrected case. Hence, the thrust of the SRV is lower than predicted. The blue point, the corrected case, shows how this can be resolved by accounting for the angle of attack difference in the selection of the vane pitch angle. The same lift coefficient is again obtained as the initial design point but at a higher angle of attack.

4.2. ADJUSTMENT IN AIRFOIL PROFILE OPTIMIZATION

To make the SRV design routine complete, the airfoil design needs to be included. The airfoil shape is required to determine the zero lift angle of attack to compute the correction angle in equation (3.15). The airfoil design is also based on the work of Li [3], see section 2.5.3. The airfoil design is the final part of the SRV design routine presented by Li. As explained in section 2.5.3, the airfoil sections are based on a NACA 4-series and are parameterized using five variables: the maximum camber, the chordwise position of maximum camber, maximum thickness, the chordwise position of maximum thickness and the chord length. At four representative sections (the root, the point of maximum circulation, a point between the maximum circulation and the tip and the tip) the airfoil profile is optimized to minimize the sectional drag and have a large margin from the design angle of attack to the stall angle of attack, see equation (2.22).

In the current airfoil optimization, an adjustment was required compared to Li's work. Li defined the stall angle of attack at the location of maximum lift coefficient, see the blue points in figure 4.5. However, in the optimization, it was found that at some combinations of airfoil profile and Reynolds number, XFOIL could not converge for all angles of attack and thus presented an incomplete lift polar. In some cases, the incomplete lift polar could be solved with extrapolation if the required values were close to the data of XFOIL. Still, this was not always the case and thus a new definition was required. XFOIL has difficulty in the prediction of the lift and drag at the stall region and to avoid that region, the stall angle of attack is defined as the point where the lift polar is not linear anymore as can be seen by the red points in figure 4.5. For the NACA 8508, in green, the two definitions of the stall angles result in not a large difference, only 0.2°. However, in the case of the NACA 6407, in blue, the difference in stall angle definitions is 4.6°. Still, XFOIL is not fully converged, since the lift polar abruptly ends without clearly showing the drop in lift due to stall. To make the optimizer more robust, it was required to define the stall angle at the end of the linear slope of the lift polar.

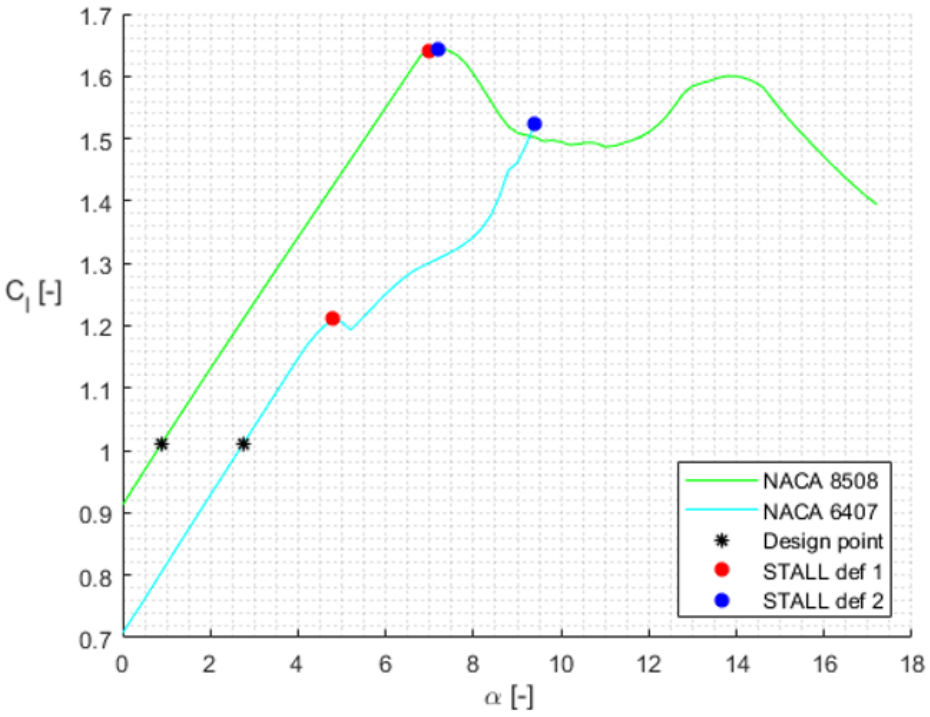

Figure 4.5: Two lift curves of airfoil computed by XFOIL using two different definitions of the stall angle (red and blue dot). The design point is indicated the black star.

4.3. VALIDATION

Since the results in the work of Li [3] are only presented in terms of thrust, the uncorrected and corrected lift coefficient or circulation can not be compared. Therefore the thrust needs to be computed using the circulation for the uncorrected and corrected case, recall the green and blue point in figure 4.4. The corrected line of the lift polar, see the pink line in figure 4.4, can be used to compute the circulation for the two cases (uncorrected and corrected) using equation (3.3). The resulting circulation will then be inserted in equation (2.19) to compute the thrust of the SRV. The designs of the SRV are kept the same, only for the corrected case, the pitch angle is higher due to the addition of the correction angle. The uncorrected and corrected thrust together with the thrust results from Li are shown in table 4.1. Li's thrust prediction with the LLT model compared to the wind tunnel experimental over-predicts the SRV thrust by 26% which is a difference of 0.8% in reference to the propeller thrust. The newly computed thrusts match well with Li's predictions. The uncorrected case has only a fraction lower thrust compared to Li's wind tunnel experiments, but the difference is negligible for the use of the correction method. When the correction angle is included and the pitch angle has increased, the corrected case obtains the same thrust value as the initial optimal design point. Both cases match with the results from Li, proving that the correction approach is not only valid for the 2D airfoil, but could also be used in 3D blade design.

Table 4.1: Thrust of SRV predicted by Li's experiments and the correction for J = 0.6 and $C_{T,P}$ = 0.322

	$C_{T,V}$ [−]	T_V / T_P [-]
Li - LLT	0.0109	3.4%
Li - Wind tunnel	0.0084	2.6%
Corrected	0.0109	3.4%
Uncorrected	0.0083	2.58%

5

RESULTS

This chapter will discuss the results of the corrected SRV design routine. In section 5.1 the correction angle distribution will be discussed including a comparison of the location of maximum correction with the maximum circulation. Also, a part will be attributed to irregularities in the distribution of the correction angle. Follow by section 5.2 where the impact of the correction on each section is discussed. So far, each blade section was corrected by an individual correction angle, however, due to structural and manufacturing reasons, it could be necessary to limit the correction by turning the full blade over a fixed angle. This will be discussed in section 5.3. The results are taken based on the work of Li, where the design condition of the propeller was at high thrust, J = 0.6, $C_{T,P} = 0.322$ and $\beta_{0.7R} = 30°$. In section 5.4 the advance ratio of the design point is varied to identify its influence on the correction. Not enough data was available of the N250 propeller at various advance ratios. Therefore in this section, the APIAN propeller is used with the velocity profiles of Stokkermans [2] varying between J = 0.95 and J = 1.8. Finally, some new insights are provided on the airfoil design from Li's SRV design routine in section 5.5 and the main conclusions of the results can be found in section 5.6.

5.1. RADIAL DISTRIBUTION OF CORRECTION

In section 4.3 the correction was applied for each blade section separately, therefore this section will show the distribution of the required airfoil rotation along the blade. The distribution of the correction angle is compared with the circulation distribution in figure 5.1. Each graph shows three distributions. In blue, the angle of attack and circulation is computed using the far field assumption, where there is no boundary applied in the axial distance. In red, the distribution of the correction angle of attack is shown in figure 5.1a and for the circulation, in figure 5.1b, the red curve shows the distribution in the uncorrected case, meaning that for the same angle of attack a lower circulation is obtained, as discussed in chapter 3. Finally, in yellow, the correction angle is added to the far field angle of attack. For the circulation, the added correction angle to the far-field angle of attack gives the 'original' far-field circulation back.

There is a small difference in the location of the maxima. The maximum circulation is located at a radial distance of $r/R = 0.566$ and the maximum correction is located at $r/R = 0.497$. The correction is dependent on the free stream angle of attack, chord and axial distance. Looking at figure 5.2a, the chord is for both radial positions equal and therefore also the axial distance. The angle of attack of the blade section is determined by XFOIL, which is based on the input of the design lift coefficient, equation (2.23). At the location of maximum circulation, the Γ/V^* ratio is lower than at the location of maximum correction. Therefore the lift coefficient is higher at $r/R = 0.497$, which is also seen in figure 5.3a, resulting in a higher angle of attack, and thus also a higher correction angle. Still, the difference in locations is small, meaning the correction angle has a similar distribution as the circulation from the root to 3/4 of the span, which is a feasible result.

The final sections close to the tip, show an irregularity in the angle of attack and the lift coefficient, see figure 5.1a and figure 5.3a respectively. Consequently, this also impacts the pitch angle as can be seen in figure 5.3b. This seems odd since the circulation, chord and velocity distribution are smooth curves. However, taking a closer look at the velocity profile in figure 5.2b, it can be noticed that the sections at the tip have a large drop in velocity, which is larger compared to the distribution for the chord and the circulation. The

larger gradient of the inflow velocity to the radial position makes the denominator in equation (2.23) smaller and therefore the lift coefficient increases.

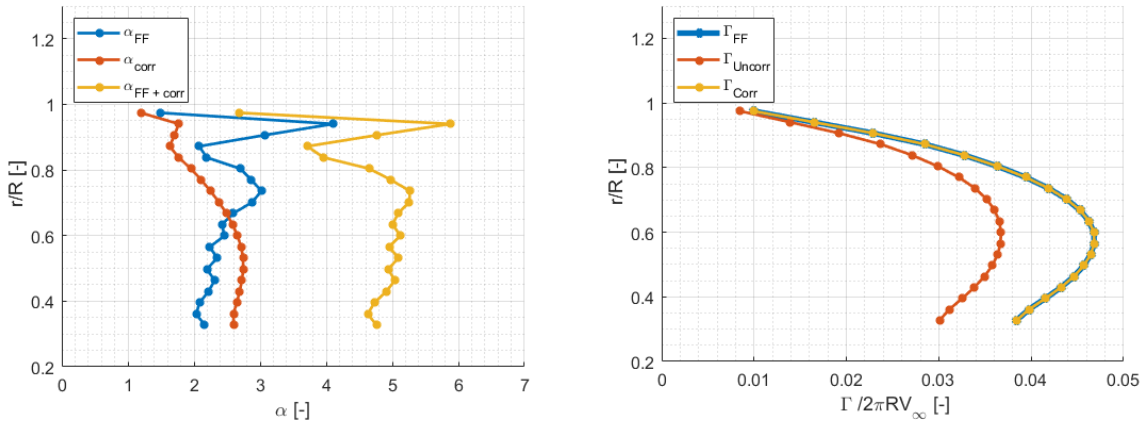

(a) Angle of attack distribution

(b) Circulation distribution

Figure 5.1: The angle of attack and correction (a) and circulation (b) distribution of the SRV blades

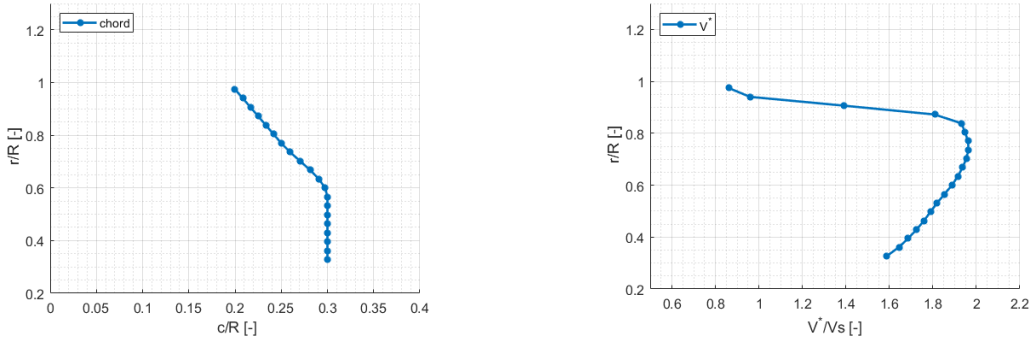

(a) Chord distribution

(b) Magnitude of inflow velocity

Figure 5.2: The chord distribution (a) and magnitude of the inflow velocity (b) of the SRV blades

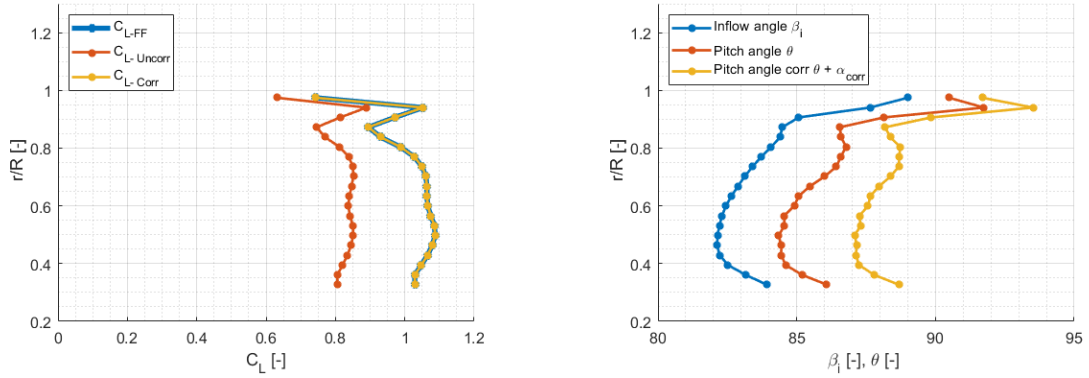

(a) Lift distribution

(b) Pitch angle

Figure 5.3: The lift coefficient distribution (a) and the pitch distribution (b) of the SRV blades

The location of the local peak in lift coefficient can be identified using more radial sections across the blade. In figure 5.4 the number of radial sections has increased from 20 to 100. The velocity distribution has a very steep slope close to the tip, meaning that a small error margin of the radial coordinate will cause a large velocity error. Between the radial point of r/R = 0.9 and r/R = 1.0, a local minimum in velocity can be seen. The drop in velocity is due to the input velocity profiles, see figure 2.13a and figure 2.13b. The minimum of this drop is at the same location as the local lift peak at the tip.

By adjusting the velocity profile, the local peak at the tip of the lift coefficient distribution can be removed and the distribution will become smooth. This is not only necessary to have a better approximation of the real lift coefficient distribution, but also will it provide the correct pitch angle distribution for the vanes. In future work, where the thrust of SRVs should be simulated using high-fidelity models, it is required to have the right pitch distribution to be able to make a valid comparison of the thrust predictions between the low- and high-fidelity models.

A polynomial of the 5^{th} order is fitted through the velocity distribution, by keeping all the radial sections until r/R = 0.85 and including the final radial section at r/R = 1.0. The fit of the polynomial for the inflow velocity V^* can be seen in figure 5.5a. The computed lift coefficient distribution with the adjusted inflow velocity profile is plotted in figure 5.5b. As can be seen, the steep peak is removed and the blade has a much smoother lift distribution, which is desired for an SRV blade.

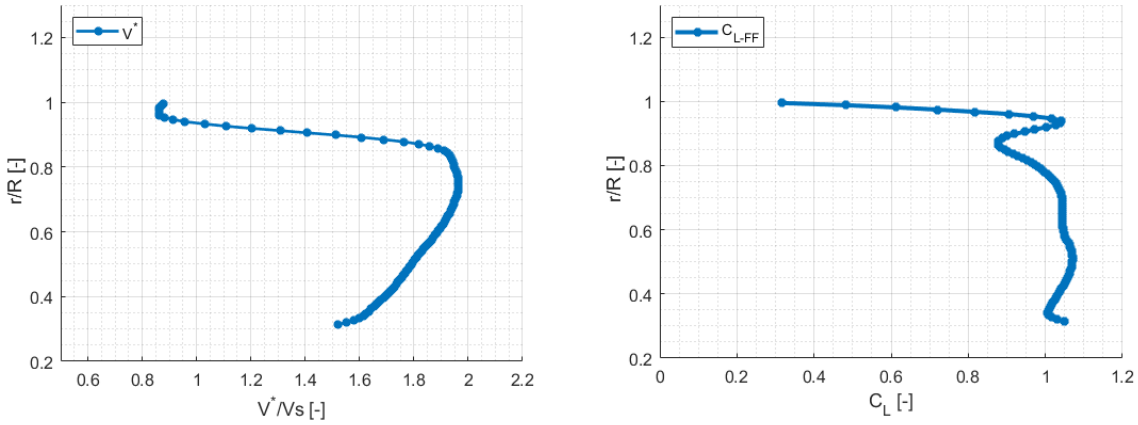

(a) Inflow velocity distribution

(b) Lift distribution

Figure 5.4: The magnitude of the inflow velocity (a) and the lift distribution (b) with 100 radial sections

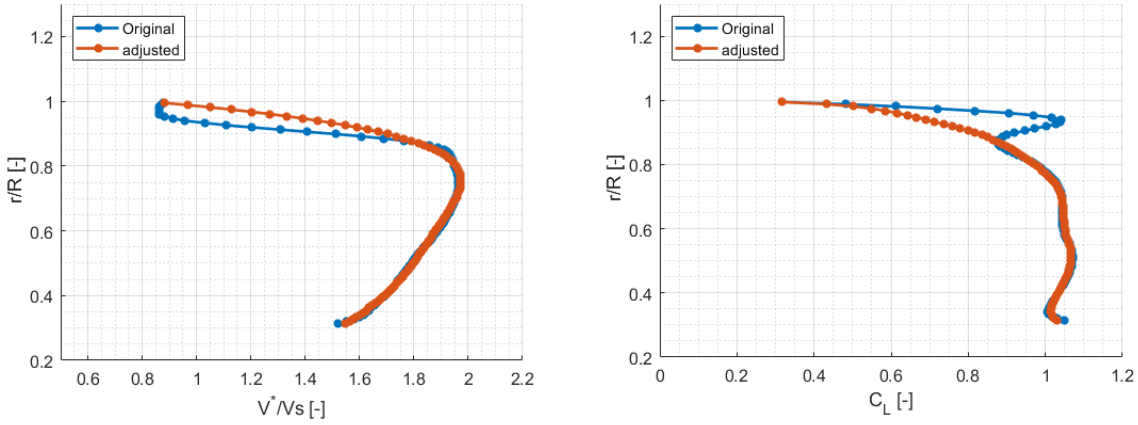

(a) Inflow velocity distribution

(b) Lift distribution

Figure 5.5: A polynomial fit for the magnitude of the inflow velocity (a) and the resulting lift distribution (b) with 100 radial sections adjusted

In figure 5.6a, the angle of attack and correction angle distribution is shown again but here the smooth lift distribution is used. In figure 5.6b the pitch distribution is presented. In both graphs, the steep peaks are removed which results in a more feasible distribution. In figure 5.7 the circulation distribution is shown and remains unaltered.

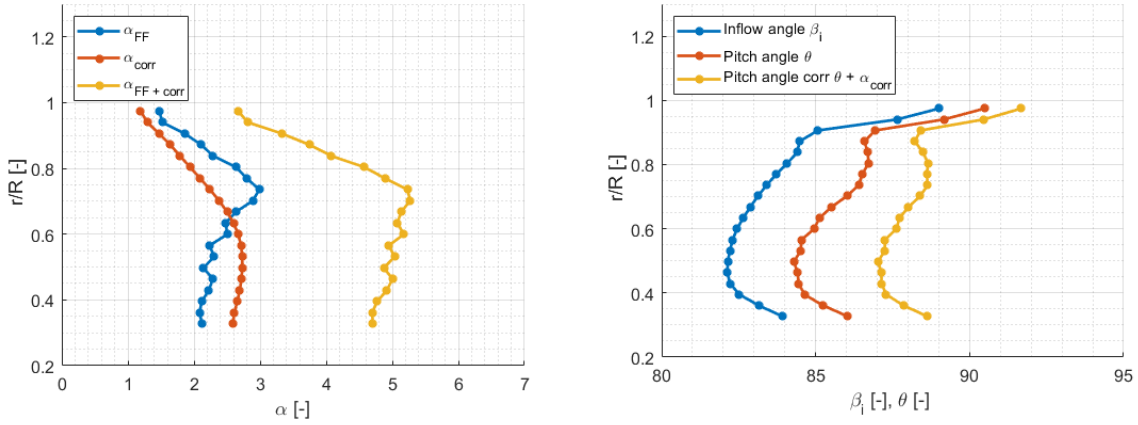

(a) Angle of attack distribution

(b) Pitch angle distribution

Figure 5.6: The angle of attack distribution (a) and pitch distribution (b) with 20 radial sections adjusted

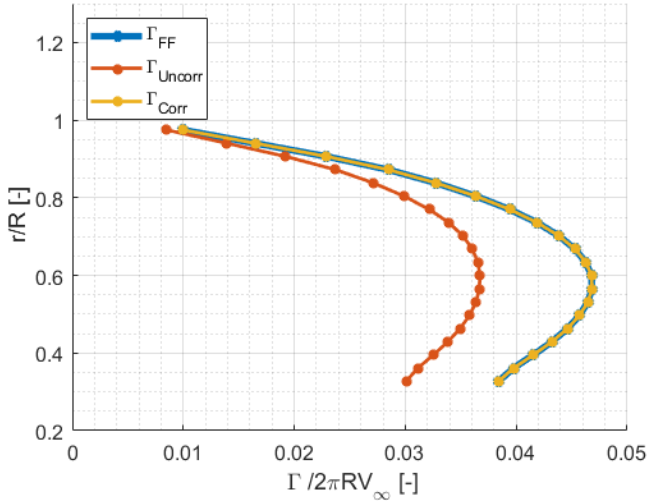

Figure 5.7: Circulation including adjusted inflow velocity

The influence of the velocity profile adjustment on the thrust performance is presented in table 5.1. The computed thrust is presented for three cases. The first is the LLT prediction from Li [3]. The Correction is the thrust computed including the correction angle for each section. The adjusted cases use a smooth inflow velocity distribution by a 5^{th} order polynomial. The table shows the same results as the circulation distribution in figure 5.7. The adjustment does not influence the thrust, even though the lift coefficient at the tip is much lower in the adjusted case compared to the Correction case. This means that the impact of the tip sections is too low to have any noticeable impact on the thrust of the SRV blade. The impact of the correction on the thrust is required to show at which vane sections the pitch angle needs to be corrected and where a compromise can be made in the final design. The next section will discuss this influence using again the adjusted velocity profiles to quantify the impact of the correction on the thrust for the tip and other vane sections.

Table 5.1: Comparison between original thrust prediction, applying the correction and adjusting the correction with a smooth lift distribution.

	$C_{T,V}$ [−]	T_V / T_P [-]
Original	0.0109	3.4%
Correction	0.0109	3.4%
Adjusted	0.0109	3.4%

5.2. SECTIONAL IMPACT

As shown in the previous section, the adjusted velocity profile for the blade sections close to the tip does not have a large impact on the total thrust of the vane. It is likely, that the blade sections of the SRV around the maximum circulation will have the largest impact on the thrust production of the vane. To quantify the amount of impact, the thrust of the SRV was computed with only one blade section rotated by its corresponding correction angle, the other blade sections kept their far-field angle of attack. This was done for all 20 blade sections separately.

This approach is to give an approximation of the sectional influence of the correction. In reality, the loading of each separate blade section affects the entire blade loading, which is also demonstrated by van Arnhem [51]. He showed how a local symmetric bell-shaped disturbance in the angle of attack along a semi-span influences the lift distribution of the semi-span. The change in circulation distribution as shown in figure 5.8a compared to the uncorrected circulation results in a vorticity that induces an upwash and downwash to the adjacent sections. Van Arnhem used the classical lifting line to compute the lift and drag and compared a case where the redistribution was taken into account and a case where the wing was analysed at each section including the disturbance. Even for a bell-shaped disturbance with a large spanwise gradient (approaching the disturbance as a step, the relative error of the lift coefficient between the redistribution and sectional case remained small. The induced drag increases with a large spanwise gradient, but since the thrust and torque forces are mainly depending on the lift force compared to the induced drag. Therefore it was concluded that the effect of the local disturbance on the neighbouring section would remain small.

To demonstrate the effect of the sectional impact due to the correction angle each section was rotated with the corresponding correction angle while the other pitch angles remained at their original value. In figure 5.8a the circulation distribution is shown where one section is rotated with the correction angle and at this radial position the circulation is again at the predicted far-field value. The thrust output of the disturbed circulation distribution was presented as the ratio between the corrected thrust and the uncorrected thrust. Note, the uncorrected thrust was based on the lower circulation due to the axial distance boundary and if the correction angle of a certain blade section does not have any influence on the thrust, the ratio of corrected thrust to uncorrected thrust would be 1.

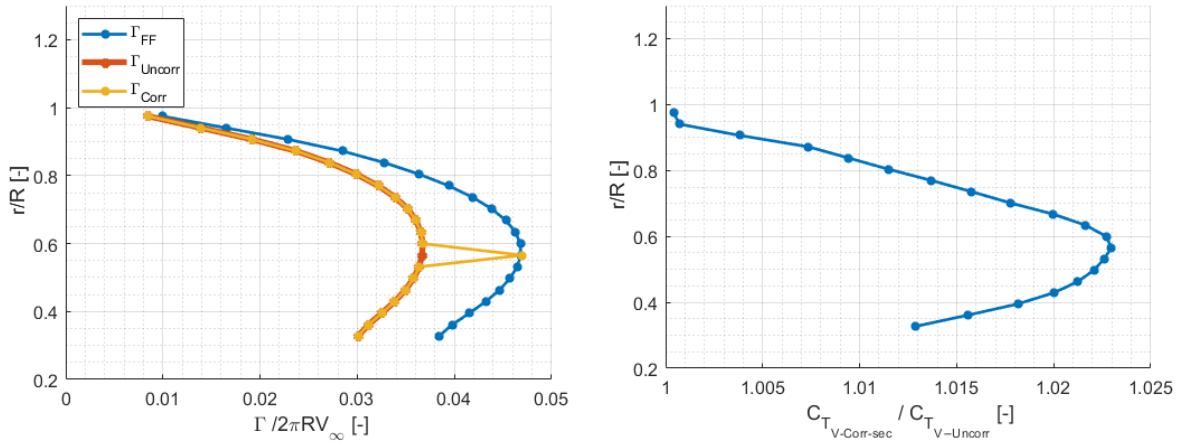

(a) Circulation distribution with a sectional correction

(b) Impact correction for each blade section

Figure 5.8: The impact of the correction angle for each blade section

The results of the impact are shown in figure 5.8b. It can be immediately noticed that the three blade sections at the tip have an impact on the thrust of less than 0.05%. This explains also the results from the previous section, where no difference in the thrust and circulation was noticed when the lift distribution at the tip was changed.

As expected, the impact of the angle correction is largest at the location of the maximum circulation. At this location, it is most favourable to have the optimum circulation, since the difference at this blade section, between the uncorrected circulation and the corrected circulation, is the largest. This result of the impact of

the correction angle on the thrust can be used when the SRV blade is turned by a fixed correction angle for all blade sections as will be explained in the next section.

5.3. FIXED CORRECTION

To avoid complicated blade designs, or to allow the blade to be corrected for different design points, a predetermined correction angle for all sections could be applied. This section will explain the effect of turning the full SRV blade with one fixed angle. There will be two cases presented, the first one is a fixed correction angle based on the average of all blade section correction angles. The second case is using a weighted average based on the impact of the correction angle as discussed in the previous section.

In the first case, the average is taken from the correction angle of all the blade sections. This results in an average correction angle of $\alpha_{corr} = 2.352°$. In figure 5.9a the angle of attack is shown with the fixed correction angle. The pitch distribution and circulation can be found in figure 5.9b and figure 5.10 respectively. The circulation distribution approaches the original distribution quite well. At the blade sections near the tip, the circulation is around 5% to 9% higher for the fixed correction angle compared to the original distribution. From the point of maximum circulation to the root, the circulation is 2% to 3% lower. Recalling the result from the previous section, the correction angle has the largest impact on the circulation and the thrust around the location of maximum circulation, therefore the lower circulation due to the average correction angle will decrease the thrust as is also shown in table 5.2. However, since the difference in total circulation is still small, less than 0.05%, also the total thrust of the vane is decreased by only a fraction, around 1%, compared to the originally predicted thrust.

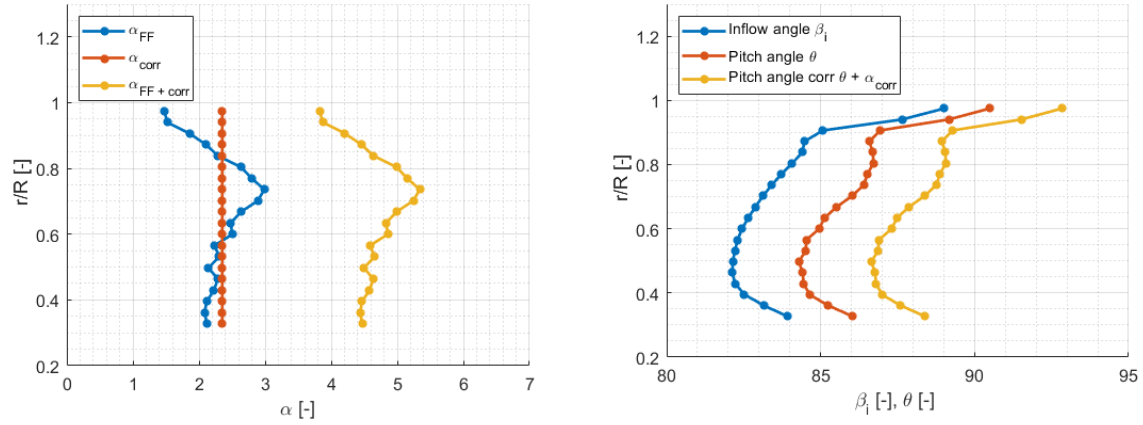

(a) Angle of attack distribution

(b) Pitch angle distribution

Figure 5.9: Fixed correction of $\alpha_{corr} = 2.352$ across the blade

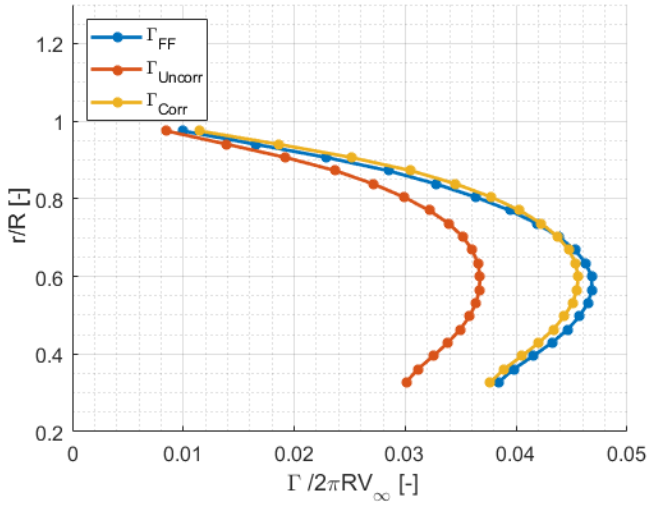

Figure 5.10: Circulation with a fixed average correction of $\alpha_{corr} = 2.352$ across the blade

In the second case, a weighted average correction angle is used. The weighting factor is based on the impact the sectional angle correction has on the thrust of the vane as discussed in section 5.2. The percentage of thrust produced by each blade section is used to determine the weight factor. When the percentage of thrust is higher, like at the location of the maximum circulation, the weight factor will also be larger. Multiplying the weight factor with the angle of attack correction and then dividing it by the sum of the weight factors, the weighted average can be computed and gives $\alpha_{corr} = 2.499°$. This correction angle is used in the computation of the circulation and the thrust, as is shown in figure 5.11 and table 5.2. Even though the same trend is noticed as for the normal average correction angle. There is an increase of circulation around the tip and a reduction around the location of maximum circulation, but the total circulation of the weighted average correction angle is higher. This is also shown in the total vane thrust. However, the improvement is only 0.05% of the total propeller thrust in favour of using the weighted average correction angle of attack over the normal average.

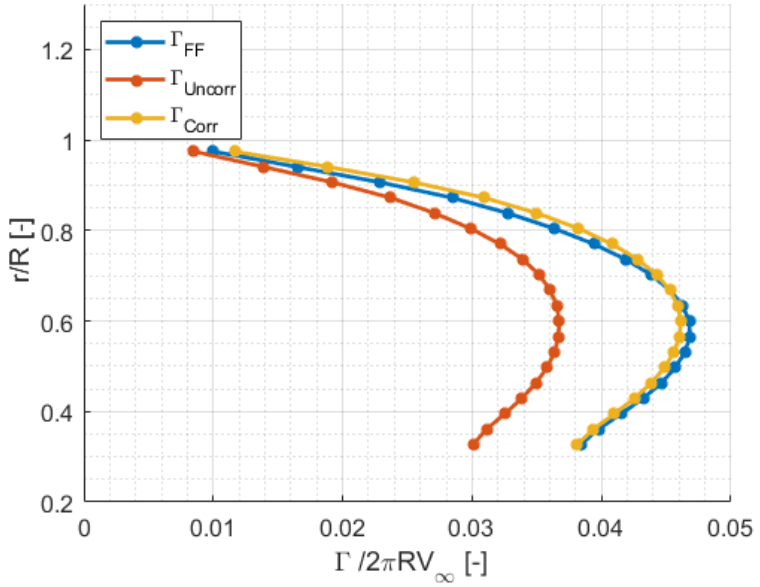

Figure 5.11: Circulation with a fixed weighted average correction $\alpha_{corr} = 2.352$ across the blade

Both the average and weighted average correction angles show a good approximation of the original computed circulation distribution and vane thrust. This will make the design of the SRV simpler since the whole blade can be rotated with one fixed correction angle and still obtains the far field thrust prediction.

Table 5.2: Fixed angle of attack for J = 0.6 and $C_{T,P} = 0.322$

	$C_{T,V}$ [−]	T_V / T_P [-]
Original	0.0109	3.4%
Separate Corr	0.0109	3.4%
Average Corr	0.0108	3.3%
Weighted Corr	0.0109	3.4%

5.4. VARIATION IN ADVANCE RATIO

Until now, the correction has been applied for a high-thrust case (J = 0.6, $C_{T,P}$ = 0.322 and $\beta_{0.7R}$ = 30°). To identify the behaviour of the correction at lower propeller thrust settings, the advance ratio will be varied. Since there was no sufficient data available for the propeller used by Li at different advance ratios, the velocity profiles for the input will be taken from the APIAN propeller by Stokkermans [2]. The SRVs will be designed at five different thrust coefficients of the propeller with corresponding advance ratios and a propeller blade pitch angle of $\beta_{0.75R}$ = 40.4°, see table 5.3. As mentioned in section 2.5.2, Stokkermans used two design cases, at high thrust (J = 0.95) and cruise thrust (J = 1.6). Similar to Li's results, the LLT numerical model over-predicted the thrust compared to the CFD simulations. To make a fair comparison by using the correction angle, the same airfoil profiles of the SRV blade will be taken as designed by Stokkermans.

Table 5.3: Performance conditions of propeller for different thrust settings

$C_{T,P}$ [−]	J [-]
0.5473	0.95
0.5317	1.00
0.3969	1.3
0.2451	1.6
0.1330	1.8

When the advance ratio is increased it immediately shows the impact of the correction. At high advance ratios, the propeller thrust is low and thus also the thrust generated by the SRVs. A lower SRV thrust means that the circulation of the blade is lower, followed by a lower sectional lift coefficient. At a lower lift coefficient, the correction becomes less relevant, as is depicted in figure 5.12. In this figure, the lift polar is plotted for two advance ratios, J = 0.95 and J = 1.8. For the low advance ratio, the correction can be applied as demonstrated in the previous sections. However, at a high advance ratio, the difference between the corrected and original lift coefficients is negligible. Furthermore, the design lift coefficient is negative, meaning that the corrected lift is higher than the original lift. Due to the linearity of the correction angle, the lift slope is rotated around the zero lift angle of attack. For negative lift, the corrected lift curve is then predicting a less negative lift compared to the original calculation. Therefore, the results of the correction angle at an advance ratio of J = 1.8 are difficult to verify since the correction is based on positive lift.

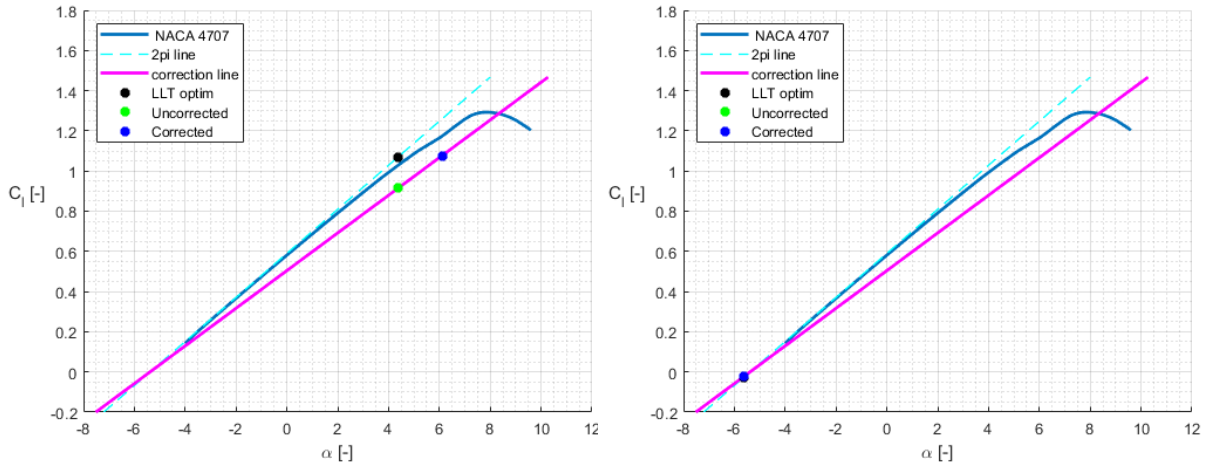

(a) Advance ratio J = 0.95

(b) Advance ratio J = 1.8

Figure 5.12: Lift polars at two different advance ratios of SRV blade section at the root for the APIAN propeller

5.4.1. APIAN SRV THRUST COMPARISON

For the APIAN propeller, Stokkermans choose two design points, a high thrust at J = 0.95 and a low thrust for cruise at J = 1.6. At these two design points, he predicted the thrust of the SRV with a numerical LLT approach and CFD simulations. Using Li's design method, a different circulation and pitch angle distribution was designed for the SRV compared to the design of Stokkermans. Additionally, also for the other thrust settings, an SRV was designed. To analyse the influence of the correction method, the planform and airfoils were taken from Stokkermans to make a direct comparison in SRV thrust. For the design of the SRV at $C_{T,P}$ = 0.547 $and C_{T,P}$ = 0.532, the planform and profile were taken from Stokkermans for the high thrust case. For the other thrust settings, the planform and profile were taken that Stokkermans designed for the low thrust case.

In figure 5.13 the thrust of the vane is plotted against the propeller thrust. In black, the far field prediction is shown using Li's design method and in red the uncorrected thrust is shown. Further, four points are plotted in the graph which represents the far field prediction and CFD prediction by Stokkermans in green and blue respectively. The corrected prediction is for all advance ratios lower. However, with an increasing advance ratio, the difference between the far field thrust and the corrected thrust of the vane becomes smaller, which is expected from the lift polars shown in figure 5.12. For a high advance ratio, there is hardly any difference between the far field and the corrected prediction of the lift. Therefore, the difference in thrust is also smaller.

At both a high and low propeller thrust, the far field prediction of the thrust agrees with the numerical results from Stokkermans. This shows that both his and Li's numerical method are consistent with each other. In the uncorrected thrust prediction it can be seen that for a high thrust, the prediction of the vane is much closer to the CFD simulations compared to the LLT prediction. It is not as close as the results of Li's SRV, but it approaches the thrust of the vane much better. At the low thrust, the correction method under-predicts the thrust compared to the CFD results. As said before, at high advance ratios the correction is (very) small, and since the thrust of the vane is close to zero, there could be some discrepancies in the thrust prediction.

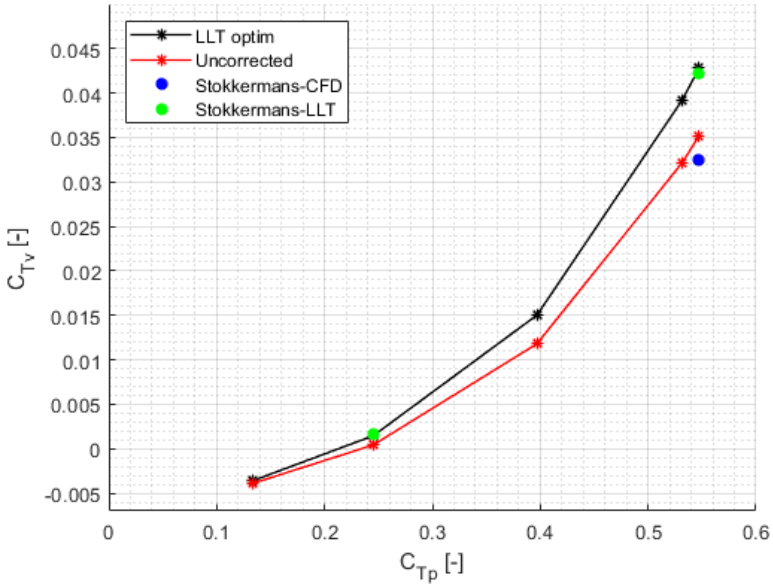

Figure 5.13: SRV thrust vs propeller thrust

5.4.2. APIAN SRV CORRECTION ANGLE DISTRIBUTION

The distribution of the correction angle, circulation and lift coefficient for different advance ratios is graphically displayed in figure 5.14 and figure 5.15. By lowering the advance ratio, the circulation will be lower, hence the lift coefficient and consequently also the correction angle. The correction angle increases by lowering the advance ratio. A black marker indicates the section of the maximum for each advance ratio corresponding with the data presented in table 5.4. For an advance ratio of J = 1.8, the maximum correction angle is not larger than α_{corr} = 0.5, but at a lower advance ratio (J = 0.95) the maximum correction angle is close to

$\alpha_{corr} = 2.3$. This large difference shows that the pitch angle of the SRV should be adjustable to maintain the optimal circulation distribution across the blade for different advance ratios.

At higher advance ratios the location of the maxima matches both the correction angle and the circulation. However, for lower advance ratios the location where the maximum is reached starts to deviate. Recalling the previous discussion in section 5.1, the ratio of the circulation to the velocity and chord determines where the maximum lift coefficient is located. In figure 5.16 is the velocity and chord distribution shown. The chord distribution is for all advance ratios the same, thus it will not explain the difference in the location of maximum circulation compared to the correction angle. For high advance ratios, the distribution of the inflow velocity and the circulation is more uniform, resulting in a lift distribution with a similar trend. In the case of lower advance ratios, the maximum of the circulation and the maximum of the inflow velocity is at different radial coordinates. The ratio of Γ/V^* causes the location of the maximum lift coefficient to decrease and consequently the location of the maximum angle of attack. However, the differences between the locations of the maxima are small, even at low advance ratios. The impact of the correction will still be the highest at the location of maximum circulation.

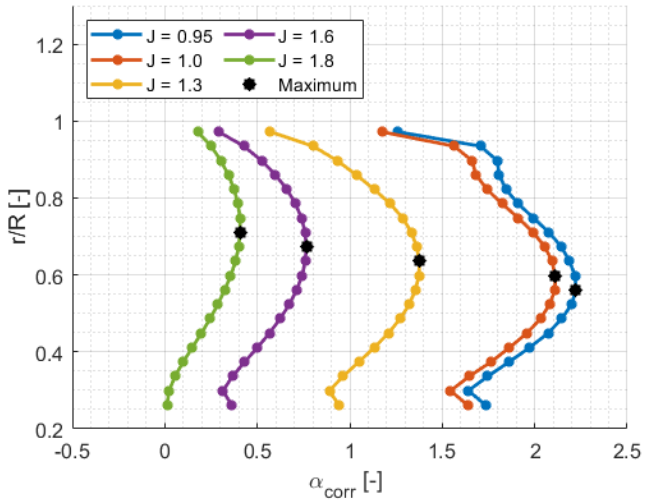

Figure 5.14: Correction angle of attack for different advance ratios

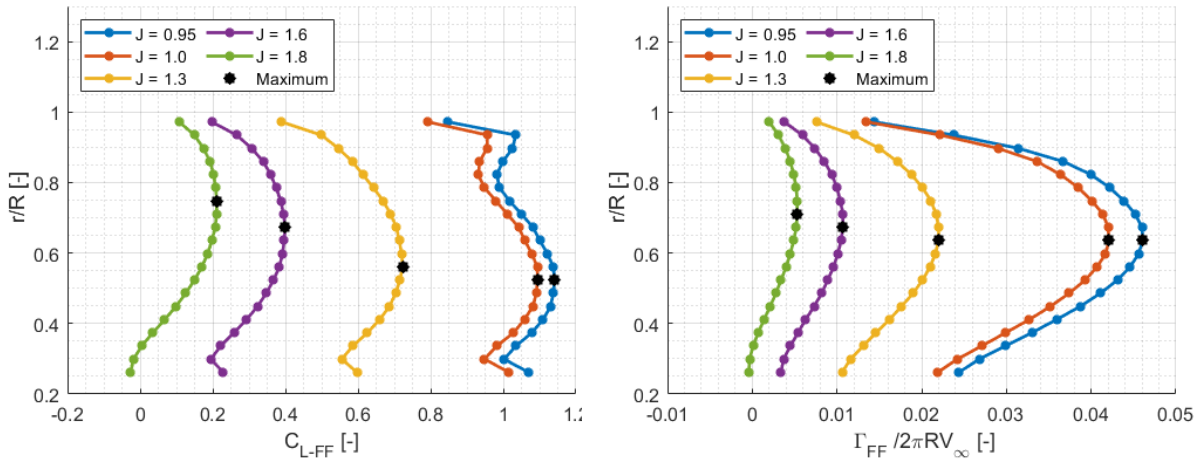

(a) Design lift coefficient

(b) Circulation distribution

Figure 5.15: Design lift coefficient and circulation distribution for different advance ratios

Table 5.4: Location of maximum circulation vs maximum correction angle of attack

	J = 0.95	J = 1.0	J = 1.3	J = 1.6	J = 1.8
r/R of Γ_{max}	0.6355	0.6355	0.6355	0.6729	0.7103
r/R of $\alpha_{corr,max}$	0.5608	0.5981	0.6355	0.6729	0.7103

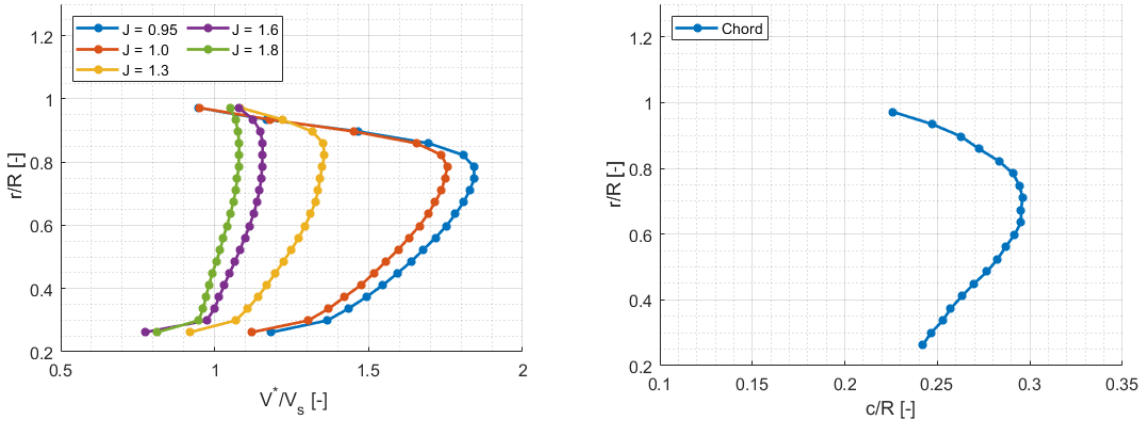

(a) Inflow velocity distribution

(b) Chord distribution

Figure 5.16: Inflow velocity distribution and chord distribution for different advance ratios

5.4.3. APIAN SRV FIXED CORRECTION ANGLE

In section 5.3, the influence of a fixed correction angle on the thrust of the SRV was discussed. This section will discuss the effect of the advance ratio for a fixed correction angle using both the average correction angle and the weighted average correction angle. The averages are taken from the correction angle as can be seen in figure 5.14. In table 5.5, the results are presented. The abbreviations mentioned in the table are Sep, Avrg and W Avrg for respectively separate correction angle, average correction angle and weighted correction angle. Similar to the conclusion from section 5.3, the fixed correction angle predicts a similar vane thrust as by using the sectional correction angle. The weighted average shows a better approximation compared to the normal average, but the differences are small for all advance ratios, especially when the vane thrust is compared to the total propeller thrust.

The correction angle distribution at different advance ratios, in figure 5.14 show that the correction angle needs to be able to vary between $\alpha_{corr} = 0$ and $\alpha_{corr} = 2.3$. By using a fixed (weighted) average correction angle the range of the required angle is reduced to $\alpha_{corr} = 0.3$ and $\alpha_{corr} = 2.0$, which is still a large difference.

The results of table 5.5 show that for all advance ratios, the far field thrust prediction was obtained when the average correction angle was used. Varying the advance ratio showed little effect on the difference in thrust predictions because the differences remained small. At higher advance ratios the thrust is reduced and consequently also the correction angle. Since the correction method is linear, it will always scale accordingly with the lift, as long as the design point is in the linear regime of the lift polar. Varying the advance ratio while keeping the correction angle fixed showed a large range of correction angles. This makes it desirable to have a variable pitch blade of the SRV.

Table 5.5: Results of turning the SRV blade by a separate of fixed correction angle for different advance ratios

Advance ratio	Correction	α_{corr}	$C_{T,V}$	T_V / T_P
J = 0.95	Sep	-	0.0414	7.56%
	Avrg	1.93	0.0412	7.53%
	W Avrg	2.01	0.0414	7.56%
J = 1.0	Sep	-	0.03813	7.17%
	Avrg	1.82	0.0379	7.13%
	W Avrg	1.91	0.03813	7.17%
J = 1.3	Sep	-	0.0145	3.66%
	Avrg	1.13	0.0143	3.62%
	W Avrg	1.22	0.0145	3.66%
J = 1.6	Sep	-	0.00107	0.44%
	Avrg	0.58	0.00097	0.39%
	W Avrg	0.66	0.00107	0.44%
J = 1.8	Sep	-	-0.0046	-3.47%
	Avrg	0.26	-0.0047	-3.52%
	W Avrg	0.34	-0.0045	-3.43%

5.5. AIRFOIL DESIGN

In section 4.2, an adjustment was presented in the airfoil optimization. For certain combinations of airfoil profile and Reynolds number, XFOIL has difficulty predicting the airfoil performance around the maximum lift coefficient. To make the optimizer more robust, the stall angle of attack was defined to be at the end of the linear regime of the lift polar instead of the angle of attack at the maximum lift coefficient. The parameterization of the airfoil optimization remained the same as Li proposed.

The adjusted optimization was validated with Li's airfoils in two ways. First using the airfoil parameterization of five variables (maximum camber, maximum camber position, thickness, maximum thickness position and chord length) as defined by Li [3] and will be referred to as optim-A. As will be shown, the new definition of stall angle in the airfoil optimizer resulted in optimized airfoil shapes that deviated from Li's airfoils. Therefore a second validation was done using four variables, by taking the chord distribution equal to Li's distribution. Since the chord length is a variable that influences the design lift coefficient and the profile drag, it was assumed that by excluding the chord length as a variable, the optimization would present a closer match to Li's results. The optimization with four variables will be called optim-B. The spanwise distributions of each variable are shown in figure 5.17a, figure 5.17b figure 5.18a, figure 5.18b and figure 5.19, for the maximum camber, the maximum camber position, the maximum thickness, the maximum thickness position and chord length respectively. The optimization was performed at four sections across the blade which will be called section 1, 2, 3 and 4 for respectively the root section, the section of maximum circulation, the intermediate section between the maximum circulation and the tip, and finally the tip section.

The updated airfoil optimizer shows a different distribution for all the parameters except the chord, which will be discussed later. The maximum camber stays constant for optim-B between sections 1 to 3 but is significantly higher, 14% to 30%, compared to Li's results. At section 4, the maximum camber is closely matched again with Li's results. Also, Optim-A shows a similar trend, except the maximum camber at section 1 increases by only 10% compared to Li's camber profile.

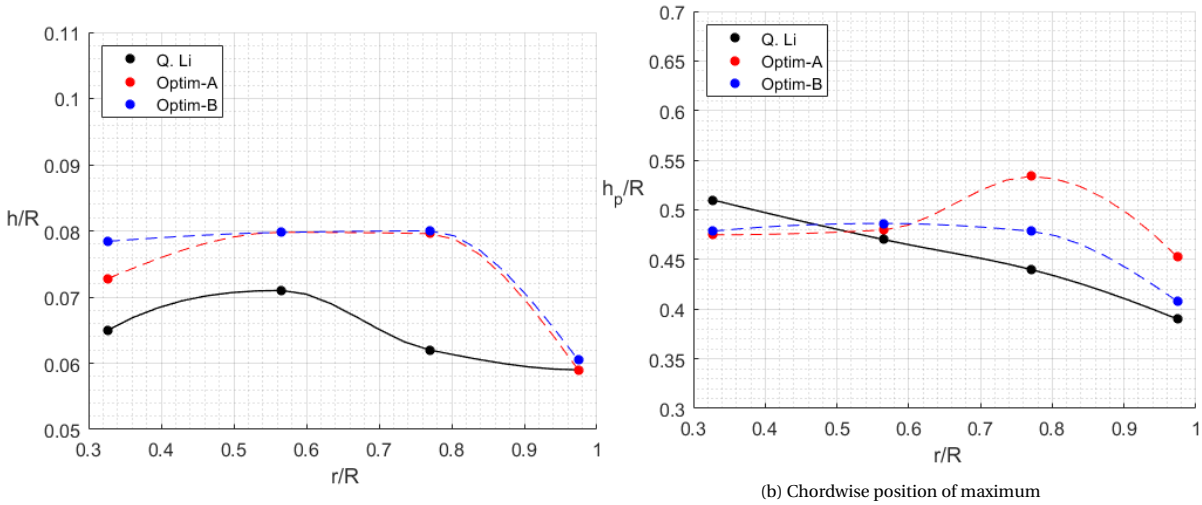

(a) Maximum camber

(b) Chordwise position of maximum camber

Figure 5.17: Airfoil design camber

The maximum camber position is shifted aft for the majority of the SRV blade for the two new optimizations, around 3% to 4%. Only Optim-A has a large rearward shift at section 3 of 20%. However, at the root section, the position of the maximum camber is more forward (6%) compared to Li.

The trends of the maximum thickness across the SRV blade can be described similarly to the trend of the position of maximum camber with again a peak at section 3, meaning a large increase in maximum thickness at this blade section. At the root section, the thickness is slightly lower compared to Li's thickness, but between the root and the tip, the thickness increases to a maximum of 30% for Optim-B at section 3 and for Optim-A an increase of 80% in maximum thickness for this section is shown.

For the position of maximum thickness, Optim-A starts with a similar position as Li, but between sections 1 and 4, the position moves aft with a maximum of 32% at section 3 compared to Li. Optim-B has across the whole blade length a rearward shifted the position of the maximum thickness, with a variation between 15% and 30% for the different blade sections.

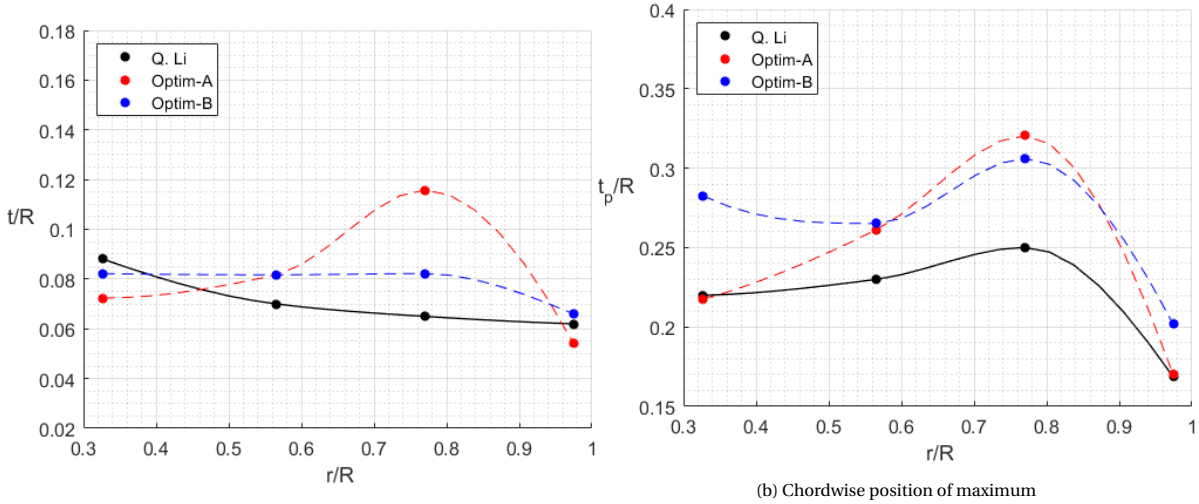

(a) Maximum thickness

(b) Chordwise position of maximum thickness

Figure 5.18: Airfoil design thickness

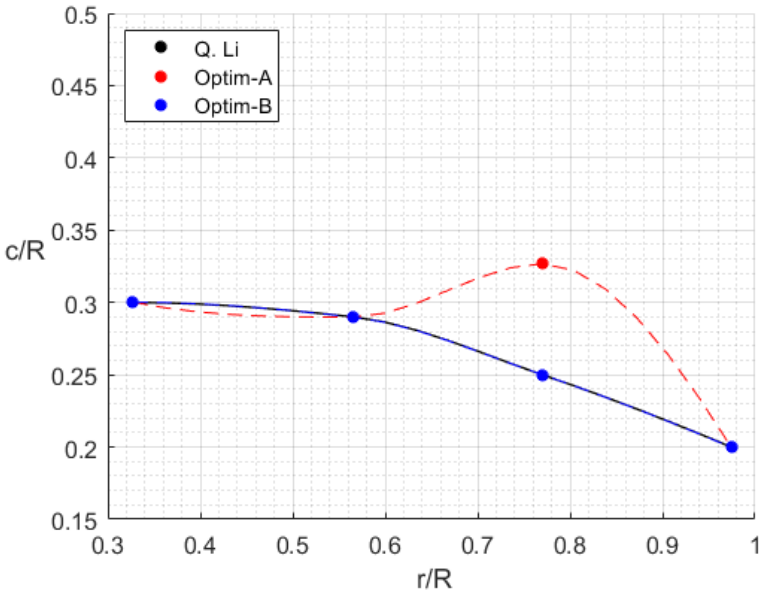

Figure 5.19: Airfoil design chord distribution

Finally, for the chord length, only optim-A is relevant, since in optim-B the chord length is kept equal to Li's chord distribution. Optim-A's chord distribution has the same values for sections 1, 2 and 4, but at section 3 the chord is much larger, almost 25% compared to Li's chord length. The other variables also showed a large increase in either maximum thickness and the position of maximum camber and thickness at section 3. It can be said that the validation did not work well, as for most of the airfoil parameters a different blade distribution was found. However, as will be shown later, the different airfoil profiles hardly influenced the thrust of the SRV, which would provide more freedom in choosing an airfoil for the SRV.

To show that the two optimizations, according to the objective function (equation (2.22)), perform better compared to Li's airfoil, table 5.6 and table 5.7 will be used. The objective function is divided into three parts f1, f2 and f3, for respectively the design drag coefficient, the stall drag coefficient and the difference between the stall angle of attack and the design angle of attack. In the table is F referring to the objective function.

The tables show that for each section the objective function, for both optimizations A and B, has a lower value compared to Li's airfoils. The airfoil profiles of Li were taken as a reference and therefore those airfoils have an output of the objective function equal to 1. Only at section 4 an improvement is found in drag, see the f1 and f2. For the other sections, both optim-A and optim-B result in an increase in drag coefficient at the design point and the stall point. The main improvement of the objective function is for the distance between the stall angle of attack and the design angle of attack. It is remarkable that in this part of the objective function, an improvement is found since figure 4.5 shows that the new definition of the stall angle results in a lower stall angle of attack, hence a smaller difference between the design and stall point. Since the improvement in the angle of attack difference is large compared to the increase in drag coefficient the objective function reaches a lower minimum compared to Li's airfoils.

Table 5.6: Objective function comparison between the airfoil profiles of Li, Optim-A and Optim-B for section 1 and 2

	Section 1			Section 2		
Airfoil	Li	optim-A	optim-B	Li	optim-A	optim-B
NACA	7509	7507	8508	7507	8508	8508
f1 (Cd_{design})	1	0.98	1.03	1	1.05	1.05
f2 (Cd_{stall})	0.5	0.52	0.56	0.5	0.56	0.56
f3 ($\alpha_{stall} - \alpha_{design}$)	0.5	0.59	0.69	0.5	0.73	0.73
F	1	0.91	0.89	1	0.88	0.88

Table 5.7: Objective function comparison between the airfoil profiles of Li, Optim-A and Optim-B for section 3 and 4

	Section 3			Section 4		
Airfoil	Li	optim-A	optim-B	Li	optim-A	optim-B
NACA	6407	8512	8508	6406	6505	6407
f1 (Cd_{design})	1	1.44	1.08	1	0.91	0.83
f2 (Cd_{stall})	0.5	0.88	0.62	0.5	0.41	0.35
f3 ($\alpha_{stall} - \alpha_{design}$)	0.5	2.31	1.49	0.5	0.47	0.3
F	1	0.02	0.21	1	0.86	0.88

A representation of the sectional drag coefficient at the design point for the different airfoil optimizations can be seen in figure 5.20. Since the part of the objective function responsible for the sectional drag at the design point (f1) was higher, the sectional drag coefficient distribution of Li's airfoils is for a major part lower compared to the new optimal airfoil design. At the point of maximum circulation, section 2, the sectional drag coefficient is 6% higher for the newly designed airfoils compared to Li's ones. Recalling the equation to compute the thrust of the SRV equation (2.19), the streamwise component of the sectional drag needs to be subtracted from the streamwise component of the produced lift, thus a higher sectional drag coefficient would result in a lower SRV thrust.

The predicted thrust of the different optimized airfoils is presented in table 5.8. Here, three thrust values are presented for each airfoil profile. $C_{T,V-Uncorr}$ is the thrust computed in the uncorrected case and $C_{T,V-Corr}$ is the thrust including the correction to obtain the same lift as in the far field case. The small increase in drag coefficient is reflected in the thrust prediction. The two optimized airfoil profiles with Li's profiles show a difference of 1% for the thrust including the correction. However, in reference to the propeller thrust, the difference is 0.01%. This shows that the increase in drag, due to a different airfoil, is sufficiently small to hardly influence the thrust of the SRV. It does not mean that the airfoil optimizer is a negligible step in the design procedure of SRVs. Only there is more design freedom in choosing an airfoil profile for the SRV without losing thrust of the SRV. The amount of design freedom for the airfoil profile will be discussed in the next section.

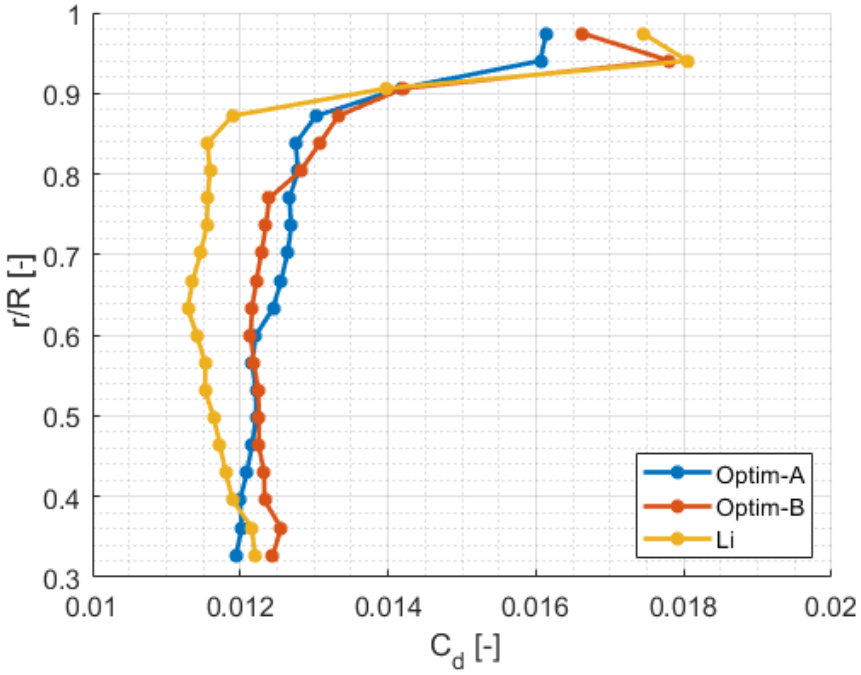

Figure 5.20: Sectional drag coefficient of Li, Optim-A and Optim-B

Table 5.8: Thrust of SRV for Li, Optim-A and Optim-B

	$C_{T,V-Uncorr}$ [−]	$T_{V-Uncorr}/T_P$ [-]	$C_{T,V-Corr}$ [−]	T_{V-Corr}/T_P [-]
Li	0.0084	2.60%	0.0109	3.4%
Optim-A	0.0082	2.55%	0.0109	3.39%
Optim-B	0.0083	2.58%	0.0109	3.39%

5.5.1. AIRFOIL VARIATION

The previous section showed little influence on the SRV thrust for two optimized airfoil profiles compared to Li's airfoils. To take it a step further, this section will discuss the amount of design freedom for the airfoil profiles before the thrust of the SRV will be influenced.

There is a profile variation chosen with high and low camber and high and medium thickness. The profiles with a low thickness or camber lower than 6% could not converge in XFOIL for design Reynolds number to obtain a lift polar and are therefore not included in the comparison. For these results, the sectional correction angle was used and the chord distribution was kept the same as Li. In table 5.9 the results of the SRV thrust are compared with each other. The delta, see equation (5.1), is the difference in SRV thrust between the vane with a constant NACA airfoil profile and Li's airfoil profiles normalized with the propeller thrust.

$$\Delta = \frac{(T_V)_{NACA} - (T_V)_{Li}}{T_P} \tag{5.1}$$

The table shows that mainly low camber, high thickness and an aft location of the maximum camber need to be avoided. This is in line with the airfoil design routine from Li. The table also shows that the variation in camber between 4% and 8% is still able to produce similar thrust values as Li's design. Further, the variation in thickness for a cambered airfoil of 4% and 6% does not influence the thrust either. And looking at the variation in camber position, as long as the position is smaller than 60% of the chord length, the thrust will not change much. However, a symmetrical airfoil should also be avoided, as is shown in table 5.10. The other airfoil profiles follow the same trend as described above. The lower SRV thrust of the airfoils with high thickness can be explained by a larger sectional drag coefficient, see figure 5.21. At some sections of the cambered high-

thickness airfoil, the drag is doubled compared to Li's results. The NACA 0015, shows a massive increase in drag coefficient up to three times as much as Li.

Table 5.9: Difference in SRV thrust for varying airfoil profiles

NACA	Δ	NACA	Δ	NACA	Δ	NACA	Δ	NACA	Δ
2607	-0.61	4607	-0.10	6607	0.00	8607	-	6407	0.00
2609	-0.29	4609	0.00	6609	-0.01	8609	-0.06	6507	0.00
2612	-0.18	4612	-0.01	6612	-0.04	8612	-0.10	6807	-0.20
2615	-0.22	4615	-0.04	6615	-0.07	8615	-0.22	6907	-0.36

Table 5.10: Difference in SRV thrust for a selection airfoil profiles

NACA	Δ
Li	0.00
0015	-0.49
2615	-0.22
4408	-0.06
8615	-0.22

This comparison shows clearly the necessity of using a cambered airfoil with moderate thickness. However, the loss in thrust is not large when the maximum thickness of the airfoil profile is increased, providing some more freedom in choosing a suitable airfoil profile for the SRV.

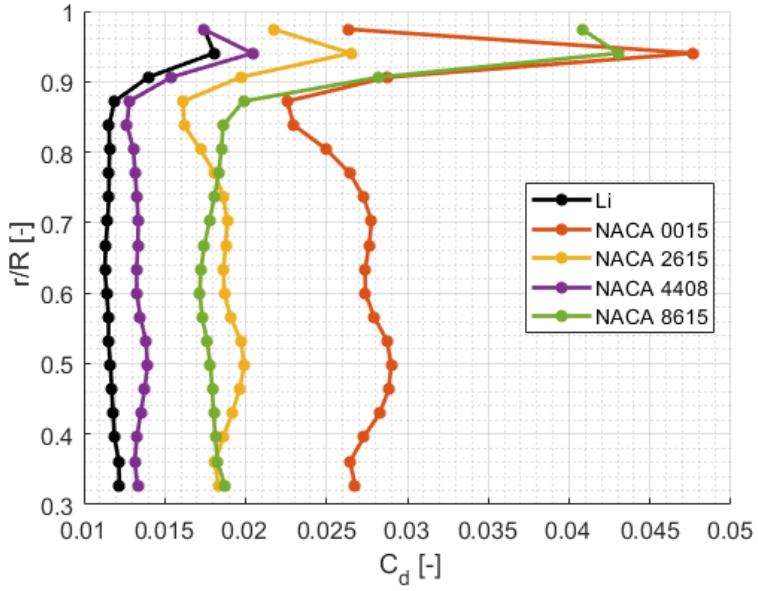

Figure 5.21: Sectional drag coefficient of different airfoils

5.5.2. CHORD VARIATION

Finally, in this section, the chord distribution is varied for each of the three optimizations, Li, optim-A and optim-B. Three variations for the chord distribution were chosen, a fixed chord, a chord distribution with a taper ratio of 1.5 and an elliptical chord distribution, as can be seen in figure 5.22. For reference, the chord distribution of Li was included. The tip chord of the elliptical chord distribution is 50% of the root. A smaller tip chord would result in a too-high lift coefficient, equation (2.23), that would pass the maximum lift coefficient of the airfoil profile, hence the linear regime of the lift polar, making the prediction unfeasible. The design lift coefficient of the other chord distributions remains in the linear regime of the lift polar, meaning that the application of the correction angle is also still valid.

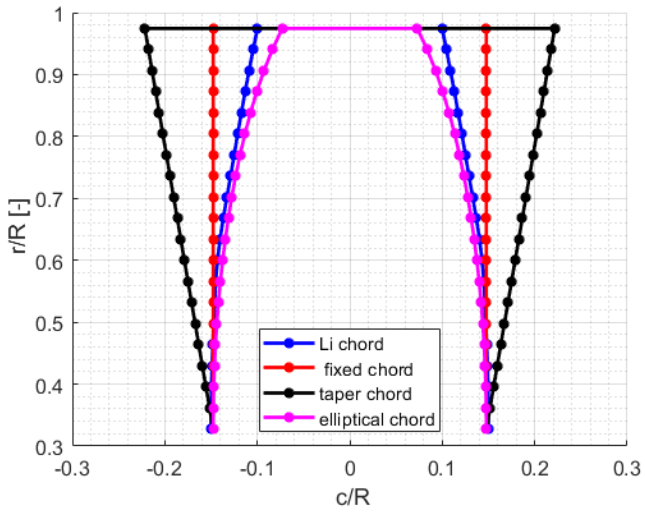

Figure 5.22: Different chord distributions for the SRV

The sectional drag coefficient for the different chord distributions is plotted in figure 5.23, figure 5.24 and figure 5.25 for the optimized airfoil of respectively Li, optim-A and optim-B. Around the root, the sectional drag coefficient is the same for all chord distributions. This is also understandable since the chord lengths at the root are kept the same. Towards the tip of the SRV, the real difference in chord length is noticeable. It can be seen, that the elliptical chord distribution has the highest sectional drag. Maintaining a fixed chord length across the SRV blade is for the two newly optimized airfoils not influencing the sectional drag coefficient. Only for Li's optimized airfoil, a fixed chord distribution will lower the sectional drag around the tip of the SRV blade. In the case of the tapered chord distribution, the sectional drag coefficient is considerably lower approaching the tip. Since the chord length is increased at the tip, a lower lift coefficient is computed to maintain the design circulation equation (2.23). Contrary, the chord length of the elliptical distribution is reduced at the tip, which increases the lift coefficient. As well known, the drag of an airfoil is proportional to the lift coefficient squared, see textbooks like Anderson [9]. The minimum drag coefficient is for cambered airfoils at a positive lift coefficient. With a decreasing lift coefficient at the tip due to a smaller chord length, the quadratic relation of the lift and drag will increase the drag coefficient for small lift values. The radial blade coordinates of $r/R = 0.9$ to the tip demonstrate this.

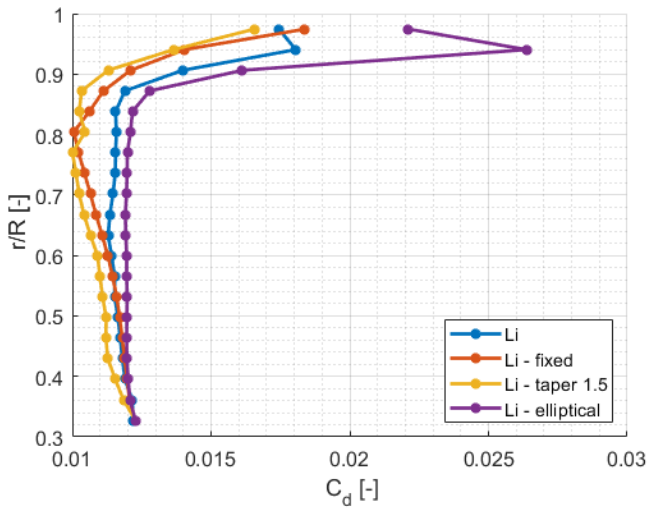

Figure 5.23: Sectional drag coefficient of Li airfoils with different chord distribution

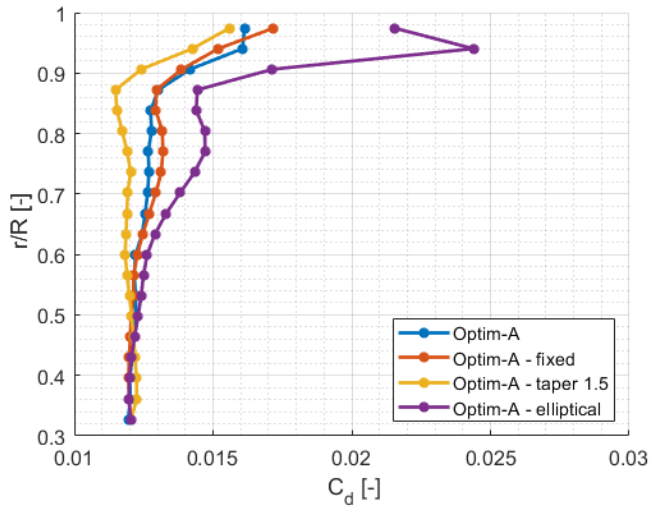

Figure 5.24: Sectional drag coefficient of Optim-A airfoils with different chord distribution

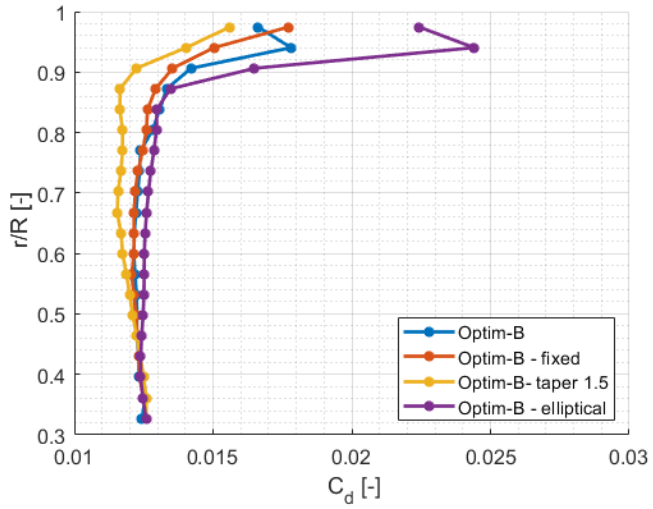

Figure 5.25: Sectional drag coefficient of Optim-B airfoils with different chord distribution

The difference in thrust for the different chord distributions at the three airfoil designs is presented in table 5.11 using the same definition for the delta as before, equation (5.1). Subsequently, in the previous discussion about the sectional drag coefficient, the same trend can be seen for the SRV thrust. The highest sectional drag was found for the elliptical chord distribution, hence the lowest thrust. The tapered chord distribution produced the lowest sectional drag coefficient and has therefore also the highest SRV thrust. However, the differences in SRV thrust are small, in reference to the propeller thrust it is a few tenths of a per cent, which is a negligible difference.

In the above analysis it has been shown that the profile drag of the vane for different airfoil designs remained sufficiently low to not negatively influence the SRV thrust, which means that concerning the drag of the SRV, the main contribution will be attributed to the induced drag.

5.6. CONCLUSION

The results show that when the correction angle is added to the blade pitch, the thrust of the SRV complies again with the far-field prediction. However, high-fidelity experiments should also validate this statement. The maximum correction was required around the location of maximum circulation. A sudden increase in

Table 5.11: Thrust of SRV for variation in chord

Chord distribution	Δ
Li - fixed	-0.01
Li - taper 1.5	-0.02
Li - elliptical	-0.04
Optim-A - fixed	-0.03
Optim-A - taper 1.5	-0.01
Optim-A - elliptical	-0.05
Optim-B - fixed	-0.02
Optim-B - taper 1.5	-0.01
Optim-B - elliptical	-0.04

the angle of attack at the tip was due to a local minimum of inflow velocity just before the tip. The peak in the angle of attack at the tip was removed by using a polynomial fit of the 5^{th} order for the inflow velocity, which resulted in a smooth lift distribution. The thrust was hardly influenced by this adjustment since the impact on the SRV thrust of the correction at these sections around the tip is small. The highest impact was obtained at the location of maximum circulation. To simplify the application of the correction angle to the SRV blade pitch a fixed correction angle was used. The average of all correction angles provided only a marginal drop in total SRV thrust. Using the effect of the impact of the correction angle on the thrust, a weighted average correction angle was computed and improved the thrust of the SRV by 0.05% in reference to the propeller thrust.

When the advance ratio was varied, the effects of the correction angle were similar as described in the previous paragraph. However, it was noted that due to the reduced propeller thrust, the thrust of the SRV would also reduce, hence the required lift coefficient would be smaller and consequently the correction angle. A difference of 1.7° in correction angle for a fixed correction showed the necessity of using an SRV with a variable pitch to increase or reduce the correction angle to obtain the optimal circulation distribution at different off-design conditions.

Finally, the validation of the adjustment to the airfoil design routine showed that there is more freedom in choosing an airfoil profile and chord distribution for the SRV blade. For the airfoil profiles a camber between 4% and 8% is possible, the maximum camber position should not be higher than 6%, but also not too low. However, due to the limitations of XFOIL, the lower limit could not be defined. Further, the thickness can vary between 7% and 15% depending on the amount of camber. The chord distribution can be either elliptical, straight or with a positive taper. The difference in thrust compared to Li's chord distribution was negligible. The main factor that drives this freedom is the sectional profile drag of the airfoil. As long as the design point of the lift coefficient remains in the linear regime of the lift polar, the profile drag will also not vary much and thus more freedom can be obtained in choosing an airfoil profile.

6

CONCLUSIONS AND RECOMMENDATION

This final chapter concludes the thesis, with the conclusion in section 6.1 and recommendations in section 6.2.

6.1. CONCLUSIONS

Swirl Recovery Vanes have proven their effectiveness by increasing the propulsive efficiency of the propeller by converting rotational momentum from the slipstream into axial momentum. Several studies have tried to quantify the thrust produced by the vanes using low-fidelity models. The predicted thrust of the SRVs was verified with high-fidelity models, such as CFD or wind tunnel experiments, however, the low-fidelity models showed an over-prediction of the SRV thrust.

Many low-fidelity models use the lifting line theory to compute the lift and thereby also the thrust produced by the SRV. The lifting line theory uses potential flow assumptions. Meaning it cannot model all flow conditions properly. Potential flow is based on the free flight condition, which entails a flow field that extends from $-\infty$ to $+\infty$. In the particular case of propeller slipstream interaction with lifting surfaces, this assumption does not hold anymore. The flow field is bounded by its height and axial distance. The height boundary is defined by the arc length between the blades of the SRV. The SRV geometry in this thesis showed to have a sufficiently large distance between the blades to have no effect on the airfoil. However, the axial distance was small enough to be relevant. The focus of this thesis was to present and implement a correction for the upstream boundary condition enforced by the propeller in the SRV design routine to reduce the over-prediction of the lifting line theory.

The correction is based on the application of the Kutta–Joukowski theorem in an axially confined domain in combination with the thin airfoil approximation. This correction can be applied to a situation of testing in an open-jet wind tunnel where the flow at the nozzle plane defines the flow upstream of a 2D airfoil blade, similar to the propeller-SRV combination. Data from an open-jet wind tunnel showed a large difference in lift polars of the potential flow solution and the experimental measurements. Since the slope of both polars was the same, in the linear regime of the lift polar only a simple rotation of the airfoil would be required to correct from the potential flow solution to the measurements.

The amount of rotation depends on the axial distance between the airfoil and the upstream boundary condition because, for a large distance, the free flight condition is met, which complies again with the potential flow assumption. Using the Biot-Savart law and the thin airfoil theory, an expression for the correction angle can be derived. The correction, or amount of rotation, is based on the ratio between the chord and axial distance between the boundary condition and the point of circulation and the free stream angle of attack. For airfoils, the point of circulation is at the quarter chord point. The thin airfoil theory assumes a lift curve slope of 2π with a zero lift angle of attack equal to zero. The theory is only valid for airfoils with a low thickness otherwise the difference in slope will cause wrong lift predictions. Further, SRV airfoils are usually cambered airfoils and to account for this, the zero lift angle of attack needs to be included in the correction angle. Validating the correction with the open-jet wind tunnel showed that the expression gives a fair prediction of the lift of an airfoil with a limited distance to the nozzle exit plane. According to the correction, the axial distance

becomes important when the d_{SRV}/c is smaller than 15. Very close to the boundary plane, the correction will not provide fair lift predictions anymore, since the amount of rotation increases rapidly.

The correction angle was included in the design routine for SRVs since the ratio of the axial distance between the propeller plane and the quarter chord over the chord is around 0.5. The correction angle is added to the design routine once the airfoil shape is known for each section is known. This means that each blade section will be separately corrected. In the wind tunnel experiments, the thrust of the SRVs was predicted to be 2.6% of the thrust of the propeller, while the lifting line predicted a thrust which was 3.4% of the thrust of the propeller. When the design angle of attack would stay constant, the corrected lift curve slope computed a vane thrust which would be 2.58% of the propeller's thrust. By adding the correction to the current design angle of attack for each blade section, the thrust from the lifting line prediction was obtained. Confirming that the correction captures the effect of the upstream boundary condition for SRVs. Even though the velocity profiles at the mid-chord location of the SRV were used, the corrected thrust was comparable to the original LLT prediction. This means that either the inflow velocity is converged before the SRV or the thrust prediction in a high-fidelity will still be lower compared to the corrected thrust.

Along the blade radius, the location of maximum correction was not exactly the same as the point of maximum circulation. This is caused by the definition of the lift coefficient, which includes also the magnitude of the free stream velocity and the chord length, but even though they are not exactly at the same location, they are close. Near the tip, the lift coefficient increases rapidly due to a large gradient of free stream velocity to the radial location of the blade. This also affects the design angle of attack and pitch distribution. To maintain a smooth lift distribution, the velocity distribution can be adjusted using a 5^{th}-order polynomial. With a smooth velocity distribution also the lift distribution will change into a more desired elliptical distribution. The impact of the lift coefficient on the total thrust is small, thus removing the peak at the tip does not have any influence on the thrust prediction.

It was found that the section with the biggest impact on the thrust of the vane was at the location of maximum circulation. This is a logical outcome since the maximum circulation contributes the most to the total thrust, and therefore this blade section has the biggest impact. Further, the correction along the blade was simplified by taking an average correction angle. This would make it much easier to apply the correction for different design conditions since the whole blade can be turned. Two cases were compared, a normal average correction angle and a weighted average correction angle. The weighted average correction angle includes the impact of each blade section on the thrust. The results showed that in both cases the lifting line prediction of the vane thrust would be obtained, but using the weighted average the computed vane thrust is higher, 3.40% to 3.38% of the propeller thrust. Therefore it would be desired to correct the SRV blade with one correction angle to make the blade suitable for more design conditions.

Further, the influence of the advance ratio on the correction angle was investigated. The location of the maximum correction angle matched well with the location of the maximum circulation, for higher advance ratios the locations are exactly the same compared to the lower advance ratios where a slight difference is spotted. As mentioned before this is caused by the different gradients of the free stream velocity, chord and circulation which influence the sectional lift coefficient.

A variable pitch angle of the SRV blade is useful for off-design conditions. The thrust of the vane did not change too much if a separate, average or weighted average correction angle was used. Of course, following the previous conclusion, the weighted average correction angle resulted in the highest vane thrust. However, for higher advance ratios the difference between the average and weighted average correction angle seems to play a more profound role, again in favour of the weighted average correction angle. To conclude, using a fixed correction angle shows good agreement, but the impact of each section needs to be taken into account to obtain the maximum vane thrust.

In the optimization of the airfoil profiles, it was found that there is more freedom in choosing a profile for the SRV without compromising on the thrust. Different airfoil profiles were compared to identify the influence on the thrust. For the airfoil profiles a camber between 4% and 8% is possible, the maximum camber position should not be higher than 6%, but also not too low. However, due to the limitations of XFOIL, the lower limit could not be defined. Further, the thickness can vary between 7% and 15% depending on the amount of camber. Airfoils within these limits would not cause an increase in drag coefficient to sufficiently decrease the thrust of the SRV. Also, the chord distribution could be changed into an elliptical, straight or with a positive taper without increasing the profile drag to lower the thrust. The analysis showed that the profile drag of

the SRV airfoils remained small while keeping within the limits of the airfoil parameters mentioned above. The induced drag has a more profound contribution to the total drag and therefore more focus should lie on minimizing the induced drag

6.2. RECOMMENDATIONS

This final section will present recommendations when this thesis is used for future work.

- To compute the optimal circulation distribution, the Newton solver requires an axial and tangential velocity profile as input. Due to the available data, the velocity profiles used in the solver were taken at the mid-chord location of the SRV. Even though the development of the slipstream was assumed to have a marginal difference, the correction method requires a velocity profile input at the location where the flow field is defined. However, the velocity profile at the propeller plane can only be used if the differences in velocity due to the development of the slipstream remain small. More research should focus on how much the slipstream between the propeller plane and SRV develops and what the best location of the velocity input for the SRV design is.

- The 2D upstream boundary correction angle was validated by data from an open-jet wind tunnel experiment where the axial distance, between the wind tunnel nozzle exit and the airfoil, was fixed. Since the purpose of the correction is to capture the effect of the axial distance, it is recommended to verify the correction for a variation of axial distances either by CFD or wind tunnel experiments.

- The implementation of the correction angle in the SRV design routine showed that the vane thrust of the lifting line theory could be obtained and would not over-predict the thrust any more. However, the thrust of the new blade pitch angle should be validated with high-fidelity models, to see if the full over-prediction is captured by the correction angle or if other effects still influence the over-prediction.

- The correction is based on a 2D airfoil profile. However, the SRV is a 3D blade. This thesis uses the Blade element theory to add all 2D airfoil profiles together to obtain a 3D SRV blade. However, in 3D other factors come into play, such as a radial flow across the blade and tip corrections need to be applied. Therefore, a more thorough investigation is necessary to validate if the 2D correction still holds when shifted to a 3D blade.

BIBLIOGRAPHY

[1] R. Singh, G. Ameyugo, and F. Noppel, *Jet engine design drivers: past, present and future,* in *Innovation in Aeronautics* (Elsevier, 2012) pp. 56–82.

[2] T. Stokkermans, *Design and Analysis of Swirl Recovery Vanes for an Isolated and a Wing Mounted Tractor Propeller*, Master's thesis, Delft University of Technology (2015).

[3] Q. Li, *Towards optimum swirl recovery for propeller propulsion systems*, Ph.D. thesis, Delft University of Technology (2019).

[4] L. L. M. Veldhuis, *Propeller wing aerodynamic interference*, Ph.D. thesis, Delft University of Technology (2005).

[5] Y. Yang, D. Ragni, L. Veldhuis, and G. Eitelberg, *Propeller induced ground vortex,* ICAS, Brisbane (2012).

[6] B. P. Epps and R. W. Kimball, *Unified rotor lifting line theory,* Journal of Ship Research **57**, 181 (2013).

[7] B. Ewald, *Wind Tunnel Wall Corrections* (AGARDograph 336, 1998).

[8] F. Weinig, *Theory of two-dimensional flow through cascades(inviscid incompressible two-dimensional cascade flow considering compressibility, viscosity and high solidarity effects),* in *Aerodynamics of Turbines and Compressors*, Vol. 1 (Princeton University Press, 1964).

[9] J. Anderson, *Fundamentals of Aerodynamics*, 6th ed. (MCGraw Hill, 2016).

[10] V. Ciobaca, M. Pott-Pollenske, S. Melber-Wilkending, and G. Wichmann, *Computational and experimental results in the open test section of the aeroacoustic windtunnel braunschweig,* International Journal of Engineering Systems Modelling and Simulation 47 **5**, 125 (2013).

[11] D. C. Mikkelson, G. A. Mitchell, and L. J. Bober, *Summary of recent nasa propeller research,* NASA (1985).

[12] A. Stuermer, *Unsteady cfd simulations of contra-rotating propeller propulsion systems,* in *44th AIAA/ASME/SAE/ASEE Joint Propulsion Conference & Exhibit* (2008) p. 5218.

[13] R. D. Hager and D. Vrabel, *Advanced turboprop project*, Vol. 495 (NASA, 1988).

[14] J. Godston and F. Mike, *Evaluation of single and counter rotation gearboxes for propulsion systems,* AIAA/SAE/ASME 20th Joint Propulsion Conference , 1195 (1984).

[15] A. Stürmer, C. O. M. Gutierrez, E. W. Roosenboom, A. Schröder, R. Geisler, D. Pallek, J. Agocs, and K.-P. Neitzke, *Experimental and numerical investigation of a contra rotating open-rotor flowfield,* Journal of Aircraft **49**, 1868 (2012).

[16] Aviationweek, *Cfm unveils 'open fan' demonstrator plan for next-gen engine,* https://aviationweek.com/aerospace/cfm-unveils-open-fan-demonstrator-plan-next-gen-engine (2021), accessed: 2022-12-02.

[17] X. Liu, *Design of Swirl Recovery Vanes for Wing-Mounted Tractor Propeller Propulsion System*, Master's thesis, Delft University of Technology (2018).

[18] J. Van Kuijk, *Analysis of Swirl Recovery Vanes: Propulsion system performance and slipstream-wing interaction*, Master's thesis, Delft University of Technology (2015).

[19] R. Nederlof, *Improved modeling of propeller-wing interactions with a lifting-line approach: Investigation of a suitable correction method to account for the finite slipstream height*, Master's thesis, Delft University of Technology (2020).

[20] J. Vanderover and K. Visser, *Analysis of a contra-rotating propeller driven transport aircraft,* AIAA Student Paper Competition (2006).

[21] V. P. Blandeau and P. F. Joseph, *Broadband noise due to rotor-wake/rotor interaction in contra-rotating open rotors,* AIAA journal **48**, 2674 (2010).

[22] J. H. Dittmar and D. G. Hall, *Cruise noise of an advanced propeller with swirl recovery vanes,* Journal of aircraft **30**, 221 (1993).

[23] T. Sinnige, T. C. Stokkermans, D. Ragni, G. Eitelberg, and L. L. Veldhuis, *Aerodynamic and aeroacoustic performance of a propeller propulsion system with swirl-recovery vanes,* Journal of Propulsion and Power **34**, 1376 (2018).

[24] L. E. van den Ende, *Swirl Recovery Vanes for Propeller Propulsion Systems: An Aerodynamic and Aeroacoustic Investigation by Lattice Boltzmann Method*, Master's thesis, Delft University of Technology (2018).

[25] J. Gazzaniga and G. Rose, *Wind tunnel performance results of swirl recovery vanes as tested with an advanced high speed propeller,* in *28th Joint Propulsion Conference and Exhibit* (1992) p. 3770.

[26] O. Yamamoto, *Numerical calculations of propfan/swirl recovery vane flow field,* in *28th Joint Propulsion Conference and Exhibit* (1992) p. 3771.

[27] Y. Wang, Q. Li, G. Eitelberg, L. Veldhuis, and M. Kotsonis, *Design and numerical investigation of swirl recovery vanes for the fokker 29 propeller,* Chinese Journal of Aeronautics **27**, 1128 (2014).

[28] W. J. M. Rankine, *On the mechanical principles of the action of propellers,* Transactions of the Institution of Naval Architects **6** (1865).

[29] L. Prandtl, *Applications of modern hydrodynamics to aeronautics, 116,* NACA Technical Report, Germany (1923).

[30] A. Betz, *Screw propeller with minimum energy loss, (schraubenpropeller mit geringstem energieverlust),* Translation from German by Sinclair, D. A., Translation Section, NRC Library. (1919).

[31] P. G. Saffman, *Vortex dynamics* (Cambridge university press, 1995).

[32] Z. Montgomery, *A propeller model based on a modern numerical lifting-line algorithm with an iterative semi-free wake solver,* Master's thesis, Utah State University (2018).

[33] M. Drela and H. Youngren, *Xrotor download page,* http://web.mit.edu/drela/Public/web/xrotor/ (2011).

[34] W. F. Phillips and D. Snyder, *Modern adaptation of prandtl's classic lifting-line theory,* Journal of Aircraft **37**, 662 (2000).

[35] W. F. Durand, *Airfoils and airfoil systems of finite span,* in *Aerodynamic Theory* (Springer, 1935) pp. 165–280.

[36] M. Drela and H. Youngren, *Xfoil: an interactive program for the design and analysis of subsonic isolated airfoils,* http://web.mit.edu/drela/Public/web/xrotor/ (2015).

[37] R. T. Jones, *Correction of the lifting line theory for the effect of the chord*, Tech. Rep. (NACA, 1941).

[38] J. Wrench, *The calculation of propeller induction factors,* Applied Mathematics Laboratory Tecnical Report, No. 1116 (1957).

[39] T. Stokkermans, N. Van Arnhem, and L. Veldhuis, *Mitigation of propeller kinetic energy losses with boundary layer ingestion and swirl recovery vanes,* in *Proceedings of the 2016 Applied Aerodynamics Research Conference, Royal Aeronautical Soc., London* (2016) pp. 56–69.

[40] B. Montgomerie, *De-camber: Explanation of an effect of lift reduction near the tip caused by the local flow around airplane wings or wind turbine tips,* in *Proc. Plenary meeting of the group for Dynamic Stall and 3D Effects a European Union, Joule*, Vol. 2 (1995) pp. 3–4.

[41] J. N. Sørensen, K. O. Dag, and N. Ramos-García, *A new tip correction based on the decambering approach*, in *Journal of Physics: Conference Series*, Vol. 524 (IOP Publishing, 2014) p. 012097.

[42] A. Silverstein and H. A. Wilson Jr, *Drag and Propulsive Characteristics of Air-Cooled Engine-Nacelle Installations for Large Airplanes*, Tech. Rep. No. NACA-SR-122 (National Aeronautics and Space Admin Langley Research Center Hampton, 1939).

[43] M. D. Patterson, J. M. Derlaga, and N. K. Borer, *High-lift propeller system configuration selection for nasa's sceptor distributed electric propulsion flight demonstrator*, in *16th AIAA Aviation Technology, Integration, and Operations Conference* (2016) p. 3922.

[44] C. Miller, *Euler analysis of a swirl recovery vane design for use with an advanced single-rotation propfan*, in *24th Joint Propulsion Conference* (1988) p. 3152.

[45] F. Çelik and M. Güner, *Energy saving device of stator for marine propellers*, Ocean engineering **34**, 850 (2007).

[46] H. C. Garner, E. Rogers, W. Acum, and E. Maskell, *Subsonic wind tunnel wall corrections*, Tech. Rep. (Advisory Group for Aerospace Research and Development Neuilly-Sur-Seine (France), 1966).

[47] F. Vandrey, *Der duseneinfluss auf die windkanalkorrekturen bei ebener stromung*, Jahrbuch der Deutchen Luftfartforschung , 1786 (1942).

[48] G. Eitelberg, T. Sinnige, T. van Pelt, and E. Raijmakers, *Ae4115: Experimental simulations reader*, (TU Delft, 2020).

[49] B. Simon, *Advanced potential flow simulator*, (2017), [Online; accessed January 19, 2023].

[50] K. Karamcheti, *Principles of Ideal-Fluid Aerodynamics* (John Wiley & Sons, 1966).

[51] N. van Arnhem, *Unconventional Propeller-Airframe Integration for Transport Aircraft Configurations*, Ph.D. thesis, Delft University of Technology (2022).